ABSTRACT

Title of dissertation: DYNAMICS OF NONLINEAR GRAVITY-CAPILLARY WAVES IN DEEP WATER NEAR RESONANCE

Naeem Masnadi, Doctor of Philosophy, 2016

Dissertation directed by: Professor James H. Duncan
Department of Mechanical Engineering

The minimum phase speed of linear gravity-capillary waves in deep water ($c_{\min}$) is known to be the bifurcation point of three-dimensional solitary waves ("lumps"). In the present thesis, various aspects of unsteady gravity-capillary lumps are investigated in the context of three sets of experiments. In the first set, cinematic shadowgraph and refraction-based techniques are utilized to measure the temporal evolution of the free surface deformation pattern downstream of a surface pressure source as it moves along a towing tank, while numerical simulations using a model equation are used to extend the experimental results. The focus of this study is on exploring the characteristics of the observed periodic shedding of lump-like depressions for towing speeds close to $c_{\min}$. From the experiments, it is found that the speed-amplitude characteristics and the shape of the depressions are nearly the same as those of the freely propagating gravity-capillary lumps of inviscid potential theory. The periodic behavior is found to be analogous to the periodic generation of two-dimensional solitary waves in shallow water by a source moving at trans-critical

speeds of pure gravity waves. In the second set of experiments, the effect of viscous dissipation on freely propagating lumps is examined. A steady forced lump is first generated by applying appropriate forcing and towing speed. The forcing is then removed suddenly and the change in shape and speed of the lump is measured as it propagates freely under the action of viscosity. It is found that the localized structure of the lump is maintained during the decay and the first measurement of the decay rate of gravity-capillary lumps is reported. In the third set of experiments, the interactions of state III lumps generated by two pressure sources moving in parallel straight lines are investigated. The sources are adjusted to produce nearly identical periodic responses. The first lump generated by each source, collides with the lump from the other source in the center-plane of the two sources. It was observed that a steep depression is formed during the collision but breaks up soon after and radiates energy away in the form of small-amplitude radial waves. After the collision, a quasi-steady pattern is formed with several rows of localized depressions that are similar to lumps but exhibit periodic oscillations in depth.

Dynamics of Nonlinear Gravity-Capillary Waves in Deep Water Near Resonance

by

Naeem Masnadi

Dissertation submitted to the Faculty of the Graduate School of the
University of Maryland, College Park in partial fulfillment
of the requirements for the degree of
Doctor of Philosophy
2016

Advisory Committee:

Professor James H. Duncan, Chair/Adviser

Professor James Baeder

Professor Kenneth Kiger

Professor Johan Larsson

Professor Amir Riaz

Dedication

To Maman and Baba.

Acknowledgments

This section is dedicated to people who helped and supported me through the ups and downs of my Ph.D. First and foremost, I would like to express the deepest appreciation to my advisor and mentor, Professor James Duncan, for the continuous support of my Ph.D study and related research, for his patience, motivation, and immense knowledge.

I wish to express my sincere gratitude for my colleagues and friends at the Hydrodynamics lab. To Dr. Christine Ikeda, Dr. Nathan Washuta, An Wang, Ren Liu, Dan Wang, Karan Parmar, Martin Erinin and Dr. Xinan Liu, thank you for the great teamwork and for making the sleepless nights before deadlines enjoyable. I certainly learned a lot from each and everyone of you.

I would like to thank my committee members, Professor Kenneth Kiger, Professor Johan Larsson, Professor Amir Riaz and Professor James Baeder for their time and insightful comments. I would also like to acknowledge the other faculty members who have helped me through the years: Professor Bongtae Han, Professor Eitan Tadmor, Professor T. R. Akylas of MIT and Professor Emilian Părău of University of East Anglia.

Special thanks to Farhad Goodarzi, Endri Mustafa, Shahin Sefati, Sadaf Khosravifar, Sahar Akram, Ehsan Aramoon, Mahsa Dornajafi, Pouyan Khakbaz, Hadi Sadrsadat, Darya Razavi and many others whose friendship have been a blessing for me and to Anahita Abazari for her companionship and understanding.

Finally, my most heartfelt appreciation is reserved for my family for their

endless love and support. To my parents, Masoumeh and Hassan, who always encouraged me to ask questions and try to find answers, I love you both. I'm also thankful to my siblings, Nasim, Nasir and Naghmeh for putting up with my long and badly timed Skype calls.

Table of Contents

List of Figures

List of Abbreviations

k	wavenumber
ω	radian frequency
c_p	phase velocity
g	gravitational acceleration
τ	surface tension
ρ	density
H	water depth
$c_{\min}$	minimum phase speed of linear gravity-capillary waves
$k_{\min}$	minimum wavelength of linear gravity-capillary waves
Bo	Bond number
U	source speed
c_g	group velocity
c_0	maximum speed of linear gravity waves ($c_0 = \sqrt{gH}$)
α	nondimensional source speed ($\alpha = U/c_{\min}$)
ϵ	nondimensional forcing parameter
h_0	dimple depth
d	air-jet tube diameter
$\mathbf{v_1}$	vector of incident light ray
$\mathbf{v_2}$	vector of refracted light ray
v_x	displacement in x direction
v_y	displacement in y direction
h_d	distance between the free surface and the dot pattern
θ_1	angle between incident ray and surface normal
θ_2	angle between refracted ray and surface normal
δ	difference between θ_1 and θ_2
n_1	refractive index in first medium
n_2	refractive index in second medium
$\hat{n}$	surface normal vector
η	free surface elevation
ξ	$\xi = x + \alpha t$
$\tilde{\nu}$	viscous damping parameter
β	nonlinear coefficient
$\mathscr{H}$	Hilbert transform
p	pressure distribution
Δt	time step
σ	exponential decay rate
h	maximum depth of a lump
T	period
T^*	reference time
$T_{\min}$	period at the minimum phase speed of linear gravity-capillary waves
$\overline{T}$	average period
Fr	Froude number
α'	differential speed parameter
D	distance between air-jet tubes

Chapter 1: Introduction

1.1 Gravity-capillary waves dispersion

Small amplitude water waves in the presence of surface tension allow solutions in the form of $a\cos(\mathbf{k}\cdot\mathbf{x}-\omega t)$ and are governed by the dispersion relation

$$c_p^2 = (\frac{g}{k}+\frac{\tau}{\rho}k)\tanh(kH) \tag{1.1}$$

where c_p is the wave phase speed, $k = 2\pi/\lambda = |\mathbf{k}|$ is the magnitude of the wave number vector, λ is the wavelength, g is the gravitational acceleration, ρ is the density of water, τ is the surface tension and H is the undisturbed water depth. It is a well known fact that this dispersion relation predicts a minimum phase speed of $c_{\min} = (4\tau g/\rho)^{1/4}$ at a finite wave number $k_{\min} = (\rho g/\tau)^{1/2}$ when the Bond number ($Bo = \tau/(\rho g H^2)$) is less than a third (see figure 1.1). In clean water ($\tau = 73.0$ mN/m), the minimum phase speed has a value of $c_{\min} = 23.13$ cm/s and happens at a wavelength of about $\lambda_{\min} = 1.71$ cm (see for example Whitham, 2011).

It is also well known that the linear steady state wave pattern generated by an infinitesimal point source moving at a constant speed, U, consists exclusively of wave components with phase speed $c_p \leq U$. Thus, for $U < c_{\min}$, the source does not create a steady linear wave pattern. In fact, the linearized theory fails as U

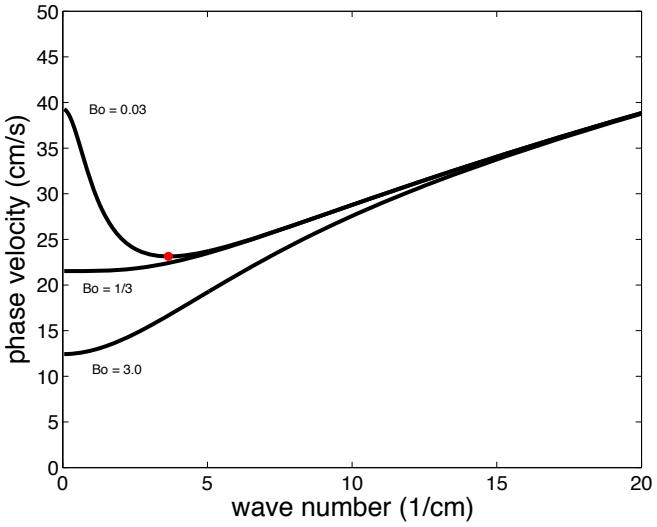

Figure 1.1: Phase speed versus wave number for different values of Bond number

approaches $c_{\min}$ and the solution becomes unbounded. Another important feature of this minimum phase speed is that the phase velocity and group velocity are equal. In fact, phase velocity and group velocity are equal at any extrema of $c_p(k)$ as can be seen by taking the derivative of phase speed with respect to k,

$$\frac{\mathrm{d}c_p}{\mathrm{d}k} = \frac{\mathrm{d}(\omega/k)}{\mathrm{d}k} = \frac{1}{k}\frac{\mathrm{d}\omega}{\mathrm{d}k} - \frac{\omega}{k^2} = \frac{c_g}{k} - \frac{c_p}{k}$$

These extrema are known to be the bifurcation points for nonlinear solitary waves (Kim & Akylas, 2005).

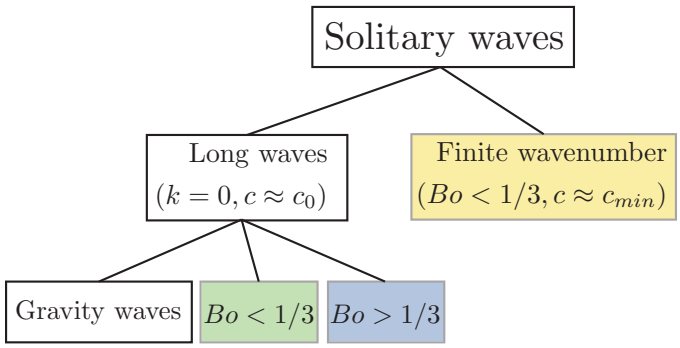

Figure 1.2: Different types of solitary water waves due to the effects of surface tension and water depth.

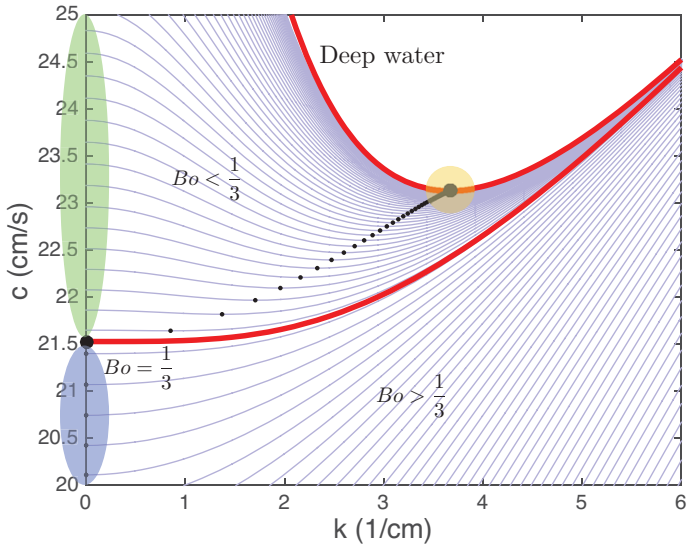

Figure 1.3: Dispersion curves for gravity-capillary waves. For $Bo > 1/3$, the phase speed has a global minimum at $k = 0$. For $Bo < 1/3$, $c_p(0) = \sqrt{gH}$ is a local maximum and there exist a local minimum at a finite wave number.

1.2 Solitary waves in water

1.2.1 Two-dimensional solitary waves

Solitary waves are localized disturbances that propagate with permanent form as a result of a perfect balance between the opposing effects of nonlinearity and dispersion. Several types of solitary water waves are known to exist due to the effects of surface tension and finite depth. These waves bifurcate from the extrema of the linear dispersion curve, $c_p(k)$. The most familiar of these waves are the two-dimensional gravity solitary waves in the long-wave-length limit ($kH \to 0$), which corresponds to a global maximum ($c_p(0) = \sqrt{gH}$) of the linear pure gravity wave dispersion curve. These solitary waves are governed by the celebrated Korteweg-de Vries equation (KdV) in the small amplitude limit. This theory was developed to explain the first scientific observations of solitary waves by John Scott Russell in 1834 (Korteweg & de Vries, 1895; Russell, 1844). A recreation of Russell's discovery is shown in figure 1.4. The accuracy of KdV equation for one-dimensional moderate amplitude waves was tested experimentally by Hammack & Segur (1974). For a complete review and historical notes, see Miles (1980).

When surface tension effects are included, there are either one or two extrema of the dispersions curve, depending on the value of the Bond number. In the long wave limit, the phase speed $c_0 = \sqrt{gH}$ is a local maximum (global minimum) of the linear dispersion relation when Bond number is less (greater) than 1/3 and KdV-type solitary waves of elevation (depression) exist. Experimental observations of the

Figure 1.4: A Soliton on the Scott Russell Aqueduct on the Union Canal near Heriot-Watt University, 12 July 1995 (From http://www.ma.hw.ac.uk/solitons/press.html).

KdV type solitary gravity-capillary waves of both depression and elevation on a thin layer of mercury were reported in Falcon *et al.* (2002).

As discussed above, the dispersion curve also features a minimum at a finite wavenumber in water of finite or infinite depth when $Bo < 1/3$. Another class of two-dimensional solitary waves that bifurcate at this minimum phase speed was discovered more recently. The existence of gravity-capillary solitary waves in deep water was first proposed by Longuet-Higgins (1988) on physical grounds by considering the effects of gravity on exact solutions for finite amplitude pure capillary waves discovered by Crapper (1957). Longuet-Higgins (1989) later made numerical calculations of the profiles of two-dimensional solitary waves and reported a limiting case for the steepest wave where an "air-bubble" gets trapped in the solitary wave. Profiles of solitary waves computed via the method explained in Longuet-Higgins

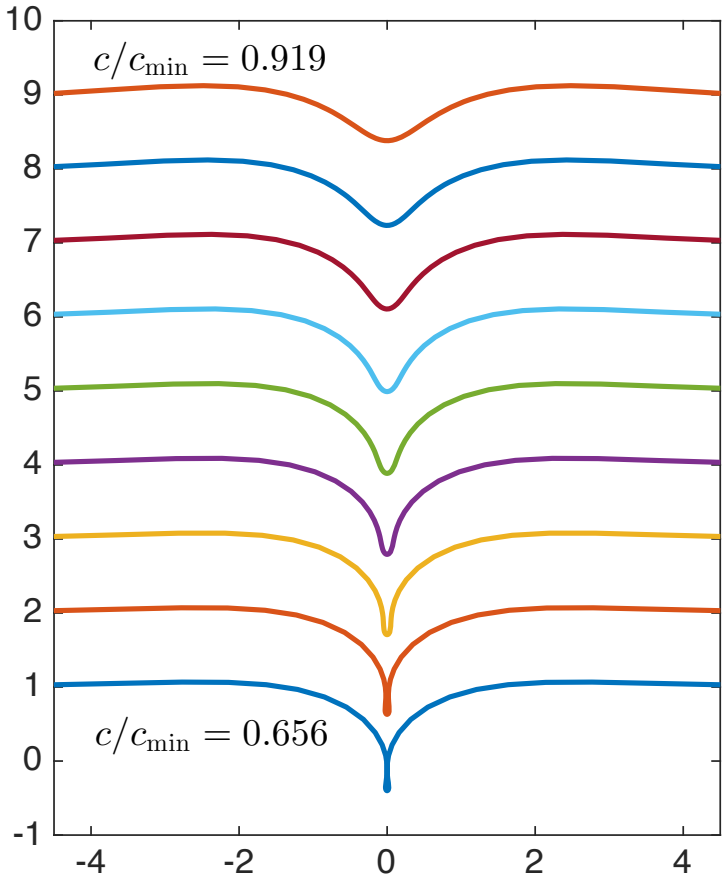

Figure 1.5: Profiles of solitary waves computed via the method explained in Longuet-Higgins (1989) for different speeds. The bottom profile shows the limiting case where an "air bubble" is entrapped in the solitary wave.

(1989) are plotted for different speeds in figure 1.5. Note that for these solitary waves, the phase speed is smaller than $c_{\min}$ and the speed decreases with increasing depth. Vanden-Broeck & Dias (1992) extended the calculations of Longuet-Higgins (1989) using a boundary integral method and found two branches of solitary waves bifurcating at $c_{\min}$; one of depression type and one of elevation type. In the small-amplitude limit, these solitary waves are governed by the nonlinear Schrödinger equation and behave as modulated wave-packets with the wave envelope moving with the wave crests at a speed slightly below $c_{\min}$ (Akylas, 1993). Longuet-Higgins (1993) also made use of the NLS equation and concluded that "in any dispersive medium which supports envelope solitons we may expect the existence of a family of steady solitary waves near a maximum or minimum of the phase speed, that is to say whenever the group velocity nearly equals the phase velocity". Zhang (1995) developed an optical technique to measure the water surface gradient and performed experiments in a wind wave tank and measured the shape of the surface features. He observed isolated steep surface depressions resembling the solitary waves profiles calculated by Longuet-Higgins (1989) and reported good agreement between theory and his experiments. In a later study, Longuet-Higgins & Zhang (1997) carried out experiments in a water flume and generated two-dimensional solitary waves by blowing air vertically onto the water surface through a two-dimensional slit and resonantly exciting the water surface near the minimum phase speed. The free-surface shape showed good agreement with the numerical results of Longuet-Higgins (1989). They also measured the variation of the amplitude versus phase speed as they turned off the air flow and let the solitary wave get damped by viscosity. Longuet-Higgins

(1997) developed a theory for the viscous dissipation of steep gravity-capillary solitary waves with the assumption that the solitary wave maintains its steady form while decaying. Hence, the rate of work due to surface stresses is equal to the rate of dissipation of energy in the bulk of the fluid. For a review of two-dimensional gravity-capillary solitary waves see Dias & Kharif (1999).

1.2.2 Three-dimensional solitary waves

Fully localized, three-dimensional solitary waves (usually referred to as "lumps") can also bifurcate at the extrema of the linear phase speed. A necessary condition for a lump to remain localized in all spatial directions is that no other linear wave can co-propagate with the speed of the lump (Milewski, 2005). This condition can only be achieved at a minimum of the linear phase speed, which can occur at zero or a finite wavenumber depending on the Bond number. For pure gravity waves the phase speed only has a maximum at $k = 0$ and the existence of three-dimensional solitary waves of elevation has been ruled out by Craig (2002).

As mentioned above, when $Bo > 1/3$, the phase speed has a global minimum at zero wavenumber (see figure 1.3). Small amplitude three-dimensional solitary waves in this condition are governed by the Kadomtsev-Petviashvili I (KP-I) equation (Kadomtsev & Petviashvili, 1970), which is a natural extension of the KdV equation to three dimensions and admits depression lump solutions. However, the condition for the Bond number restricts the water depth to at most a few millimeters and the viscous effects at the bottom boundary, which are not included in the above

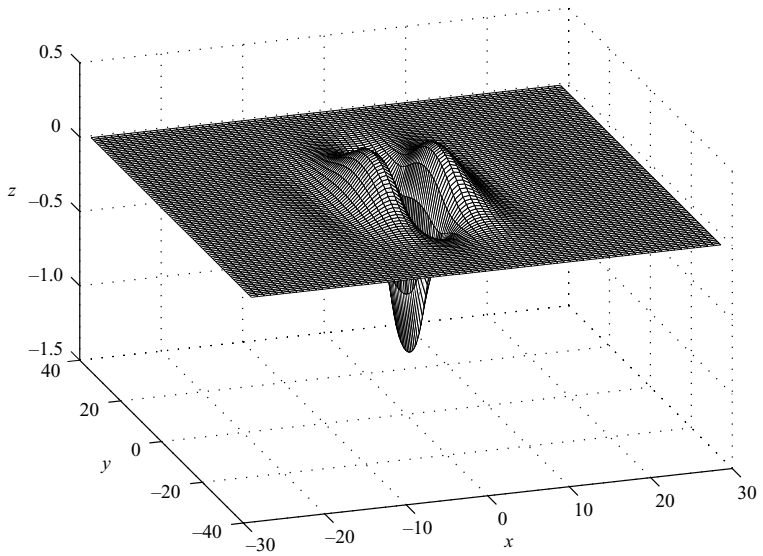

Figure 1.6: A freely propagating three-dimensional lump moving at $\alpha = c/c_{\min} = 0.92$ from fully-nonlinear potential flow calculations by Părău *et al.* (2005)

theories, become important.

When $Bo < 1/3$, three-dimensional solitary waves of elevation and depression bifurcate at the above-mentioned $c_{\min}$ that occurs at finite wavenumber. Kim & Akylas (2005) found that similar to two-dimensional gravity-capillary solitary waves, in the small-amplitude limit, three-dimensional solitary waves behave as modulated wavepackets with envelope and crest moving at the same speed and are governed by an elliptic-elliptic Davey-Stewartson equation Davey & Stewartson (1974) in water of finite depth and an elliptic two-dimensional NLS equation in deep water. Milewski (2005) used a continuation method and found a branch of solutions connecting the long solitary waves in the surface-tension-dominated regime to wave-packet solitary waves as $Bo = 1/3$ is crossed. He pointed out that the wavepacket lumps are more

relevant since the viscous effects at the bottom boundary become negligible. Finally, Părău *et al.* (2005) extended the boundary integral method used by Forbes (1989) to include surface tension and solved the fully nonlinear potential flow equations to find steady lump profiles. These lumps are fully-localized in all directions and are more extended in the transverse direction (figure 1.6).

The dynamics of these lumps, including their stability and interactions, have been explored using model equations (Akers & Milewski, 2010; Akylas & Cho, 2008; Wang & Milewski, 2012). Wang & Milewski (2012) developed a new model equation called the cubic model and validated its accuracy in 2-D with potential flow calculations. They then used this model in 3-D to study the stability and evolution of lumps. They found out that all lumps are unstable except for the moderate-amplitude depression type and the unstable waves evolve into a time periodic localized state called a "breather".

1.3 Response of a water surface to a moving disturbance near resonance

Moving a localized free-surface pressure source or bottom topographic feature at speeds near one of the critical speeds, c_0 or $c_{\min}$, is a common method of generating solitary waves. These extrema speeds are associated with a resonant condition: The linear solution to a disturbance moving at these speeds becomes unbounded and naturally, the nonlinear effects become important. In two dimensions, the nonlinear response of a water surface to a steady pressure distribution moving at speeds close to

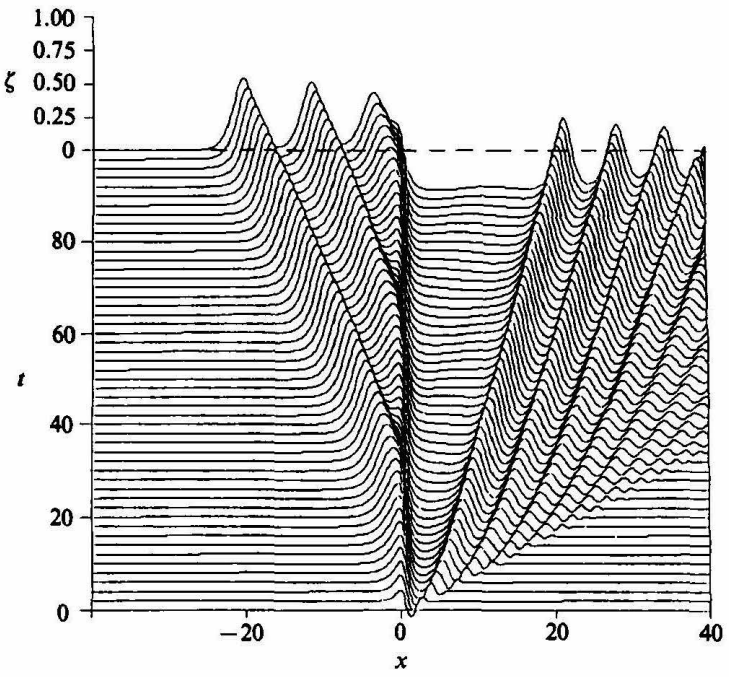

Figure 1.7: Periodic generation of solitary waves upstream of a pressure source moving at the critical speed (from Wu, 1987).

c_0 features periodic shedding of solitary waves upstream of the disturbance (Akylas, 1984). The energy input to the system due to the pressure source moving at trans-critical speeds cannot be radiated away since the dispersive effect is relatively weak. The surface response will grow and, since for 2-D gravity waves the higher amplitude waves move faster, the local wave moves ahead of the source and a solitary wave is generated. This process is then repeated periodically (Wu, 1987) as shown in figure 1.7.

In the regime of strong surface tension ($Bo > 1/3$), this problem was considered in three dimensions by Berger & Milewski (2000) using a forced generalized Benny-Luke equation (Benney & Luke, 1964) that includes the effects of surface ten-

sion and a topographical forcing (Milewski, 1998). Periodic shedding of 3-D lumps was observed downstream of the topography. These lumps move at an angle with respect to the direction of the flow and their amplitude and period of generation depends on the flow speed. The Benny-Luke equation is inviscid and since viscous effects become important in shallow water flows with $Bo > 1/3$, the results may not be physically realizable.

In deep water, the surface response to a pressure distribution moving at speeds close to $c_{\min}$ was investigated experimentally by Diorio *et al.* (2009). In this study, the wave pattern behind a small pressure distribution created by a vertical air jet that was set to move horizontally at constant speed below the minimum phase speed was observed by a variety of photographic measurement techniques. They identified three response states for the wave pattern as the towing speed of the pressure source approached $c_{\min}$ (figure 1.8). At low speeds, the response is similar to that found when the air jet is stationary (state I) and is essentially a circular depression under the pressure source. As the speed is increased, an abrupt transition occurs and a wave-like state in the form of a solitary depression is formed behind the pressure source (state II). The amplitude of the water surface depression is increased significantly compared to that in state I. The wave pattern is steady and is elongated in the cross-stream direction. This pattern resembles the freely propagating lumps calculated by Părău *et al.* (2005) (see figure 1.6). At even higher translation speeds but still less than $c_{\min}$, a third response state (state III) appears and the wave pattern becomes unsteady and features a V-shaped pattern with periodic shedding of lump-like disturbances from the tips of the V. As the speed is increased above $c_{\min}$,

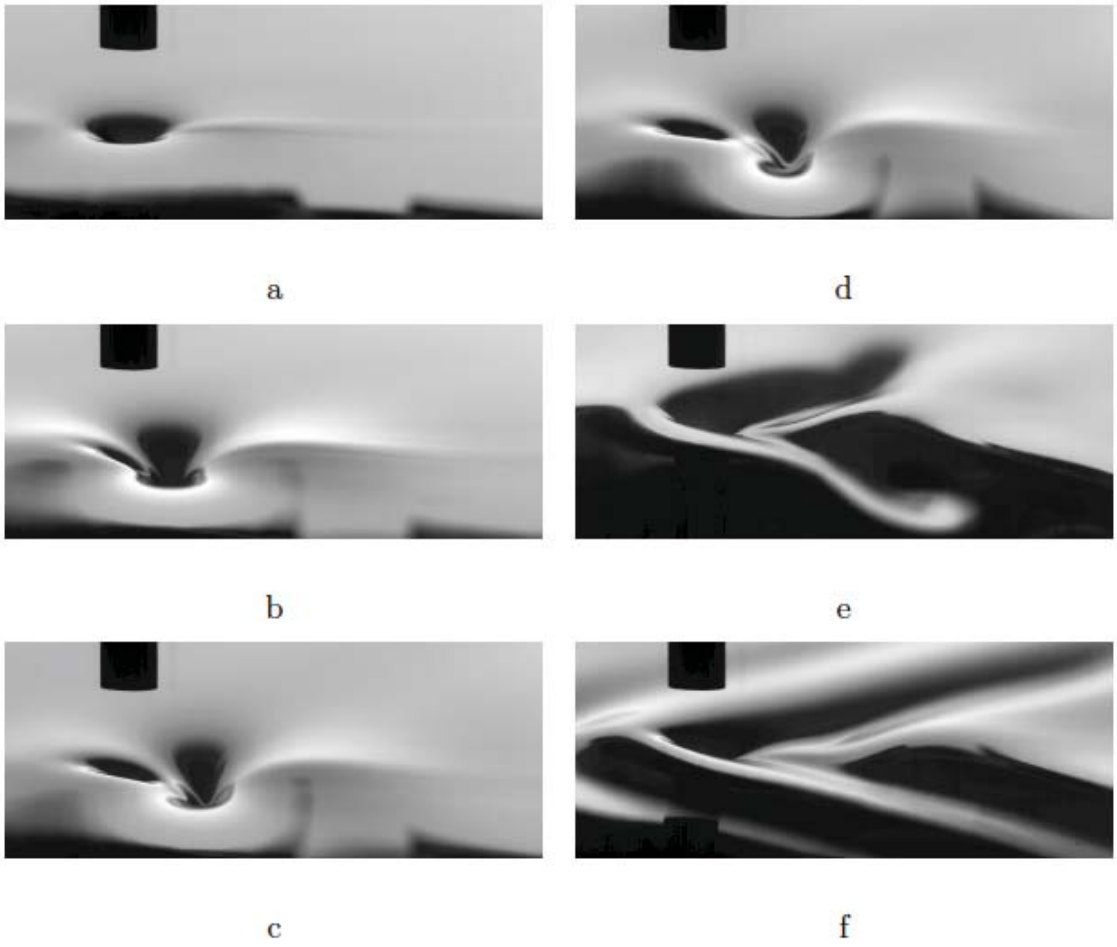

Figure 1.8: Wave pattern behind a pressure source moving at constant speed below $c_{\min}$ from Diorio *et al.* (2009). Images are taken by a high-speed camera positioned to the side of the air-jet tube and above the water surface. The tube is moving from right to left. (a) $\alpha = U/c_{\min} = 0.905$, state I: a small depression under the tube, (b) $\alpha = 0.927$, (c) $\alpha = 0.948$, (d) $\alpha = 0.970$. State II: wave pattern moves behind the pressure source and is elongated in cross-stream direction, (e) $\alpha = 0.981$. State III: unsteady V-shape pattern with lump-like disturbances shedding from the tips of the V, (f) $\alpha = 1.03$, linear pattern

the pattern becomes similar to the steady, V-shaped, linear pattern with surface-tension-dominated waves ahead of the source and gravity dominated waves behind it. Characteristics of state II response and the unsteady behavior in the transition region between state I and state II was explored in detail by Diorio *et al.* (2011) but careful examination of the unsteady response of state III and the effects of viscous dissipation on gravity-capillary lumps were left for future studies.

1.4 Thesis outline

The main objective of this thesis is to explore the dynamics of gravity-capillary waves in deep water near the resonant condition and use experimental and numerical tools to expand our understanding of these waves. Three main topics are addressed in the subsequent chapters. In chapter 2, the periodic generation of lump-like disturbances downstream of a source moving at speeds close to $c_{\min}$ is examined. A refraction-based measurement technique is used to obtain full-field surface elevation data. Experimental results suggest that the disturbances in state III are in fact lumps. Different characteristics of these lumps are documented from experimental data and numerical simulations of a model equation. A new asymmetric response is found in the transition region between state II and state III. The evolution of a free lump under the effects of viscous damping is explored in chapter 3. A steady lump in state II that is generated under forced condition is let free by removing the forcing and the decay properties of the free lump is measured. In chapter 4, the interaction of state III lumps generated by two pressure sources moving in parallel is

investigated and the first account of an oblique collision of gravity-capillary lumps is reported. Chapter 5 provides a summary of contributions and suggestions for future research.

Chapter 2: The generation of gravity-capillary solitary waves by a pressure source moving at a trans-critical speed[1]

2.1 Introduction

As discussed in §1.3, Diorio *et al.* (2011) found three distinct response states for a pressure distribution moving at speeds below $c_{\min}$. They reported detailed measurements of the state II response and found a one-to-one relation between the amplitude and the phase speed of the waves (a known feature of solitary waves) and compared it to the bifurcation curves from theory. The techniques employed by Diorio *et al.* (2011) were suited only to steady wave patterns and therefore, they were not able to make measurements of the state III response or to accurately determine the transition between state II and state III. Images from Diorio *et al.* (2009) for a cycle of shedding in state III are shown in figure 2.1. Cho *et al.* (2011) used a model equation with quadratic nonlinearity and a viscous dissipation term to capture the steady and unsteady behavior of the wave pattern generated by a pressure source moving at a speed near $c_{\min}$. Their results compared favorably with the experimental results of Diorio *et al.* (2011). It was found that viscous damping

[1]Some of the results presented in this chapter can be found in Masnadi & Duncan (2016).

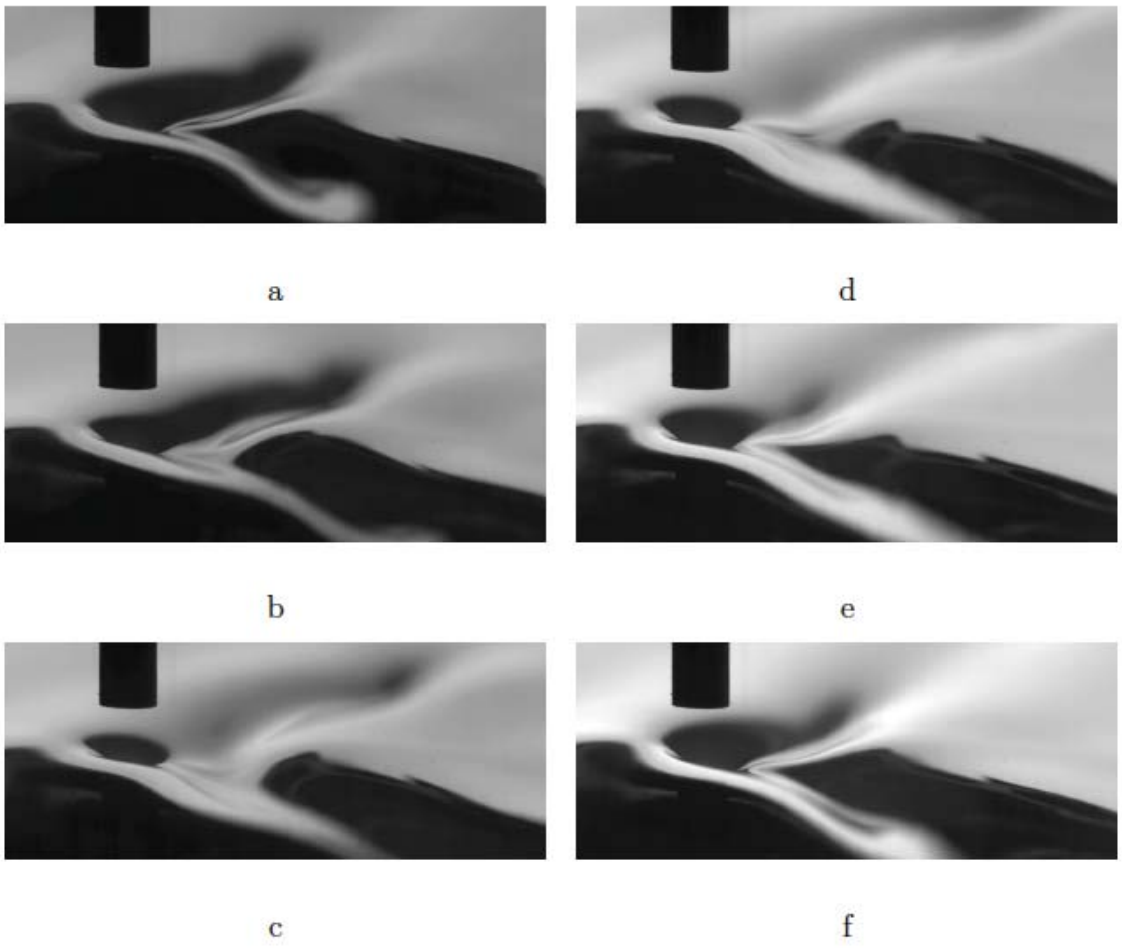

Figure 2.1: Snapshots of State III for one cycle of "lump shedding" for $\alpha = 0.981$ from Diorio *et al.* (2009). The images are separated by 0.36 s in time.

plays an important role in the formation of both the steady response pattern in state II and the unsteady pattern in state III.

In this chapter, detailed measurements of the unsteady wave pattern behind a pressure source moving with speeds close to $c_{\min}$ and with a range of pressure magnitudes are presented. The water depth is chosen so that the Bond number is much smaller than 1/3 and the problem is considered to be in deep water. These measurements are used for two purposes: (i) to explore the state III response includ-

ing the periodic shedding and propagation of unsteady localized depressions and (ii) to investigate the effect of viscous damping on these depressions.

The chapter is structured as follows: The experimental details and the measurement techniques are described in §2.2 and §2.3, respectively. This is followed in §2.4 by a brief overview of the model equation described in Cho *et al.* (2011) and the numerical procedure used to solve it. The experimental and numerical results are then presented and discussed in §2.5. Finally, the conclusions of this study are given in §2.6.

2.2 Experimental set-up

The experiments were performed in an open-surface towing tank that is 6 m long, 30 cm wide[2] and 7 cm deep (see figure 2.2). The side walls and bottom of the tank are made of 0.64-cm-thick clear polycarbonate sheets which are supported by an external aluminium frame. The aluminium frame is attached to the steel frame of a large wind-wave tank (14.8 m long, 1.2 m wide and 2.4 m high) such that the towing tank is at an elevation of about 2 m above the laboratory floor. An instrument carriage travels along the length of the wind-wave tank and so along the length of the towing tank. The carriage is supported by four hydrostatic oil bearings that ride on a pair of precision rails positioned on the top of each sidewall of the wind-wave tank. This bearing system provides a very low vibration level. The carriage rails where leveled by comparing the carriage height with the calm water

[2]That the tank is sufficiently wide to eliminate the effects of the tank sidewall on the results is addressed in §2.5.

surface in the towing tank and after adjustment the carriage height varied by at most 0.4 mm along the length of the tank. The carriage is driven by steel cables that are in turn driven by a servo motor. The carriage motion is controlled by a computer-based feedback system that employs a carriage position sensor that runs the length of the tank. In all the experiments presented in this chapter, the carriage is set to accelerate to a constant speed within the first 25.4 cm of the translation and decelerate to zero speed in the last 25.4 cm of its motion. This restriction creates an average acceleration and deceleration of about 10 cm/s^2 for the range of towing speeds used. Evaluation of the carriage position sensor data show that the carriage position at any instant in time is repeatable within ± 0.5 mm from run to run and the average speed of the carriage during its constant speed motion has a relative error of less than 0.01 percent. In the following, the carriage speed U is indicated by the dimensionless parameter, $\alpha = U/c_{\min}$.

A pressure disturbance is made on the water surface by blowing air through a 2.5-mm-ID tube that is attached to the instrument carriage. The tube is oriented vertically with the bottom end of the tube positioned at about 1 cm above the water surface. The tube is embedded in silicon and sandwiched between two aluminum plates to increase its stiffness. The pressure source for the jet is a 37-l compressed air tank that is mounted on the carriage and is connected to the air-jet tube via a system consisting of a pressure regulator, a needle valve, a flow meter and flexible hoses. The compressed air tank is pressurized to about 2.7 bar before each experimental run. When the carriage is stationary, the air flow makes a small axisymmetric depression on the water surface directly under the tip of the air-jet tube.

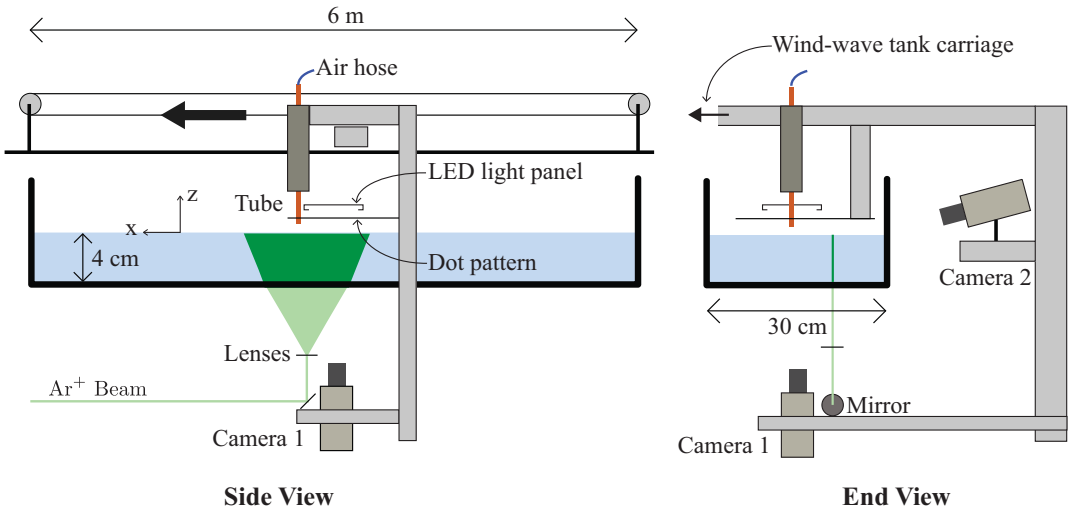

Figure 2.2: Schematic of the experimental set-up. The tank has clear walls and is positioned about 2.0 m above the laboratory floor. The water surface is excited by a vertically oriented jet of air exiting from a small-diameter tube that is mounted on the moving carriage. Two high-speed cameras that are also mounted on the carriage are used to measure the wave pattern around the air jet impingement point. Camera 1 views, through the tank bottom and the wavy water free surface, a dot pattern held just above the water surface. Camera 2 views, from the side of the tank, the intersection of a vertically oriented laser light sheet and the water surface.

Since surface tension effects are of utmost importance in this experiment, the following water preparation and surface tension measurement procedures were followed to minimize and monitor surfactant levels. First, at the beginning of the day of each series of experiments, a separate water treatment tank with an approximate volume of 1 m^3 was filled with filtered tap water. Then, chlorine was added to the water to reach a concentration of about 10 ppm. The water was then circulated through a diatomaceous earth filter for about eight hours before the start of the experiments on that day. The water was then dechlorinated by adding an appropriate amount of hydrogen peroxide. This latter step is necessary because high chlorine levels degrade the fluorescein dye used in the Laser-Induced Fluorescence (LIF) surface profile measurements described below. The dye is then added to the water at a concentration of about 0.7 ppm. This cleaned dye solution was then used to fill the towing tank to a depth of approximately $H = 4$ cm (corresponding to a Bond number of $Bo = 4.65 \times 10^{-3}$). The towing tank includes a water surface skimming system and for ten minutes before each experimental run, water was pumped from the treatment tank through the towing tank and to the drain via the skimmer.

Periodically during the experiments on each day, samples of the towing tank water were extracted and surface tension isotherms of the samples were measured using a KSV NIMA Langmuir trough. In these measurements, the surface tension in the trough is measured with a Wilhelmy plate as the local water surface is compressed by moving Teflon barriers toward the measurement site at a constant rate. These barriers barely touch the water surface. The resulting surface compression increases the number of surfactant molecules per unit water surface area while des-

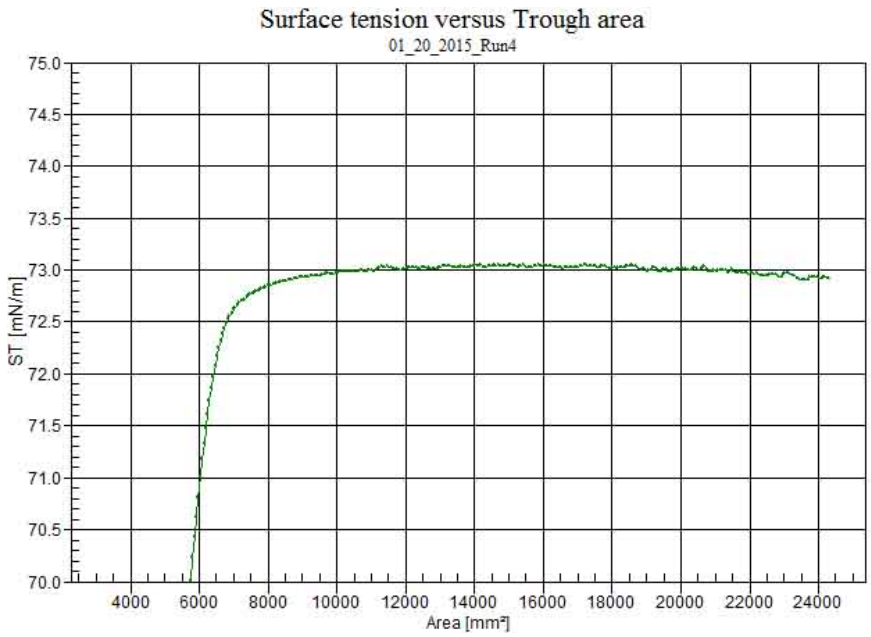

Figure 2.3: An example of surface tension measurements using the Langmuir trough.

orption of the surfactant to the bulk fluid decreases the surface concentration at a slower rate. An example of surface tension measurements using the Langmuir trough is shown in figure 2.3. It was found that the surface tension before compression was maintained at 73.0 ± 0.5 dynes/cm (the value for clean water) throughout the experiments and in all cases the surface tension after compression of the water surface area by 75 percent over a 60-second period resulted in a drop in surface tension of less than 0.5 dynes/cm. As the barriers continued to move creating even higher compressions, the surface tension eventually experienced a sudden drop at compressions ranging from 80 to 95 percent. The water temperature was also measured and maintained at 25 ± 1 C.

2.3 Measurement details

Measurements of the free-surface deformation patterns were carried out using several photography-based techniques. The objective of the first measurement is to obtain the relationship between the airflow rate in the brass tube and the depth of the depression made on the water surface while the carriage was stationary. For these measurements, a still image camera (Nikon D800E, 36 mega-pixel sensor) was placed on a tripod and was oriented horizontally so that it viewed the air-jet tube and water surface from the side. An LED light panel (made by Phlox) was used for illumination and was placed on the opposite side of the tank from the camera. The camera was positioned vertically so that the depression under the air-jet tube was viewed from just below the mean water surface. With this configuration, the surface depression appears dark in the images and the image resolution in the focal plane of the depression was 5.9 μm/pixel. We will refer to this technique as the shadowgraph method.

Following the notation of Diorio *et al.* (2011) we define the forcing parameter $\epsilon = h_0/d$ where h_0 is the depression depth when the air-jet tube is stationary and d is the internal diameter of the tube. A series of shadowgraph images for different airflow rates in the tube are shown in figure 2.4. Since the depression is viewed from under the water surface, the top part of the image is just a reflection. The last image in this figure is a checkerboard pattern with diagonal lines that is placed in the focal plane of the camera and is used to find the location of the free surface when the air-jet is off. The intersection of the diagonal lines in the reflected part

of the image with the diagonal lines in the bottom part is defined as the location of the free surface. With the above-described measurements, ϵ was measured to an accuracy of about ± 0.01. A calibration was performed to relate the air-jet flow rate to ϵ for a range of airflow rates corresponding to $0.15 \leq \epsilon \leq 1$. Also, since the air jet flow rate must remain constant during any experimental run, h_0 was measured over a period of 400 seconds after opening the air valve. This time interval is much longer than the duration of individual runs. It was found that h_0 varied by less than five percent. As mentioned earlier, the carriage tracks are not perfectly level; however, the vertical distance between the tube and the water surface varies by less than four percent.

The shadowgraph method was also used in qualitative observations of the surface response for a wide range of experimental parameters. In these observations, the still image camera used in the h_0 measurements was replaced by a high-speed digital movie camera (Vision Research, Phantom V641, 2560×1600 pixel images), which was mounted to the carriage so that it moved along the tank with the air-jet tube. The LED panel was placed at a fixed position about 3 m from the starting point of the carriage motion and on the opposite side of the tank from the camera to provide backlighting. The camera was triggered to capture images as it passed by the LED panel and those images were used to determine the response state (see §2.5.1).

Quantitative measurements of the unsteady wave pattern behind the air-jet were made via an optical refraction-based technique (called the refraction method in the following) that is similar to the method described in Moisy *et al.* (2009) (see

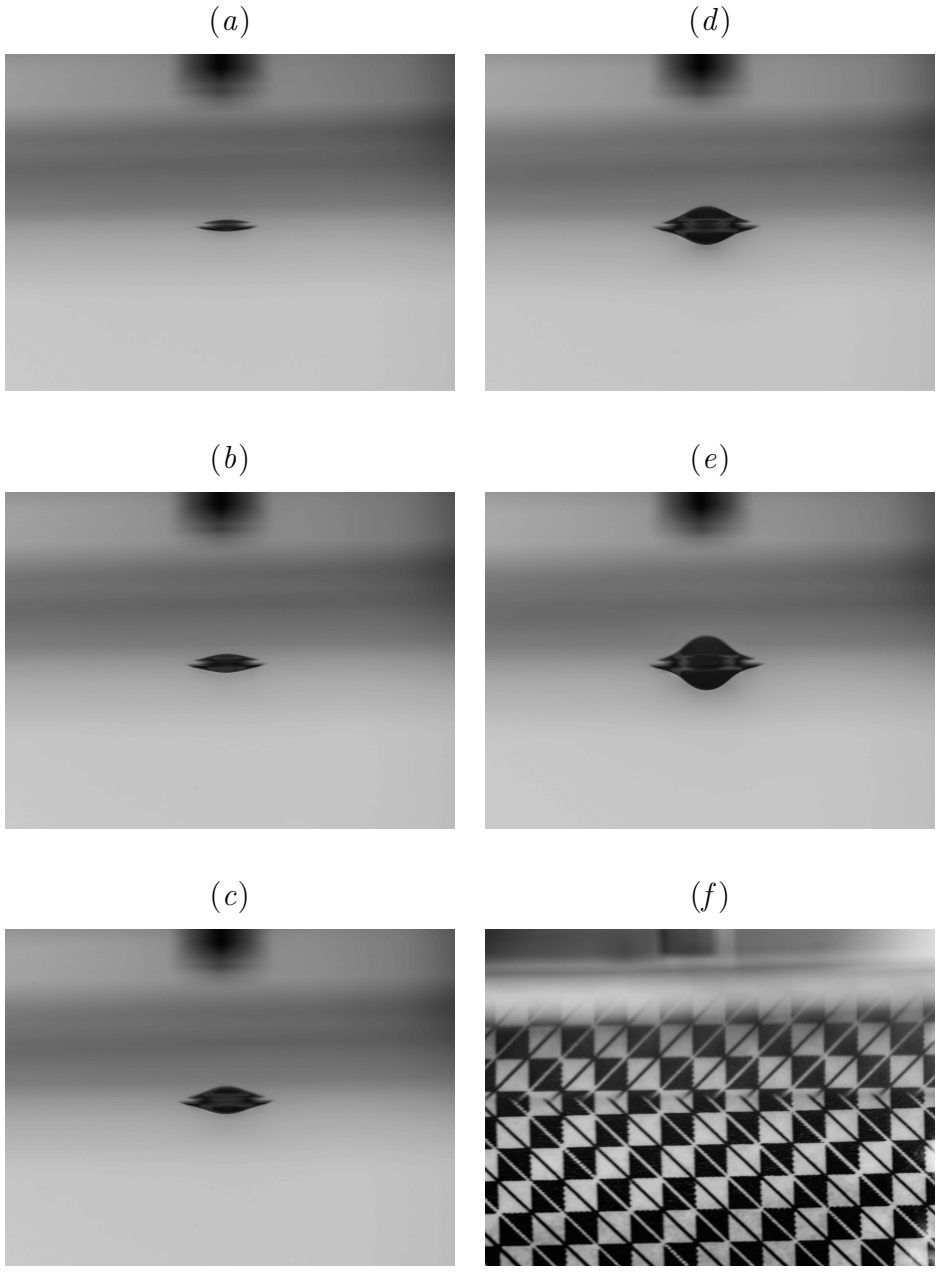

Figure 2.4: (a)-(e) Shadowgraph images of the depression under the air-jet tube when the carriage is stationary for different airflow rates in the tube. The tube is out of focus in the images since the light path length is different for water and air. (f) Image of a checkerboard with diagonal lines that is used to find the location of the free surface.

also Fouras *et al.*, 2006, 2008). In the implementation of this method, a computer-generated image of a pattern of randomly placed black dots is printed on a translucent matte paper (Grafix Matte 0.005 Dura-Lar Film). This pattern is attached to the bottom of a clear plastic plate which is attached to a traverser and held level at an adjustable height above the calm water free surface. The dot pattern is lit from above by the above-described LED panel and is photographed from under the tank with a vertically oriented high-speed digital movie camera (Phantom V641, Vision Research). The camera is mounted 1 m below the tank (camera 1 in figure 2.2) and a long focal length lens (200 mm) is used to image a small surface area. As shown in the figure, the dot pattern, the LED panel and the camera are mounted on the instrument carriage and so move along the tank with the air-jet tube. The dot pattern was imaged at a resolution of about 26 pixels per millimeter. An optical filter is placed in front of the camera lens to block most of the light from the LIF method described below. The camera is triggered by a photo diode that is placed on one side of the tank. A low-power laser beam is pointed at the diode from the other side of the tank. When the carriage passes this location, a knife edge mounted on the carriage blocks the laser beam and the diode sends a signal to trigger the camera. This method was found to be repeatable to within two frames in the camera image sequences. For a carriage speed of 23 cm/s and the camera frame rate of 300 fps used in the experiments, the carriage travels 0.77 mm between frames.

In the first step of the refraction method measurement procedure, a reference movie is taken when the air jet is off and the water surface is calm. A second movie is then taken through the wavy water surface in a separate run with the air jet on.

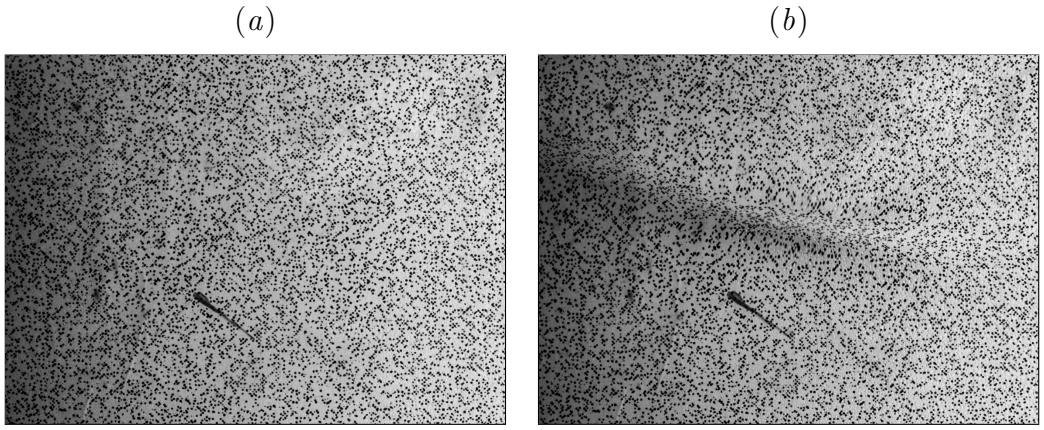

Figure 2.5: Sample cropped images of the dot pattern. These images are approximately 5 cm wide in the physical plane. The actual field of view is about 10 cm $\times$ 6 cm. The dot pattern is placed very close to the water surface (about 5 mm) to make the distortions small. (a) Reference image through calm water surface (b) Distorted image through disturbed water surface.

The measurement technique is based on comparing images that were taken at the same location in the tank in separate runs. Because the camera is triggered by the fixed laser trip device as described above, a given location in the tank corresponds to a specific frame number in all movies. If the tank bottom was completely level, flat and uniform and the carriage remained at exactly the same height above the water surface during the entire run, the images in the reference movie would all be identical and a single reference image taken anywhere in the tank would be sufficient. The frame-by-frame comparisons between the reference and measurement movies is used to reduce errors caused by whatever slight imperfections may be present.

A pair of refraction images, one with the air jet off and one with the jet on, are shown in figures 2.5(a) and (b), respectively. Comparing these two images, the dots appear to move because of the refraction at the wavy interface in image (b). This apparent motion is quantified by using standard PIV software (DaVis by LaVision) to find the dot displacement vectors. The number and size of the dots in the pattern are designed to follow the recommendations for PIV experiments (see for example Adrian & Westerweel, 2010). Figure 2.6 shows the displacement vectors for the image pair shown in figure 2.5. The magnitude of the displacement vectors depends on the local free surface slope and the local distance between the free surface and the dot pattern. A larger distance gives a higher resolution (displacement) for the measurement technique but can result in ray crossing and spurious vectors.

Once the displacement vectors are calculated, approximate surface normal vectors are computed on a uniform grid using Snell's law and assuming that the local distance between the free surface and the dot pattern is the distance between

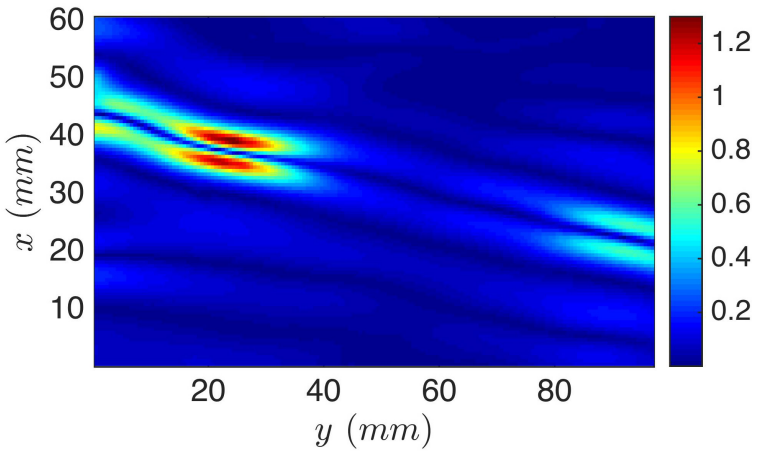

Figure 2.6: Magnitude of displacement vectors (in mm) for the image pair in figure 2.5.

the flat water surface and the dot pattern. As demonstrated in figure 2.7 (for convenience this is drawn in 2-D but can be easily extended to 3-D) at each location on the surface the incident vertical light rays vectors are defined as:

$$\mathbf{v_1} = (0, 0, 1) \tag{2.1}$$

To define the refracted light rays, the distance between the water surface height and the dot pattern is needed. As a first guess this distance can be approximated as the distance between the dot pattern and the calm free surface. This can be corrected to some extent in the subsequent iterations. Therefore, we have

$$\mathbf{v_2} = \frac{(v_x, v_y, h_d)}{\sqrt{{v_x}^2 + {v_y}^2 + {h_d}^2}} \tag{2.2}$$

where v_x and v_y are the displacements in x and y directions and h_d is the distance between the free surface and the dot pattern. According to Snell's law, the incident and refracted rays and the surface normal lie in one plane. This plane is shown on

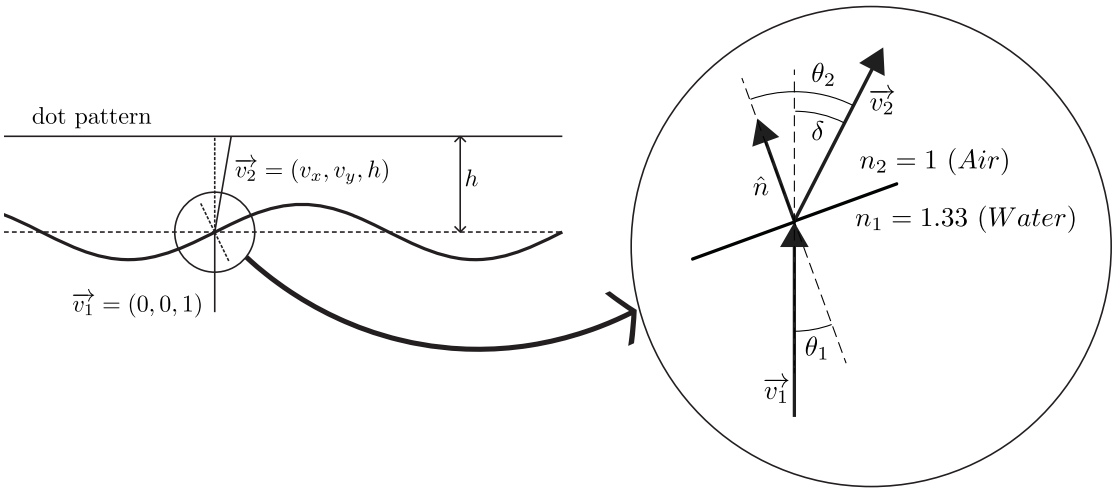

Figure 2.7: Refraction at the air-water interface (drawn in 2-D for simplicity).

the right side of figure 2.7. Now define θ_1 as the angle between the incident ray and the surface normal, θ_2 as the angle between the refracted ray and the surface normal and δ as the difference between θ_1 and θ_2. Using the Snell's law, we have

$$n_1 \sin(\theta_1) = n_2 \sin(\theta_2) \tag{2.3}$$

$$\delta = \theta_2 - \theta_1 = \cos^{-1}(\mathbf{v_1} \cdot \mathbf{v_2}) \tag{2.4}$$

$$n_1 \sin(\theta_1) = n_2 \sin(\theta_1 + \delta) \tag{2.5}$$

$$\theta_1 = \tan^{-1}(\frac{n_2 \sin(\delta)}{n_1 - n_2 \cos(\delta)}) \tag{2.6}$$

where n_1 and n_2 are the refractive indices of the two media (in this case water and air respectively). Normal vector $\hat{n}$ is then found by rotating the vector $\mathbf{v_1}$ around the axis given by $\mathbf{v_1} \times \mathbf{v_2}$ with angle θ_1. If the free surface shape is defined as $z = f(x, y)$ and $\hat{n} = (n_x, n_y, n_z)$, we get $f_x = -\frac{n_x}{n_z}$ and $f_y = -\frac{n_y}{n_z}$ where $\bigtriangledown f = (f_x, f_y, -1)$.

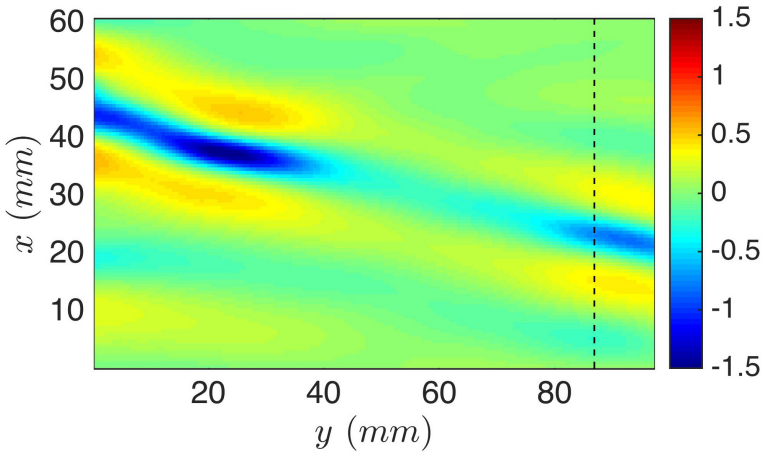

Figure 2.8: Free-surface elevation (in mm) for the image pair in figure 2.5. The dashed line is the approximate location of the laser sheet that is used for the LIF measurements.

An inverse gradient algorithm called "intgrad2" is then utilized to integrate the surface normal field and obtain the first estimate of the three-dimensional shape of the surface (see Moisy *et al.* (2009) for details). In order to have an absolute measurement of the surface height, a reference height is required as the integration constant. This reference height was measured using a cinematic LIF technique as explained below. Once the first approximation of the surface height map is calculated, the surface normal vectors can be recomputed using the map of calculated local distance between the water surface and the dot pattern. The procedure to find the surface height map is then repeated. In validation tests, it was found that three iterations of this procedure are usually enough for convergence. The calculated surface elevation map for the images in figure 2.5 are shown in figure 2.8.

A cinematic Laser-Induced Fluorescence (LIF) method was used to measure

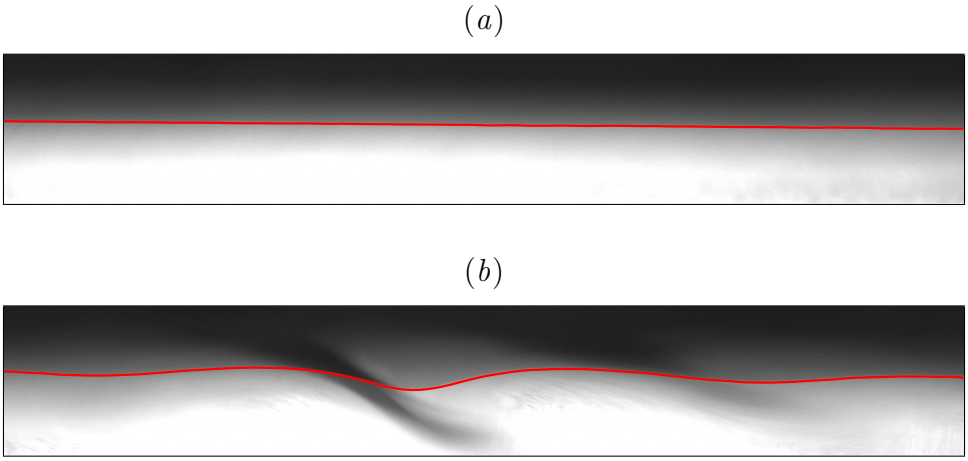

Figure 2.9: Sample images from the LIF method. These images are about 5 cm wide. The red lines are the calculate free-surface profiles after image processing. (a) Calm water surface. (b) Disturbed surface.

the wave height along a line inside the measurement field of the refraction-based method, see figure 2.2. In order to perform these measurements, Fluorescein dye is added to the water and a thin sheet of light from an argon-ion laser is projected vertically onto the water surface from below. The light sheet is about 20 cm wide and 1 mm thick and the plane of the light sheet is oriented in the direction of the carriage motion. A second camera is mounted on the carriage (camera 2 in figure 2.2) and views the intersection of the light sheet and the free surface through the side wall and from above the surface, looking down with an angle of about 15 degrees from the horizontal. The image resolution of this camera was 50 pixels per millimeter. This camera is triggered simultaneously with the refraction method camera via the laser trip device.

A gradient-based method for edge detection combined with dynamic program-

ming (Amini *et al.* (1990); Duncan *et al.* (1999); Kass *et al.* (1988)) is utilized to find the free surface shape along the image of the intersection of the laser sheet with the water surface. This method starts with an initial guess for the profile and tries to minimize a local energy functional to find the optimum profile. The energy functional consists of an internal energy and an external energy. The internal energy term keeps the profile smooth and connected and the external energy moves the profile towards image features (in this case edges). A sequence of about 5500 images are taken in each run. To improve the speed and accuracy of the program, the wave profile from each image is used as the initial guess for the next image in the sequence. The first image in each movie is taken during the carriage acceleration and therefore the free surface is still calm and the program is allowed to search for 20 pixels away from the initial guess. Since the movies are taken at a high frame rate, the change in the shape of the profiles in consecutive images is very small and it was decided to allow the program to search only 1 pixel away from the initial guess after the first image. The structure that holds the water tank blocks the view of the camera at three places during each run. For the first image after each blockage, the search window size is again set to 20 pixels. A sample pair of LIF images, one taken with the air jet off and the other with the jet on, are shown in figures 2.9(a) and (b), respectively. These images are for the same instants in time as the dot pattern images in figure 2.5. The calculated profiles are also plotted on top of the images.

The vertical vibration in the carriage motion affects the wave profile measurements from the LIF technique. In order to reduce the error, first each wave profile extracted from individual frames is smoothed in the x-direction using Savitzky-

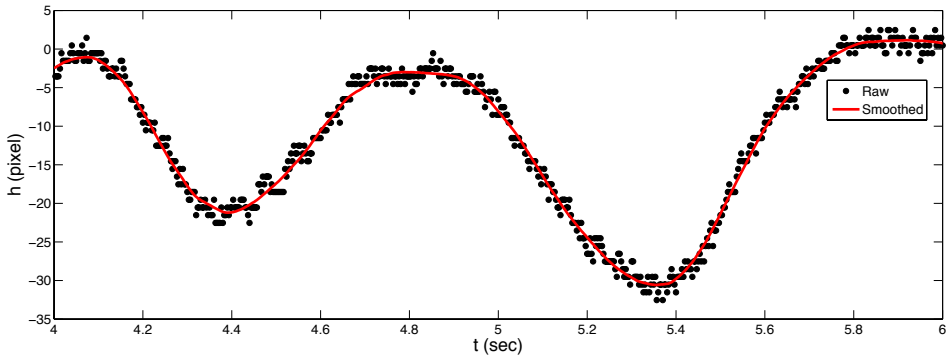

Figure 2.10: An example of smoothing done on the raw data from image processing (see text for details)

Golay filtering. Then, the height signal at each pixel location was smoothed in time. Figure 2.3 shows a sample signal of the surface height from one pixel column on the camera sensor and the red line is the result of the smoothing. Using this method we are confident that the measurement error for the LIF technique is within one camera pixel or about ± 0.02 mm in the physical space.

Since the cameras used for the refraction method and the LIF method are triggered simultaneously, there is an LIF image pair, with the air jet on and off, for each refraction image pair. Thus, for each image pair from camera 1, the surface shape along the laser sheet is known from camera 2 and is used as the integration reference to obtain the free surface elevation map. Because the structure holding camera 1 is so far below the carriage, the camera tends to vibrate during each run creating an oscillating uniform pixel displacement with an amplitude of about 6 pixels primarily in the streamwise direction. This oscillation creates a fictitious mean slope of the computed surface height maps. This slope is removed by using

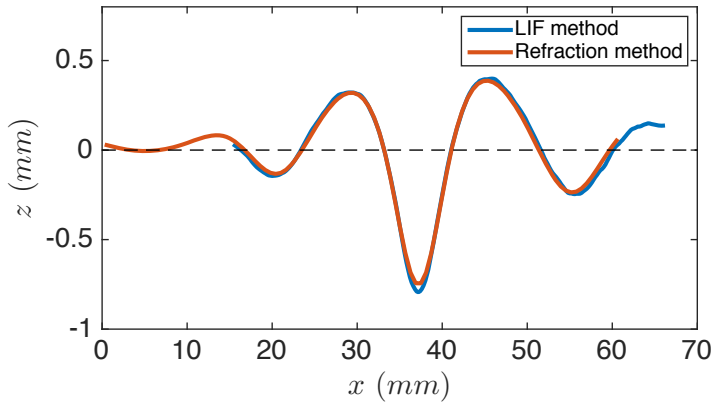

Figure 2.11: Comparison between the results of the LIF method and the refraction method for the images in figures 2.5 and 2.9.

the LIF reference line.

The accuracy of the refraction method can be estimated by comparing the profile along the laser sheet with the LIF profile at the same instant. In figure 2.11, surface profiles from the sample images of figures 2.8 and 2.9 are plotted in the same coordinate system. The maximum difference in surface height between the two methods in a test run (5500 frames) had an RMS value of 0.066 mm or about 6 percent of maximum depth.

For the quantitative measurements of the state III deformation patterns, the following experimental conditions and measurement settings were used. In order to obtain accurate measurements with the refraction method, the dot image displacements should be large enough that they can be measured accurately but not so large that the images of single dots become distorted or refracted light rays cross before reaching the dot pattern. As described above, dot image displacements increase

with increasing distance (h_d) between the mean water surface and the dot pattern and with increasing surface slope, which is controlled partially by the forcing parameter (ϵ). By trial and error, it was determined that with the tip of the air-jet tube located 7 mm above the mean water level accurate measurements were obtained with $h_d = 5.4$ mm and $\epsilon = 0.24$. These conditions were used for all of the full-field quantitative surface deformation pattern measurements. In these experiments, the towing speed of the carriage was varied between 21.9 cm/s and 23.5 cm/s with a step of 0.1 cm/s. The field of view of the camera 1 was about 60 mm in the streamwise direction and 100 mm in the cross-stream direction and was located on one side of the pressure source, hence looking at half of the wave pattern. For each condition, each "run" consisted of four movies (5500 frames for each movie at 300 frames per second) including two movies for each camera, one with the air-jet off and one with the air jet on. Three "runs" were carried out and processed for each towing speed

The distorted dot pattern images can also be used to obtain a qualitative understanding of the surface shape without image processing. For these observations, h_d was increased so that the dot image displacements were large and the dot images were distorted into lines at locations with high surface slope. These high-distortion images are used to observe the free surface deformation in the state II-III boundary and to measure the shedding period of the depressions in state III (see §2.5.1 and §2.5.3). For these experiments, α was varied from 0.779 to 1.016 and ϵ was varied from 0.24 to 0.63.

2.4 Numerical model

The model equation derived by Akers & Milewski (2009) and extended by Cho *et al.* (2011) was used alongside the experimental results to investigate some features of the unsteady response to a moving pressure source. This equation is devised to capture the main effects of nonlinearity, dispersion and dissipation in the system and the interplay between them. Velocity and length are scaled by $c_{\min}$ and $1/k_{\min}$, respectively. In a coordinate system moving with the source ($\xi = x + \alpha t$ and y), the free-surface elevation η is governed by

$$\eta_t - \tilde{\nu}(\eta_{\xi\xi} + \eta_{yy}) + (\alpha - \tfrac{1}{2})\eta_\xi - \beta(\eta^2)_\xi - \tfrac{1}{4}\mathscr{H}\{\eta_{\xi\xi} + 2\eta_{yy} - \eta\} = Ap_\xi, \qquad (2.7)$$

where $\mathscr{H}$ denotes the Hilbert transform, $\tilde{\nu}$ controls the viscous damping and A controls the peak amplitude of the pressure distribution p. A quadratic nonlinearity is used and the coefficient of the nonlinear term is set to

$$\beta = \sqrt{11/2}/8 \qquad (2.8)$$

to be consistent with the weakly nonlinear theory in the small-amplitude limit. The pressure distribution is assumed to have the Gaussian form

$$p(\xi, y) = \exp(-2\xi^2 - 2y^2). \qquad (2.9)$$

Numerical solution of equation 2.7 was obtained using a spectral method in space and a predictor-corrector method in time as described in Cho (2010). The computational domain was $-37.7 < \xi < 37.7$ and $-62.8 < y < 62.8$ with 512 grid points in each direction and no symmetry was assumed. The time step was set to $\Delta t = 0.001$.

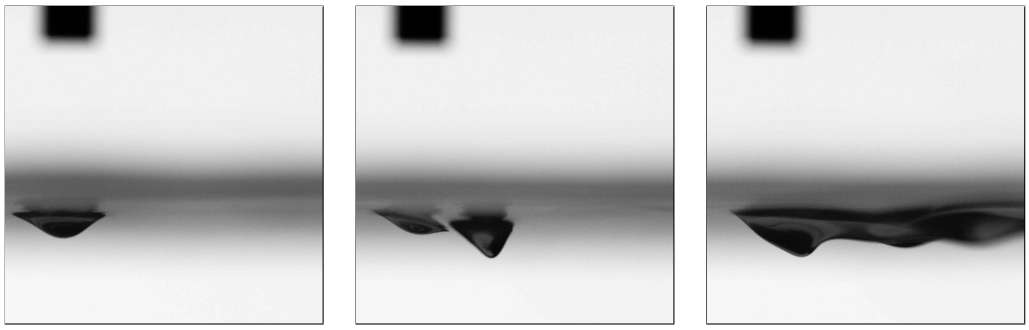

(a) (b) (c)

Figure 2.12: Shadowgraph images from camera 1 for $\epsilon = 0.36$ and three values of α. The camera is focused through the water on the depression. The air-jet tube, which is moving from right to left, is also visible in the upper left of each image, but it is out of focus since it is viewed through air. (a) $\alpha = 0.82$. State I response: a small dimple beneath the air-jet tube. (b) $\alpha = 0.93$. State II response: a steady lump behind the tube. (c) $\alpha = 0.97$. State III response: An extended unsteady pattern behind the tube.

2.5 Results and discussion

2.5.1 State diagram

Qualitative observations of the shape of the free-surface deformation pattern were made for a wide range of α and ϵ. These observations were carried out by using both the underwater shadowgraph movies and the refraction method movies. The shadowgraph movies are well suited for observing state I, state II and the state I-II boundary (see figure 2.12), while the refraction movies are well suited for observing state III and the state II-III boundary (see figure 2.13). The final result of this

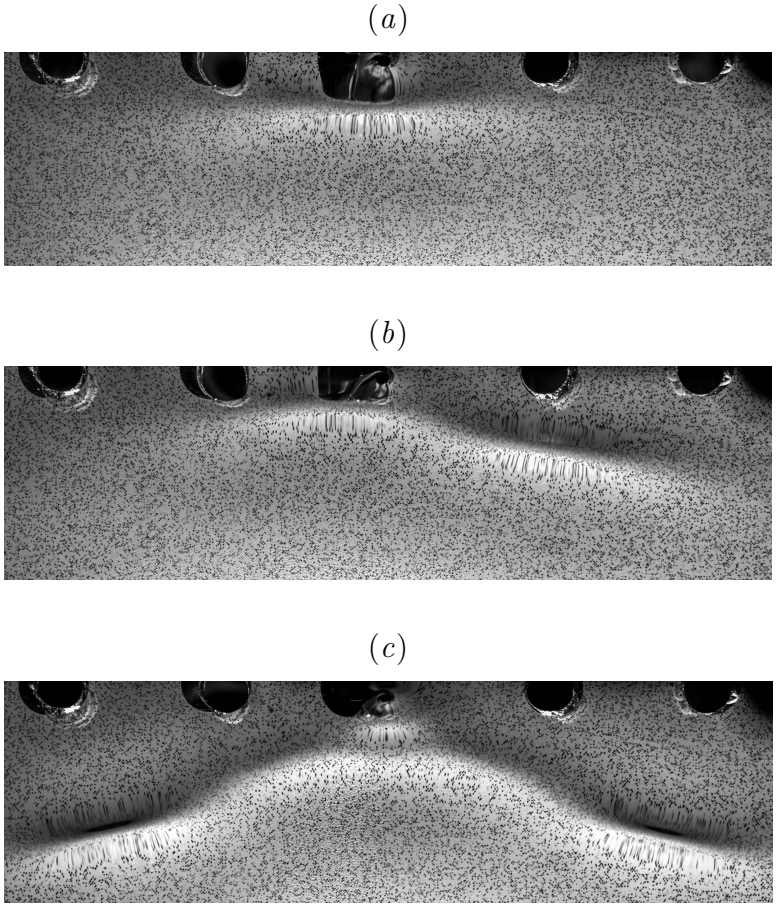

Figure 2.13: Refraction images of the deformation pattern behind the air-jet tube for $\epsilon = 0.24$ and $\alpha = 0.930$, 0.964 and 0.986, corresponding to state II, the state II-III boundary and state III, are shown in (a), (b) and (c), respectively. The dark circles along the top of each image are holes where the air-jet tube can penetrate the dot pattern. In the images shown here, the air-jet tube is located in the center hole and the carriage is moving from the bottom to the top of the page. The distance between the dot pattern and the water surface is relatively large to make the distortions more obvious for qualitative visualization. The width of each image is about 9 cm in the physical plane. The depressions are the dark elongated areas while the adjacent regions where the dots are stretched are regions of high surface slope.

work is the state map in the α-ϵ plane shown in figure 2.14. This state map was determined by choosing five values of ϵ and for each ϵ, starting with an α such that a state I response occurred, increasing α in steps of 0.02 and recording the state as it changed for I to II to III. The boundary regions between states were then explored in smaller steps of α and frequently with repeated experimental runs. The state I, II and III responses as seen in shadowgraph images are shown in figure 2.12(a), (b) and (c), respectively. The state I response is a steady dimple under the air jet; the state II response consists of a steady dimple under the air jet followed by a steady deeper depression behind the air jet; and the state III response is an unsteady deformation pattern that is elongated in the downstream direction. Similar observations were reported by Diorio *et al.* (2011). The state II and state III responses are also shown in the refraction images in figure 2.13(a) and (c), respectively. In figure 2.13(a), the state II response is difficult to see because it is under and very close behind the air jet at the top center of the image; however, the state III response in figure 2.13(c) is seen much more clearly than in the shadowgraph image in figure 2.12(c).

Between states I and II and between states II and III, there are boundary regions of finite thickness in α where the response is clearly not consistently one of the three states. In the state I-II boundary region, the surface deformation pattern oscillates between states I and II, as discussed by Diorio *et al.* (2011). In the present work, it is found that the thickness of this boundary region is about 0.02 in α. In the state II-III boundary region, the surface shape is highly oscillatory (especially at large ϵ values) and features an extended pattern that is asymmetric with respect to the vertical streamwise plane going through the air jet tube, see figure 2.13(b).

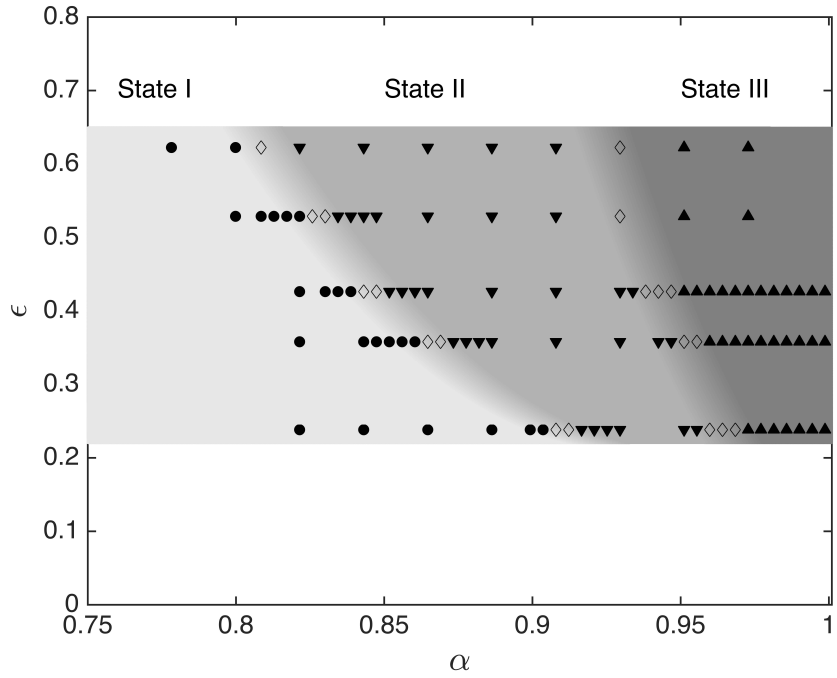

Figure 2.14: State diagram in the α–ϵ plane: ● – state I, ▼ – state II, ▲ – state III, and ◇ – state I-II transition on the left and state II-III transition on the right. In the state I-II transition region, the response is sometimes in state I and sometimes in state II. In the state II-III transition region, the deformation pattern is unsteady with asymmetric and irregular shedding of localized depressions. Estimates of the locations of the state boundary regions are indicated by a gradient in the image grey level.

In experiments with $\epsilon = 0.24$, localized depressions are generated alternately from the left and right sides of the centerline and decay quickly before moving very far from the pressure source. For $\epsilon = 0.36$ and 0.43, the surface pattern features large-amplitude localized depressions close to the pressure source. These depressions are highly oscillatory and often seem to disappear as they radiate small-amplitude waves. The α values for both the state I-II and state II-III boundaries decrease with increasing ϵ.

2.5.2 Evolution of free-surface shape in state III

The evolution of the three-dimensional shape of the free surface in state III was measured with the refraction-based method described in §2.3 for $\epsilon = 0.24$ and α values ranging from 0.946 to 1.016. Sequences of surface elevation patterns for α=0.986, 0.994 and 1.003 are shown in figures 2.15, 2.16 and 2.17, respectively, in a reference frame moving with the pressure source. The time separation between the plots in each figure is $\Delta t = 0.3$ seconds. The pressure source is located at the origin (shown as a black dot) and is moving in the positive x-direction in the laboratory reference frame. In the following, both general observations and quantitative aspects of the deformation pattern are discussed.

In each run, as the carriage reaches its final speed, a V-shaped pattern appears behind the source and a pair of isolated depressions form at the tips of the V. These depressions, which appear as blue ovals in figure 2.15, are oriented with their long axes making an angle of about 15 degrees in the clockwise direction relative to the

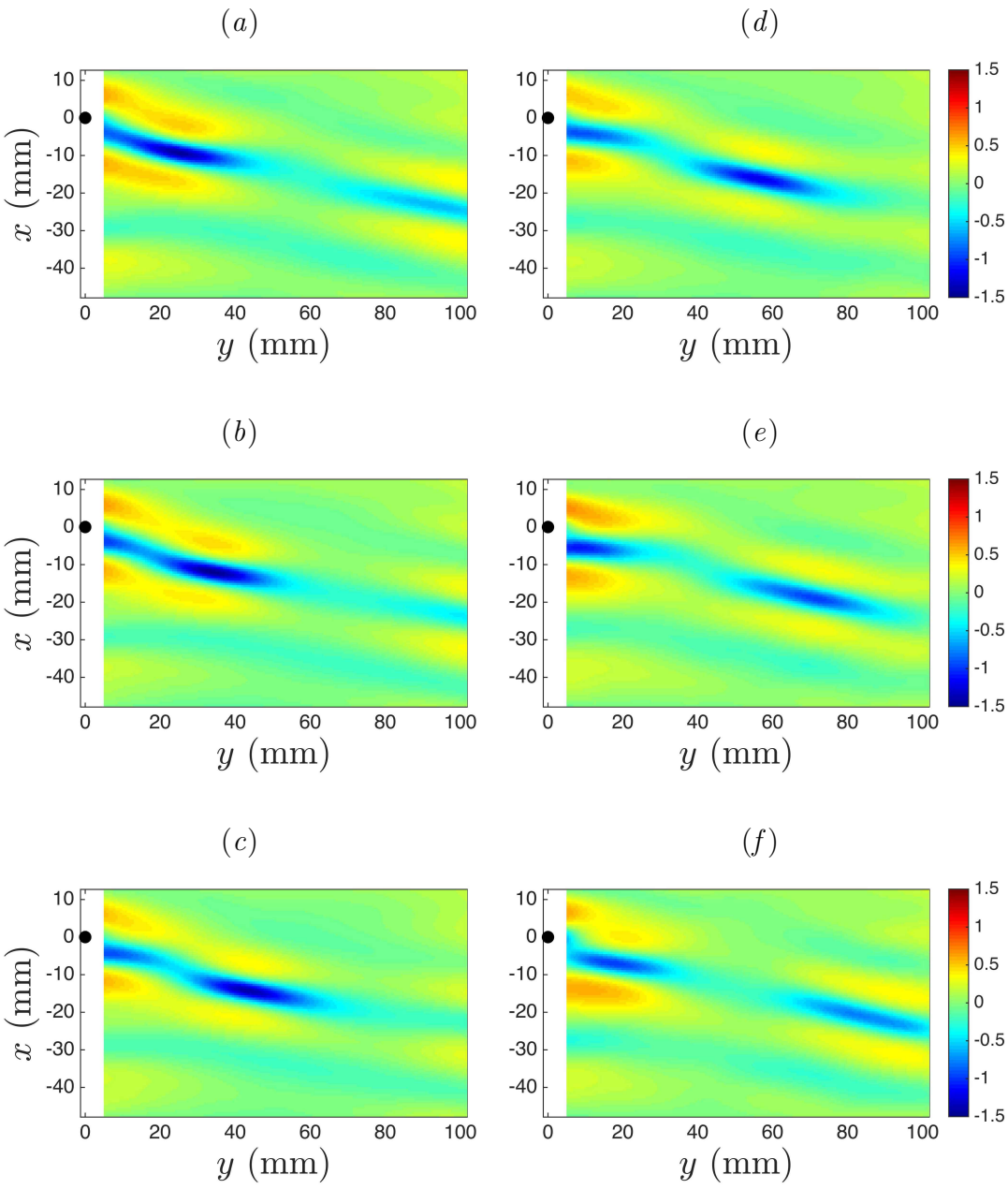

Figure 2.15: Snapshots of free-surface elevation (in mm) for $\epsilon = 0.24$ and $\alpha = 0.986$. The air-jet tube is located at the origin (shown as a black dot) and is moving in the positive x-direction. The time separation between figures is 0.3 seconds.

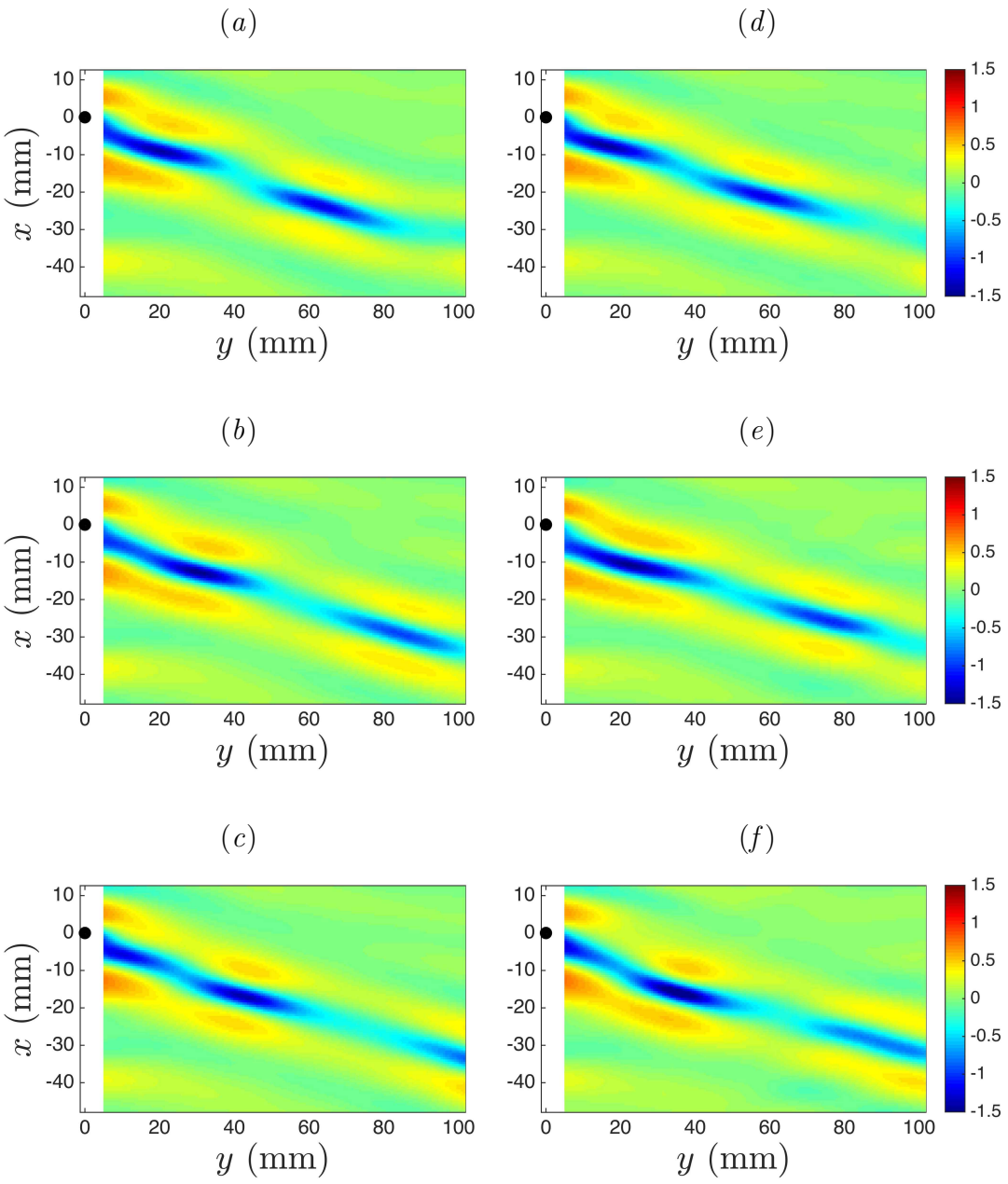

Figure 2.16: Snapshots of free-surface elevation (in mm) for $\epsilon = 0.24$ and $\alpha = 0.994$. The air-jet tube is located at the origin (shown as a black dot) and is moving in the positive x-direction. The time separation between figures is 0.3 seconds.

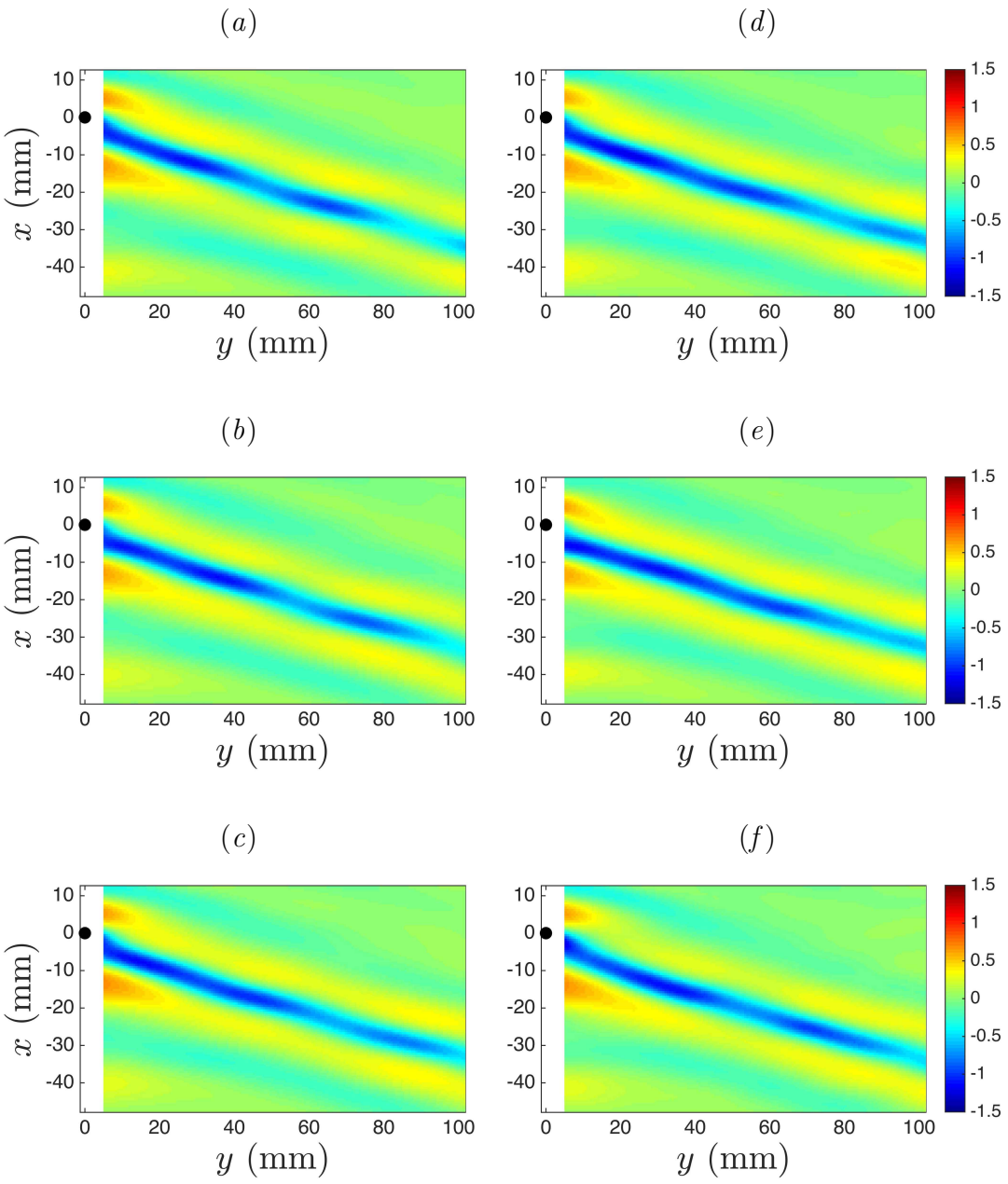

Figure 2.17: Snapshots of free-surface elevation (in mm) for $\epsilon = 0.24$ and $\alpha = 1.003$. The air-jet tube is located at the origin (shown as a black dot) and is moving in the positive x-direction. The time separation between figures is 0.3 seconds.

cross-stream direction. In the reference frame of the air-jet tube, the depressions move away from the source in approximately the direction of their long axis; in the laboratory reference frame they propagate in the direction perpendicular to their long axis. This angle increases slightly with increasing towing speeds. The maximum depth of each depression increases as it is generated, but as it moves away from the source, the maximum depth decreases and the depressions seem to move at a faster rate. This process is repeated during the entire run as depressions are periodically shed and quickly damp out.

At lower towing speeds, the shedding events are isolated and separate depressions move away from the source and decay (figure 2.15), while at higher speeds, the shedding occurs more frequently and new depressions are shed before the previous depressions have moved far from the source (figure 2.16). Hence, as the towing speed is increased each depression is more likely to interact with its neighbors. The behavior of depressions is quite complicated. For example, they can suddenly speed up or slow down, change shape or merge with another localized depression. This behavior is probably due to these interactions.

As the towing speed is increased above $c_{\min}$, the depressions become shallower and the shedding becomes even more frequent. Here, it is difficult to recognize individual isolated depressions, especially at later times during a run (figure 2.17). For $\alpha > 1.02$, the pattern starts to look similar to the steady V-shape pattern of linear theory. Quantitative measurements of the shedding period are discussed later.

From the surface elevation plots in figure 2.15, it is observed that the three-dimensional shape of the isolated depressions in state III resembles the shape of the

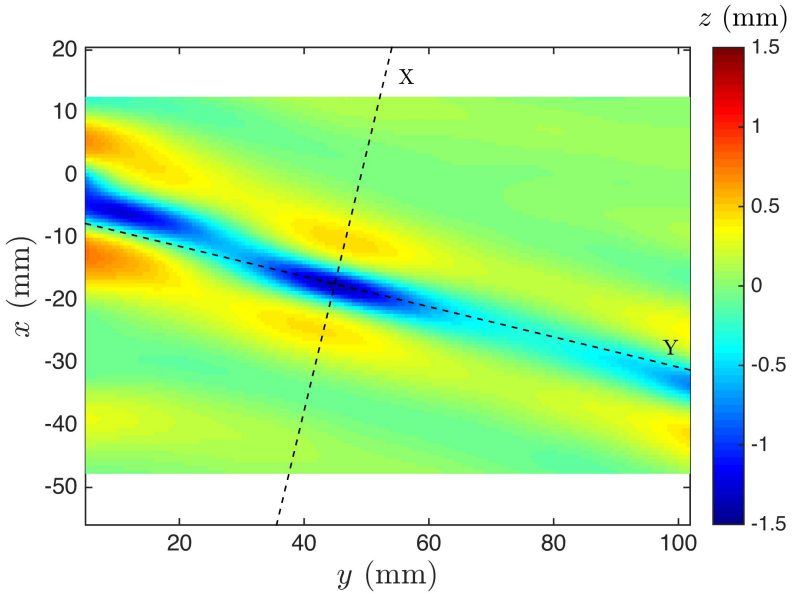

Figure 2.18: The modified coordinate system for a state III localized depression with $\alpha = 0.986$ and $\epsilon = 0.24$.

lumps in state II measured by Diorio *et al.* (2011) and the freely propagating steady lumps from potential flow calculations by Părău *et al.* (2005). To better illustrate the shape of the state III depressions, the two-dimensional profiles along the axes of symmetry of the depressions are calculated. The cross-stream direction (Y-axis) is defined by fitting a line to the location of the maximum depth in each y-position in the vicinity of the maximum depth of the depression. The streamwise direction (X-axis) is perpendicular to the Y-axis and intersects with it at the position of the maximum depth of the depression (see figure 2.18). The profiles along the X and Y axes are plotted in figure 2.19-(a) and show remarkable similarity to the freely propagating lumps of Părău *et al.* (2005) shown in figure 2.19-(b). Note that the steady lumps in state II and the freely propagating lumps in Părău *et al.* (2005)

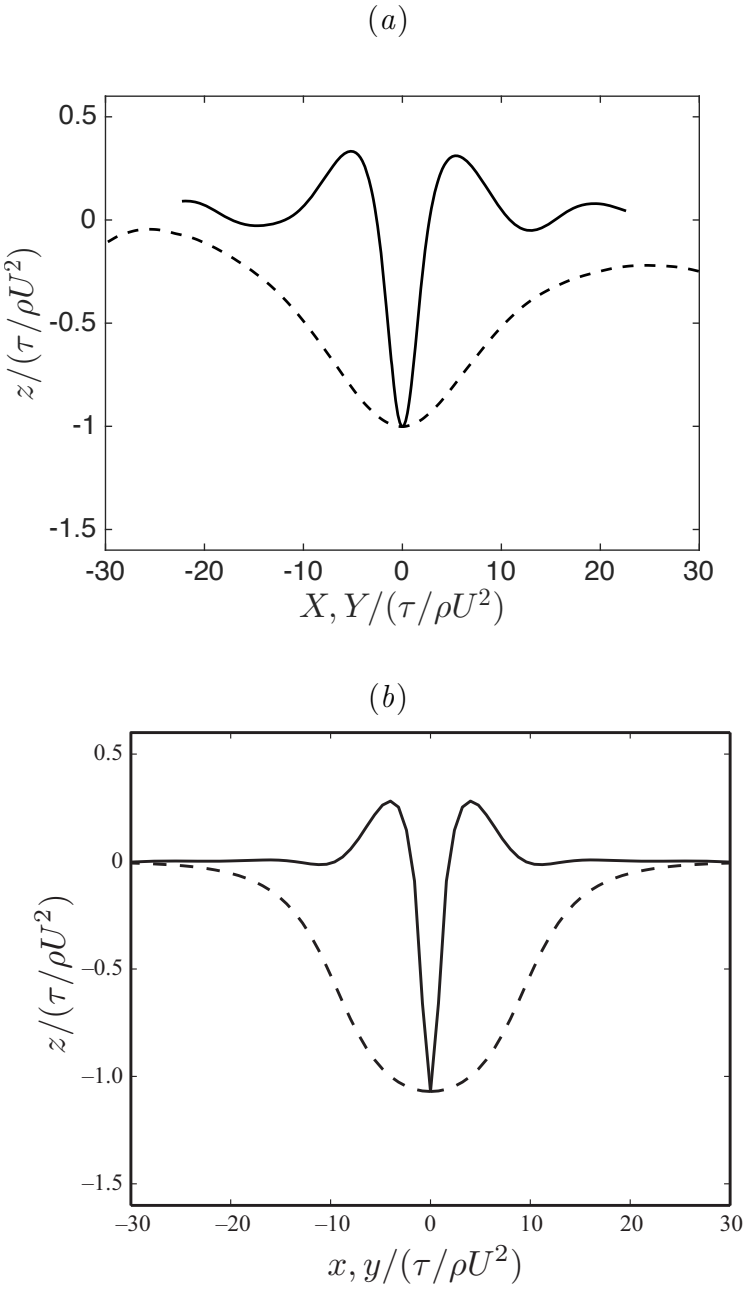

Figure 2.19: (a) Profiles along the main axes of the lump shown in figure 2.18 in dimensionless form. The solid line is the profile in the streamwise (X) direction and the dashed line is the profile in the cross-stream (Y) direction. (b) Profiles of a steady freely propagating lump from inviscid potential flow calculations by Părău *et al.* (2005) for $\alpha = 0.919$.

are highly localized in all directions and the surface height approaches zero away from the center of the lump. However, in state III, the depressions are not fully isolated and are probably interacting with one another. This is especially clear in the cross-stream profile (dashed line).

One of the well-known features of solitary waves is the one-to-one relationship between their speed and amplitude. Resonantly forced lumps of state II move at the same speed as the pressure forcing and a monotonically decreasing relation between their maximum depth and the towing speed was found in the experiments of Diorio *et al.* (2011). A similar relation was found in the inviscid potential flow calculations of freely propagating steady lumps by Părău *et al.* (2007). One wonders if such a relationship exists for the state III depressions as well.

Unlike the lumps in state II, the speed and depth of a depression in state III are not constant – each depression undergoes both smooth and erratic changes in these quantities. The erratic behavior is probably due to interactions with previous and subsequent depressions, see above discussion. Furthermore, obtaining instantaneous velocity from the position of the maximum depth of a depression often results in noisy data. To overcome this latter issue, a quasi-steady behavior is assumed for the depressions: the velocity for each depression is estimated by locally fitting straight lines to position versus time data as the the depression depth passes through each of a specified set of equally spaced depths between 0.6 mm and 1.4 mm. To reduce noise in determining the location of the maximum depth of a depression, the surface shape was approximated by fitting a quadratic surface to a small area around the central region of the depression and the location of the maximum depth of the fitted

surface was used for further processing. Each depression is tracked in this way until it moves out of the field of measurement or its depth becomes smaller than 0.5 mm.

This measurement was performed for 373 individual depressions observed in all the runs with $0.977 \leq \alpha \leq 1.016$. Results are plotted in figure 2.20. The depression depth, h, is normalized by the wavelength of a linear wave at the minimum phase speed ($\lambda_{\min}$=1.71 cm). In this plot, each grey dot represents the velocity of a lump at one of the prescribed depression depths. The black squares are the average speeds for each depth and the error bars are the standard deviations. As expected, the grey dots are dispersed over a relatively large area due to the uncertainty in the speed measurement and the erratic behavior of the depressions. However, in an average sense, the behavior of the unsteady lumps of state III is remarkably similar to that of the inviscid and steady free lumps of Părău *et al.* (2007) (shown as triangles in the plot) and the forced steady lumps of Diorio *et al.* (2011) (shown as the dashed line in the plot). Given the shape and depth-speed characteristics of the depressions, they appear to be freely propagating gravity-capillary lumps.

As mentioned earlier, the lumps in state III first form and then decay quickly as they move away from the pressure source. The decay properties of these lumps were measured by tracking their maximum depth in time. In order to measure lump behavior that is likely to be similar to that of freely propagating lumps, conditions where the lump in question was far from any neighbors were chosen. To achieve this, two criteria were met. First, only the first lump in each run was considered since these lumps propagate into relatively undisturbed water. Second, an experimetnal condition with a long shedding period ($\epsilon = 0.24$ and $\alpha = 0.986$, see figure 2.15)

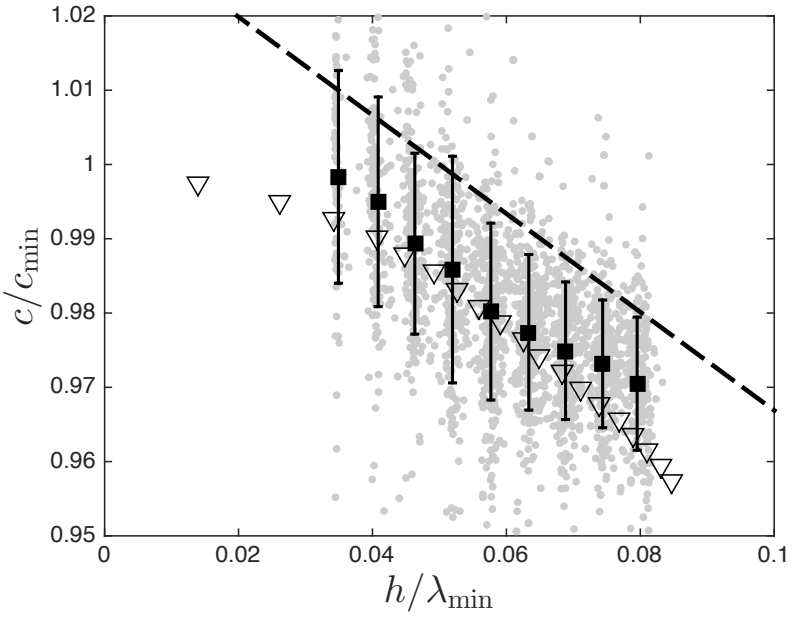

Figure 2.20: Speed of the depressions (normalized by $c_{\min}$) in the reference frame of the laboratory versus the maximum depth of the depressions (normalized by $\lambda_{\min}$). The grey dots are the velocity of a given state III depression in each band of depression depths. ■ Average speed for each depth band. The error bars are the standard deviations. ▽ Potential flow calculations of Părău *et al.* (2007) for freely propagating lumps. −− Linear fit from the experimental data for forced lumps in state II from Diorio *et al.* (2011).

was chosen so the next lump shed was far behind the first lump. A plot of depression depth (h on a logarithmic scale) versus time for several lumps meeting these conditions is shown in figure 2.21. The three sets of black triangles are from three experimental runs in which the camera's field of view was close to the pressure source. For these runs, the depth increases at first as the lump is formed and then starts decreasing once it becomes detached from the local depression region. It was observed that the first shedding events in separate runs are not exactly repeatable. Therefore, the data points from separate runs are shifted in time (by no more than 0.15 seconds) to form a better match between runs. The gaps in these data sets for $4.5 \lesssim t \lesssim 5$ s are due to blockage of the camera's line of sight by one of the water tank's structural elements.

In order to track the depth of the lumps for later times, the camera was moved laterally away from the air-jet tube and the distance between the dot pattern and the water surface was increased to obtain a more accurate measurement of small surface deformations. Furthermore, the starting position of the carriage motion was set to a new location so that the tank structure would not block the camera view. The results for the first lump in four separate runs are shown as open circles in figure 2.21, along with the previously discussed data. An exponential decay function in the form of $h(t) = A\exp(-\sigma t)$ was fitted by the least squares method to the data from these four runs and is plotted as a dashed line in the figure. The calculated decay rate is $\sigma = 1.11$ s^{-1}. Thus, a lump loses about 63 percent of its initial depth after about 0.90 s, a time over which it propagates approximately $0.90c_{\min} = 20.8$ cm. A similar decay time was predicted from numerical results obtained with the model

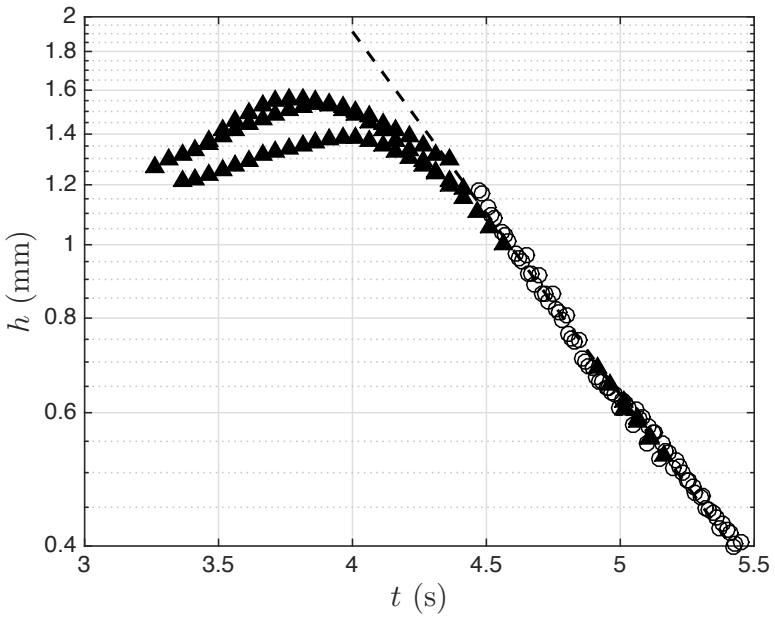

Figure 2.21: Maximum depth of first lumps (h) versus time (t). The time $t = 0$ is approximately the instant when the carriage starts its motion. Data from separate experimental runs with $\epsilon = 0.24$ and $\alpha = 0.986$ are shown. The black triangles (open circles) are from measurements with the camera field of view close to (far from) the pressure source. The dashed line is a least-squares fit of an exponential decay law to the open circles. The exponential decay rate calculated from this fit is $\sigma = 1.11\ \mathrm{s}^{-1}$. The accuracy of the depth measurements is ± 0.06 mm.

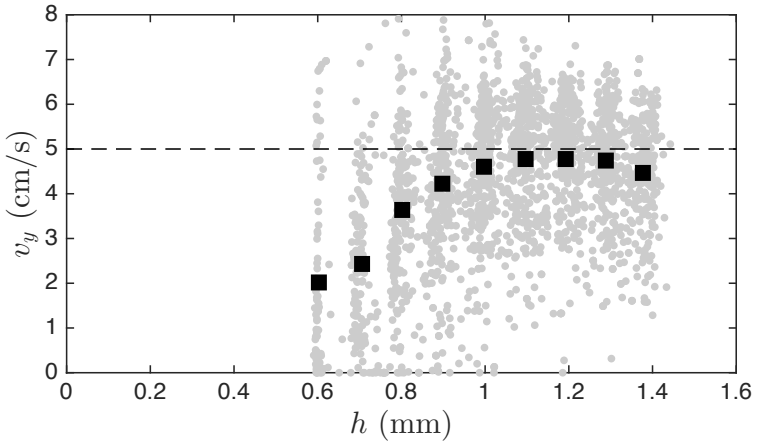

Figure 2.22: Cross-tank component of lump velocity (v_y) versus h for all lumps.

equation in Cho *et al.* (2011). This short characteristic decay time may partially account for the scarcity of reported observations of lumps in nature.

The measurements of the speed, propagation direction and decay rate of the lumps can now be used to verify that the tank width is sufficient to avoid the influence of sidewall reflections on the experimental results. In this verification, the decay of h as a lump travels laterally over a distance of one-half of the tank width is calculated. The measurements of the cross-tank components (v_y) of the lump velocities are shown in Figure 2.22. As can be seen in the figure, the highest average v_y values are about 5 cm/s. Given the tank half-width of 15 cm, the transit time would be about 3 s. In this time, h would decay by a factor of $e^{-3.0\sigma} = 0.036$. Thus, the tank wall reflections should have minimal influence on the results.

The effects of α and ϵ on the shedding period in state III were also investigated by using dot pattern image sequences with large distortions (see figure 2.13c). The instantaneous period (T) was taken as the time difference between the passage of

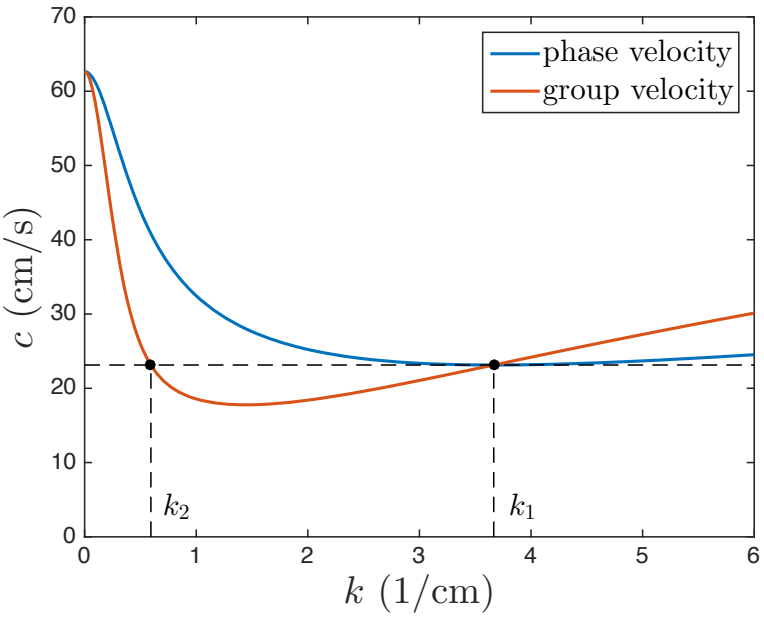

Figure 2.23: The shedding period is scaled with the period of a wave component whose group velocity is equal to the minimum phase speed. There are two wavenumbers, k_1 and k_2, that satisfy this criterion.

two successive lumps across fixed vertical lines near both sides of the images and an average of these T values over each run was taken as the shedding period $\overline{T}$ for each experimental condition. A reference time, T^*, based on linear theory was chosen to nondimensionalize the shedding period data. In choosing T^*, it was noted that in linear theory when a source starts from rest and reaches a steady speed, the unsteadiness of the wave pattern can be partially due to a wave component whose group velocity c_g is equal to the towing speed U. In the present scaling idea, only a single time scale is desired, rather than one for each towing speed, so this wave component is taken as the one for which $c_g = c_{\min}$. For the Bond number in these experiments ($Bo = 0.00465$), there are two values of k that satisfy this criterion, $k_1 = k_{\min}$ and $k_2 = 0.594$ cm$^{-1} = 0.162 k_{\min}$ (see figure 2.23). At k_1, $c = c_{\min} = c_g$ so the period of this wave would be infinite in the reference frame moving with speed $c_{\min}$. At k_2, $T = 0.259$ s $= 3.40 T_{\min}$ in the laboratory reference frame and 0.598 s in the reference frame moving at speed $c_{\min}$. This latter period is taken as the reference time scale T^*.

Curves of nondimensional shedding period, $\overline{T}/T^*$, versus α are plotted in figure 2.24 for $\epsilon = 0.24$, 0.36 and 0.43. As can be seen from the figure, the curve for $\epsilon = 0.24$, begins at $\alpha = 0.973$, the right side of the state II-III boundary in figure 2.14, with a shedding period of $\overline{T}/T^* \approx 6.8$. The value of $\overline{T}/T^*$ then decreases monotonically to about 1.7 at $\alpha = 1.008$. At the same time, the magnitude of the slope of the curve decreases monotonically, becoming nearly zero for $\alpha > 1.0$. The curves for $\epsilon = 0.36$ and 0.43 start at $\alpha \approx 0.96$ with $\overline{T}/T^* \approx 3.0$ and are nearly identical. As α increases, $\overline{T}/T^*$, decreases monotonically, reaching a value of about

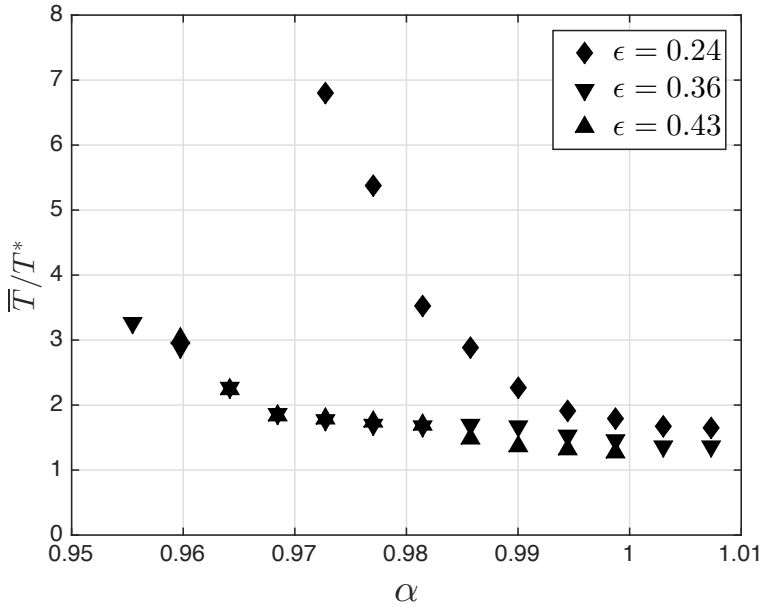

Figure 2.24: The nondimensional shedding period ($\overline{T}/T^*$) of state III lumps versus the towing speed parameter (α) for three values of the forcing parameter (ϵ). $\overline{T}$ is the average lump shedding period and $T^*(= 0.598$ s) is a reference time scale based on linear wave theory as described in the text. The standard deviation of the measured periods during a single run was about ± 0.3 s for low values of α and decreased to about ± 0.1 s for $\alpha \approx 1.0$.

1.4 at $\alpha = 1.008$. These curves are also nearly level for $\alpha > 1.0$. The fact that the two curves for the higher values of ϵ are nearly equal and very different from the curve for the lowest value of ϵ indicates an insensitivity to the effects of nonlinearity beyond a certain level of forcing. The fact that the curves for all three values of ϵ nearly converge to $\overline{T}/T^* \approx 1.5$ as $\alpha \to 1.0$, may indicate that the nonlinearity, which is of primary importance for creating the surface response at lower values of α, causes only a modification to linear theory for $\alpha \gtrsim 1$. In fact, for the cases with $\alpha > 1.0$ the oscillation may be primarily a starting transient, as is discussed further below.

The longevity of the lump shedding was addressed through the experimental measurements and the results from the model equation described in §2.4. A shedding cycle from the numerical simulations is shown in figure 2.25. The forcing parameters used in the model equation, A, has to be tuned to produce similar results to the experiments. Cho *et al.* (2011) tuned this parameter to match the jump conditions between the three states in the experiments. In our numerical tests, we found that the boundary between state II and state III varies only slightly when forcing is increased (see figure 2.14) but the period of shedding is very sensitive to the changes in forcing parameters. In order to obtain more accurate results from the model equation, we tried to tune the forcing parameter to obtain a reasonable match for the shedding period as well as the jump conditions.

Typical results are shown in four plots of minimum surface height at the cross-stream position of $y = 60$ mm versus time in figure 2.26. In this figure, the top plot is from an experimental run with $\epsilon = 0.24$ and $\alpha = 0.994$ and the oscillations

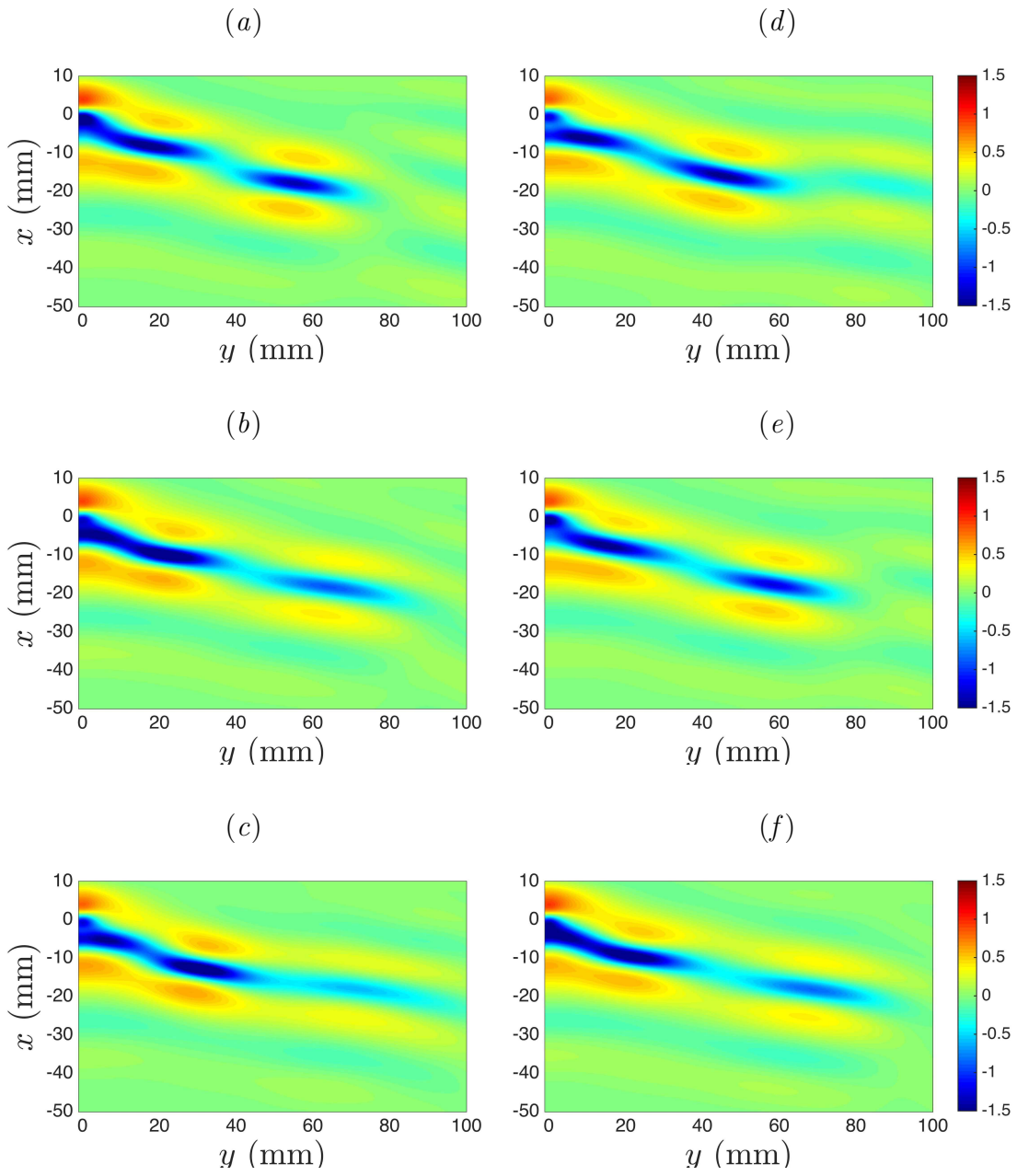

Figure 2.25: Simulation results of the model equation for $A = 0.27$ and $\alpha = 0.994$. The time separation between figures is 0.3 seconds.

in height correspond to the passage of lumps through the designated cross-stream location. These oscillations continue for the entire length of the steady-speed part of the experimental run (18.2 s), which is limited by the present tank length. This result suggests that the shedding of lumps in state III may continue indefinitely. To further investigate the shedding duration at longer times, numerical simulations were performed for a forcing value of $A = 0.27$. The temporal evolution of the pattern was computed for 100 seconds with parameters $\tilde{\nu} = 2.4\tilde{\nu}_0$, where $\tilde{\nu}_0 = 0.003$ is the decay rate of linear sinusoidal waves. For this set of parameters, the α values at the state II-III boundary in the model equation match the values in the experiments when $\epsilon = 0.24$. Calculation results are presented for three values of $\alpha = 0.994$, 1.012 and 1.016, in figures 2.26(b), (c) and (d), respectively. As in the experiments, the minimum height of the pattern at the cross-stream position $y = 60$ mm versus time is plotted in the figures. For $\alpha = 0.994$, full field deformation maps (shown in figure 2.25) indicate the response is clearly in State III and the plot in figure 2.26(b) shows the short time ($0 \leq t \leq 10$ s) and the long time ($90 \leq t \leq 100$ s) part of the surface height record. It is observed that the oscillations become regular and well-defined after about 5 seconds and that the shedding of the depressions continues for the entire numerical run, which is about five times as long as the experimental run. This lends strong support to the idea that the shedding in state III is not a transient phenomenon.

The model equation was also used to investigate the transition from periodic shedding in state III to a steady V-shape response for $\alpha > 1$. It was found that, for the parameters used in the simulations, the amplitude of the oscillations decreases

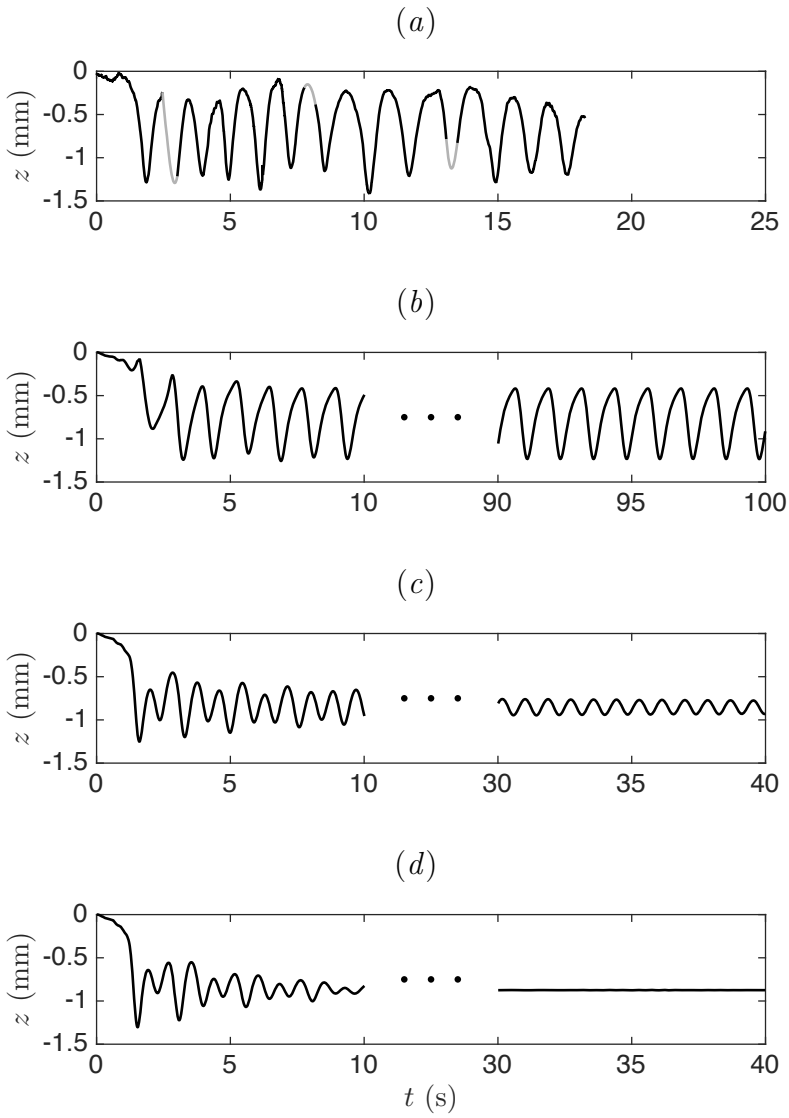

Figure 2.26: Minimum surface elevation at y=60 mm versus time. (a) Experiment with $\epsilon = 0.24$ and $\alpha = 0.994$. Numerical calculations of the model equation with $A = 0.27$ and $\tilde{\nu} = 2.4\tilde{\nu}_0$ for (b) $\alpha = 0.994$, (c) $\alpha = 1.012$ and (d) $\alpha = 1.016$. In the top plot, the grey lines are interpolated data for the locations where the camera view is blocked by elements of the tank structure.

as α is increased above 1, but the periodic behavior continues up to $\alpha = 1.012$ (figure 2.26-c), though, as can be seen in the plot, it takes a relatively long time to become established. For $\alpha > 1.012$ some random oscillations are observed initially, but the response reaches a steady state after about 10 seconds (figure 2.26-d).

The periodic shedding of lumps in state III seems to be analogous to the generation of solitary waves upstream of a source moving near the critical speed of pure gravity waves in shallow water (Wu, 1987). Detailed numerical and experimental results for a surface pressure distribution and a bottom topography moving at trans-critical Froude numbers ($Fr = U/c_0$ where U is the source speed and $c_0 = \sqrt{gH}$) and for a range of forcing parameters are reported in Lee *et al.* (1989). In the following, some aspects of these two types of solitary waves (pure gravity solitary waves and gravity-capillary lumps) are compared and summarized.

In the shallow water case, according to linear theory, the surface response is singular as $Fr = 1$ is approached and no wave response is predicted for $Fr > 1$. Similarly, for the gravity-capillary case in deep water, no linear waves exist for $\alpha < 1$ and the linear response becomes unbounded at $\alpha = 1$. The mechanism of generation of solitary waves for a disturbance moving at a trans-critical speed is described qualitatively by Wu (1987) as follows: "In this trans-critical speed range, the dispersive effect is weak, so the velocity of propagating mechanical energy away (by means of radiating long waves) from the forcing disturbance is about equal to the velocity of the moving disturbance. The local wave will therefore grow as the energy acquired by local fluid at the rate of work by the moving disturbance keeps accumulating. When the local wave reaches a certain threshold magnitude, the

increase in phase speed with increasing amplitude (due to nonlinear effects) will be sufficient to make the wave break away from the disturbance, thus 'born free' as a new solitary wave propagating forward with a phase velocity appropriate to its own amplitude. The process is then repeated over a new cycle." A similar mechanism can be attributed to the periodic generation of lumps in state III. The main difference is that for gravity-capillary solitary waves, the phase speed decreases with increasing amplitude. Hence, as the local wave grows, the phase speed decreases and a solitary wave is generated downstream of the disturbance when the local wave reaches a certain threshold.

The similarities become more conspicuous using a differential speed parameter defined as $\alpha' = \pm(U/c_{crit} - 1)$ with the plus sign and $c_{crit} = c_0$ for pure gravity waves and the minus sign and $c_{crit} = c_{\min}$ for gravity-capillary waves. Based on this definition, for both cases, the linear response becomes unbounded at the critical value $\alpha' = 0$ and no linear waves exist for $\alpha' > 0$. According to our results for gravity-capillary waves and the findings reported in Lee *et al.* (1989) for shallow water, the generation of solitary waves continues indefinitely for a range of subcritical and supercritical values of α' and the period of generation and the amplitude of the solitary waves increase with increasing α'. In the supercritical regime, there exists an upper bound for α' beyond which the phenomenon ceases to exist and only a local response is found. This upper bound becomes slightly larger when forcing is increased. In the subcritical regime, below a certain α', the amplitude of the solitary waves diminishes with time and the periodic generation seems to be a transient feature of the response. It was also found that the period of generation of solitary

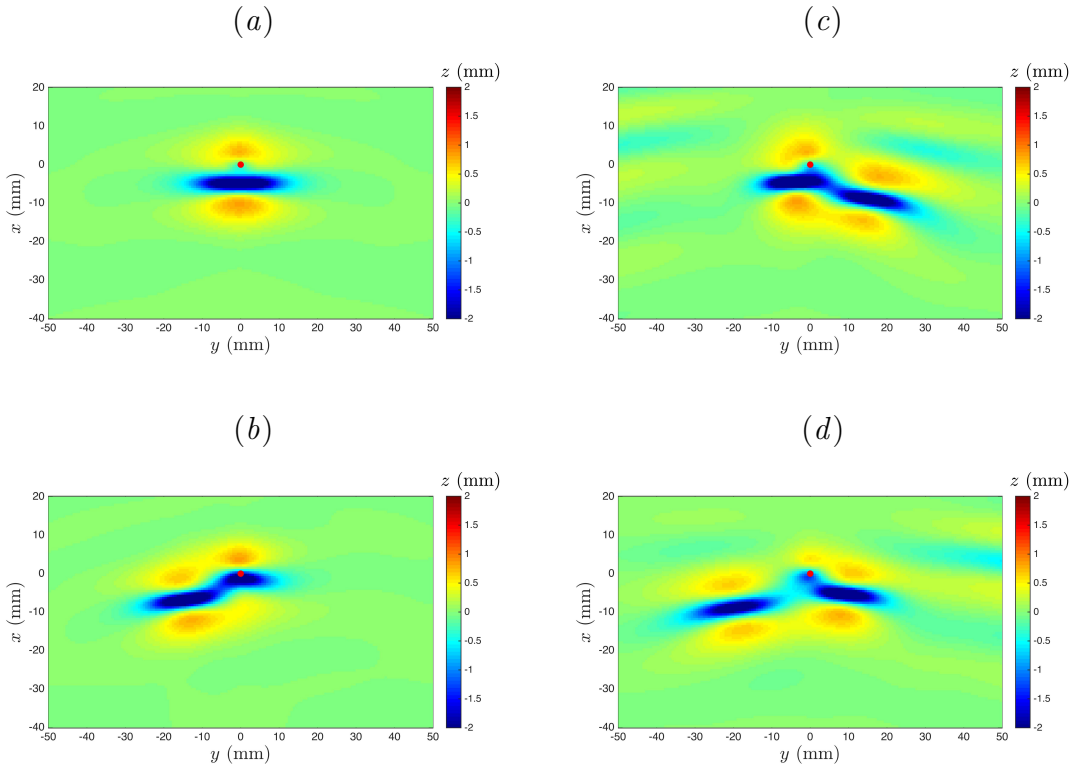

Figure 2.27: Surface elevation maps from simulations with $A = 0.3$, $\alpha = 0.908$ and $\tilde{\nu}_0 = 2.4\nu_0$. The pressure source is located at the origin and indicated by a white dot. (a) t=6 s. (b) t=7 s. (c) t=8.5 s. (d) t=9.5 s.

waves decreases with increasing forcing.

2.5.3 Asymmetric unsteady pattern

As discussed at the end of §2.5.1, a new response state featuring an unsteady asymmetric surface deformation pattern was discovered experimentally in the boundary region between state II and state III. In Cho *et al.* (2011), the model equation described in §2.4 was successful in, at least qualitatively, capturing all the response states observed in the experiments described in Diorio *et al.* (2011). In

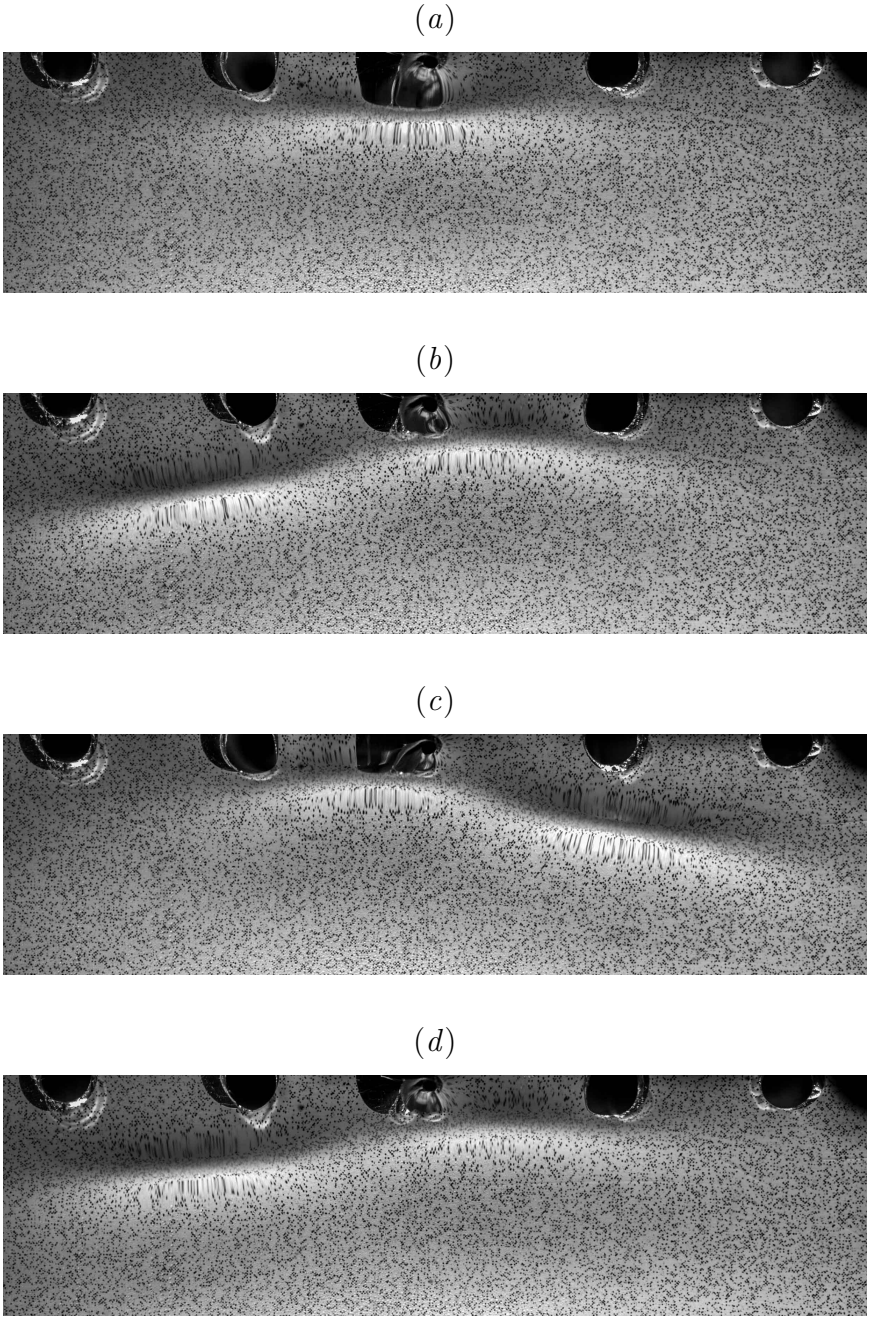

Figure 2.28: Refraction images in an experiment with $\epsilon = 0.24$ and $\alpha = 0.964$. The air-jet tube is located in the top middle. The field of view is about 9 cm wide. (a) $t = 0.0$, (b) $t = 3.7$ s, (c) t=7.1 s, (d) t=10.7 s.

the present work, the model is used to further explore the unsteady asymmetric behavior in the state II-III boundary region and the stability of state II. To this end, calculations were performed with $A = 0.30$, $\tilde{\nu} = 2.4\tilde{\nu}_0$ and a fairly wide range of α, $0.800 \leq \alpha \leq 1.040$. For each α, the evolution of the surface pattern is calculated for a period of 20 seconds.

As α is increased in successive numerical calculations, a sharp boundary is found between state I and II at $\alpha = 0.873$ where a sudden jump in the maximum depth of the depression was observed. In the speed range $0.873 \leq \alpha \leq 0.962$, a steady state II is formed after a few transient oscillations. Both of these results were reported in Cho *et al.* (2011). However, in the present calculations it was found that after some time the steady response in state II breaks down into an unsteady and asymmetric pattern that is very similar to the asymmetric wave pattern observed in the experiments for conditions in the state II-III boundary. This similarity can be seen by comparing the snapshots of the surface height field at late time in the computed wave pattern in state II, $\alpha = 0.908$, given in figure 2.27, to the series of refraction images showing the asymmetric deformation pattern in the state II-III region in the experiments, given in figure 2.28. In the numerical calculations, the surface pattern features alternate shedding of lumps from the right and left of the pressure distribution. This shedding behavior does not have a well defined period or left/right order especially at lower α values in the range. It was also found that the steady part of the response breaks down at larger times for higher α values (about 6 seconds for α=0.890 to about 10 seconds for α=0.962). For an α value slightly above 0.962, periodic shedding of lumps in a symmetric pattern is observed. The

shedding starts after about 2 seconds and continues for the length of the simulation. This boundary between asymmetric shedding and the symmetric shedding in state III is quite sharp in both the simulations and the experiments. Investigations into the possibility that the state II response in the experiments eventually breaks down into an asymmetric shedding pattern are left to future work using a longer tank.

2.6 Summary and conclusions

The unsteady wave pattern behind a surface disturbance moving with a constant speed (U) close to the minimum phase speed of gravity-capillary water waves ($c_{\min}$) was investigated by using a combination of experiments and numerical calculations. The experiments were performed in a long open-surface water tank in which the surface disturbance was created by downward air flow from the tip of a vertically oriented tube that was attached to a moving instrument carriage. In the numerical calculations, the model equation described in Cho *et al.* (2011) was used to extend the experimental results to times later than were possible in the experiments.

In previously published research, it was found that the water surface deformation pattern for $U \lesssim c_{\min}$ is determined by two external non-dimensional parameters: the strength of the forcing, $\epsilon = h_0/d$, where h_0 is the depth of the local depression under the air-jet tube when it is stationary and d is the tube's internal diameter, and the towing speed parameter $\alpha = U/c_{\min}$. Depending on the values of ϵ and α, the surface deformation pattern behind the source has three distinct response states: state I in which a steady axisymmetric dimple appears under the air jet

tube, state II in which a steady gravity-capillary lump appears behind the air-jet tube and state III in which an unsteady V-shaped pattern appears and includes the shedding of isolated depressions from the tips of the V. These depressions were found to decay rapidly as they propagated away from the source. In the previous experimental work, the steady response in states I and II as well as the unsteady response in the state I-II boundary region were studied in detail quantitatively using shadowgraph and laser-induced fluorescence techniques, but the response in state III was observed only qualitatively.

In the present experiments, state III and the boundary region between states II and III were studied in detail using a combination of cinematic refraction-based and shadowgraph-based techniques. It was found that the three-dimensional shape of the localized depressions in state III are similar to the shapes of steady, forced lumps of state II and the freely propagating lumps of inviscid potential theory. Measurements of the speed of these depressions during their decay revealed that they follow the speed-amplitude relation of steady lumps from inviscid potential theory. Based on these two findings, the isolated depressions appear to be freely propagating gravity-capillary lumps. The exponential decay rate of these lumps was found to be about 1.11 s^{-1}, indicating substantial decay over time scales on the order of one second, a time over which a typical lump travels only about 20 cm. Numerical simulations of the model equation suggest that the periodic behavior in state III is not a transient phenomenon and continues indefinitely. It was found in the experiments that the period of shedding ($\overline{T}$) in state III decreases with increasing towing speed and approaches a value of about $1.5T^*$ as α approaches unity for all

values of the forcing parameter, ϵ. The time scale T^* is the period, as measured in the reference frame of the source, of a linear wave whose group velocity is equal to $c_{\min}$ and whose wavelength is longer than the wavelength of the wave with phase speed equal to $c_{\min}$. Numerical simulations of the model equation were used to explore the surface response pattern at times later than could be achieved in the experiments, due to the limited tank length. It was found that in the simulations, once initiated, the state III response continues unaltered over the longest numerical runs attempted, 100 s.

In the experiments, it was found that there is a boundary region between state II and state III, in which the surface response is unsteady and features asymmetric irregular shedding of lumps from the two sides of the deformation pattern. A similar response state was found in the numerical simulations. In fact, in the simulations, the response for all state II conditions eventually breaks down into an asymmetric shedding pattern, similar to that found in the state II-III boundary region in the experiments. The possibility that the state II response breaks down after a sufficiently long time in the experiments is left for future investigations.

It is noted that the above-described behavior bears a strong similarity to the upstream periodic shedding of two-dimensional solitary gravity waves from a source moving at trans-critical speeds relative to the maximum speed of linear gravity waves in shallow water. In this analogy, the solitary wave shedding processes in the two systems are similar in many respects if one views the process in terms of the source strength and the differential speed parameter, $\alpha' = \pm(U/c_{crit} - 1)$, where U is the towing speed and c_{crit} is the critical speed, with the minus sign and $c_{crit} = c_{\min}$ for

gravity-capillary waves and the plus sign and $c_{crit} = \sqrt{gH}$ for shallow water gravity waves, where H is the water depth.

Chapter 3: Experiments on viscous dissipation of free lumps

3.1 Introduction

As discussed in chapter 1, most theoretical and numerical studies of solitary waves assume the flow to be inviscid and a complete theory for the effects of viscous dissipation on steep solitary waves is still lacking. Longuet-Higgins & Zhang (1997) performed experiments on viscous dissipation of two-dimensional gravity-capillary solitary wave in a narrow water flume. They generated two-dimensional solitary waves by blowing air vertically onto the water surface through a two-dimensional slit and resonantly exciting the water surface while the water was running in the flume at a speed near the minimum phase speed. They inserted a small amount of chalk powder to visualize the free surface shape. The observed profiles matched well with the theoretical profiles calculated by Longuet-Higgins (1989), see figure 1.5, especially at speeds close to $c_{\min}$. At lower speeds, some unsteadiness was observed, probably owing to lateral instabilities and the profiles deviated from the theoretical ones. The behavior of a solitary wave under the action of viscosity was also investigated by removing the forcing and observing the evolution of the free surface shape. As expected, the wave amplitude diminished with time while its phase speed increased. The rate of decay of the amplitude was much larger when

the wave was steep. This experimental study was accompanied by a theoretical work by Longuet-Higgins (1997). The main idea of the paper is that "the nonlinear wave maintains its steady form approximately while decaying under the action of viscosity" i.e. weak dissipation. In this regard, the total rate of work done against surface stresses must be equal to the total rate of dissipation of energy in the fluid. He derived a general equation to calculate the rate of decay of solitary waves. He found that, in low-amplitude limit, the decay rate of wavepacket solitary waves is twice the value for a uniform train of infinitesimal waves with wavenumber equal to the carrier wavenumber of the solitary wavepacket. This is attributed to the spreading of the wave envelope as the amplitude decreases. For steep solitary waves, it was found that the local decay rate depends on the steepness of the wave and is much larger than that of wavepacket solitary waves. Calvo & Akylas (2002) examined the two-dimensional stability of steep solitary waves and suggested that the strong forcing is responsible for the unsteadiness observed in the experiments by Longuet-Higgins & Zhang (1997).

In this chapter, the temporal evolution of freely propagating gravity-capillary lumps under the effect of viscous damping is investigated to provide a basis for theoretical modeling of the nonlinear viscous damping of forced and free lumps. A steady forced lump in state II is first generated using a pressure source moving at a constant speed below $c_{\min}$. The forcing is then removed abruptly and the change in shape, depth and speed of the lump is measured as it decays under the effects of viscous dissipation.

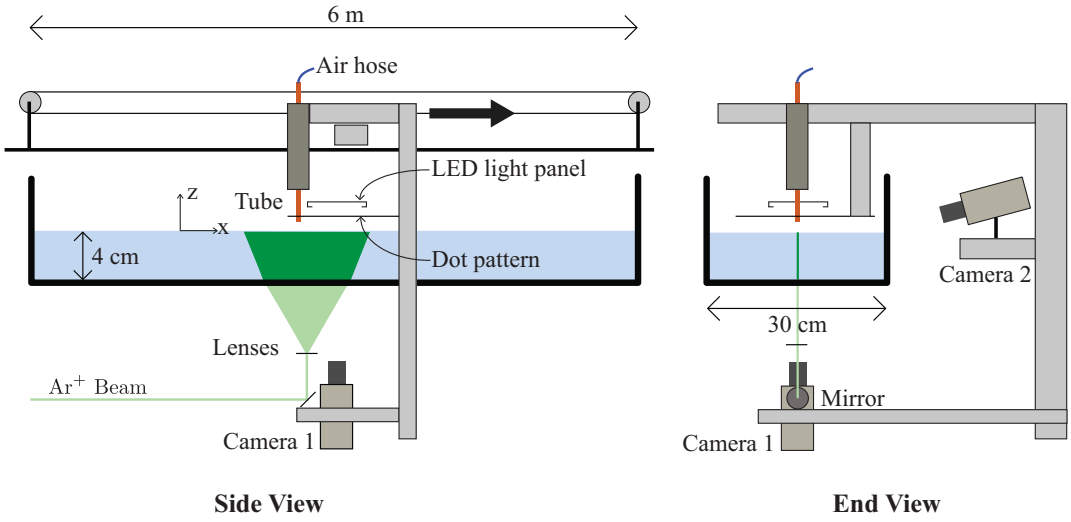

Figure 3.1: Schematic of the experimental set-up. The air-jet tube and the laser light sheet are positioned in the middle of the tank width.

3.2 Experimental details

The experimental set-up consists of the water tank and instrument carriage system described in the previous chapter (see §2.2). The main difference in the set-up is that the air-jet and the laser light sheet are now positioned at the center of the tank width. The water surface deformation pattern is measured using the LIF and the refraction techniques (see §2.3).

Before each experiment run, clean water is pumped from the source tank to the experiment tank and is drained through the skimmer pipes for about ten minutes. A water sample is taken at this time for the surface pressure isoterm measurement. The air tank is filled with compressed air at 30 psi. The airflow in the tube is

adjusted using the needle valve and is let open for about a minute before the run. The carriage is then triggered to accelerate and reach the desired steady speed. The carriage moves about 25.4 cm before reaching the final speed. The carriage speed for the experiments presented in this chapter is in the range of 20.5 cm/s to 22 cm/s corresponding to speed parameters α in the range of 0.886 to 0.951. A forcing corresponding to $\epsilon = 0.35$ was used in all experiments. The surface response for these parameters while the forcing is on is a state II steady lump as described in Diorio *et al.* (2011) and shown in the state diagram of figure 2.14. The lower towing speeds in the range are close to the boundary between state I and state II and the wave pattern is a very steep depression located close to the pressure source. As the towing speed is increased and approaches the boundary between state II and state III, the pattern becomes asymmetric in the streamwise direction and the main depression moves downstream of the pressure source. The maximum depth of the steady lump decreases with increasing towing speed but it becomes more elongated in the cross-stream direction.

A state II lump response is quickly formed after the steady towing speed is reached. After approximately 6 seconds into the steady part of the carriage motion, the air-jet is suddenly turned off by manually shutting off the control knob on the airflow meter. The exact time of the shut-off can be found within 4 frames (1/150 s) from the high speed movies. In most runs, the carriage continues its constant speed motion after the shut-off for about 5 seconds so the cameras can follow the change in shape and speed of the water surface response. In some cases, the carriage is programmed to decelerate right after the air-jet is turned off and then continue its

motion at a constant speed 3 cm/s slower than the speed before the shut-off. The purpose of this change in carriage speed is to make the wave pattern that is originally under the air-jet tube visible to the camera. A sequence of images starting from before the shut-off until about 4 seconds after the shut-off are processed using the LIF and refraction methods to find the surface profile in the middle plane of the wave pattern and the 3-D shape of the free surface upstream of the disturbance.

3.3 Results and discussion

LIF measurements of water surface profiles at the center-plane of the air-jet tube were carried out for four towing speed parameters $\alpha = U/c_{\min}$ of 0.886, 0.908, 0.930 and 0.951 where U is the carriage speed and $c_{\min} = 23.13$ cm/s is the minimum phase speed of linear gravity-capillary waves. Sequences of processed profiles for different towing speeds are shown in figure 3.2. These profiles are plotted in a reference frame moving with the tube. Each profile is shifted vertically from the previous one by 0.1 mm and the time interval between consecutive profiles is 1/150 s. In this coordinate system, the air-jet tube is located at $x = 0$ and the carriage is moving in the positive x direction (from left to right). The first profile in each sequence shows the steady lump profile just before the air-jet is turned off. After the forcing is removed, the main depression starts to decay. As the lump becomes shallower, it speeds up and moves upstream of the air-jet tube. This depression remains isolated for a relatively long time, at least in the stream-wise direction, and resembles the profile of a gravity-capillary lump. In all cases some small ripples are

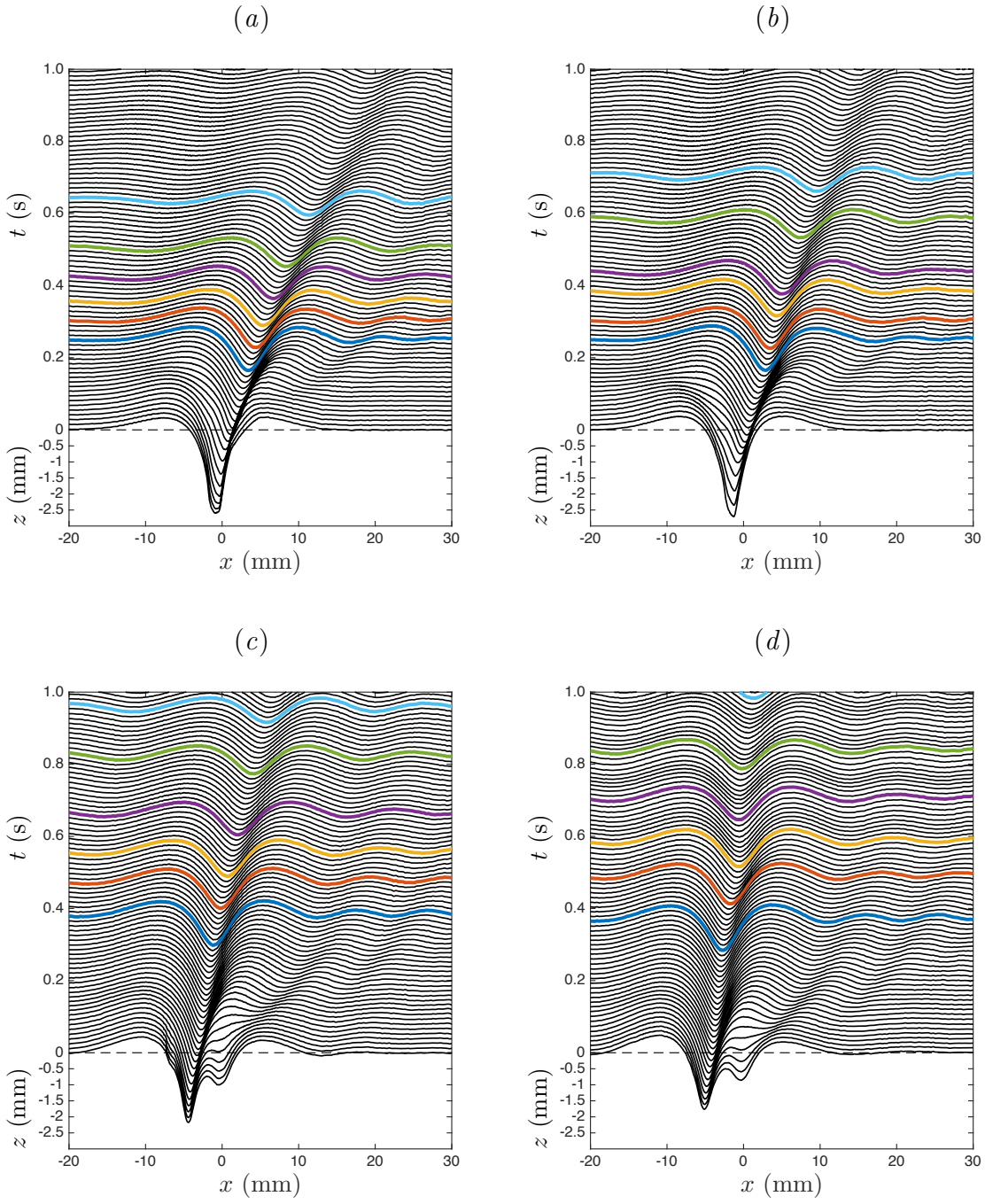

Figure 3.2: Free surface profiles in the center-plane of the tube. Each profile is shifted vertically from the previous one by 0.1 mm and the time interval between consecutive profiles is 1/150 s. (a) $\alpha = 0.886$. (b) $\alpha = 0.908$. (c) $\alpha = 0.930$. (d) $\alpha = 0.951$. The profiles with the same color have the same maximum depth.

generated immediately after the forcing is removed and propagate in front of the main depression.

The wave profiles at maximum depths of $h = 1$, 0.9, 0.8, 0.7, 0.6 and 0.5 mm are color-coded in figure 3.2 for comparison between different cases. It is observed that at lower towing speeds, for which the steady lump under the forcing has a larger depth, the lump decays faster when the forcing is removed compared to higher towing speeds. To further illustrate this point, the maximum depth of the main depression was tracked in time and the results are shown in figure 3.3. The instant the forcing is removed is defined as $t = 0$. In this figure the maximum depth is plotted in logarithmic scale and the local slope of each curve is equal to the exponential decay rate of the lump at that instant. It is observed that the free-surface response decays at a very high rate immediately after the forcing is removed but reaches a constant decay rate at about $t = 0.3$ s. This is in agreement with the results of Longuet-Higgins (1997) for two-dimensional gravity-capillary solitary waves where solitary waves with larger steepness have a higher rate of decay.

The almost constant exponential decay rate at later times was computed by fitting a function in the form of $h(t) = h_0 \exp(-\sigma t)$ to the data between $t = 0.3$ s and $t = 1.0$ s for each towing speed. The fitted functions are plotted as dashed lines in figure 3.3 and the computed decay rates are plotted against α in figure 3.4. The data shows that the decay rate of a lump depends on the condition in which it was generated. For example, if we consider the profiles with the same color in figure 3.2, although they have a very similar profiles in the stream-wise direction, the ones that were generated at a lower towing speed decay faster. In general the

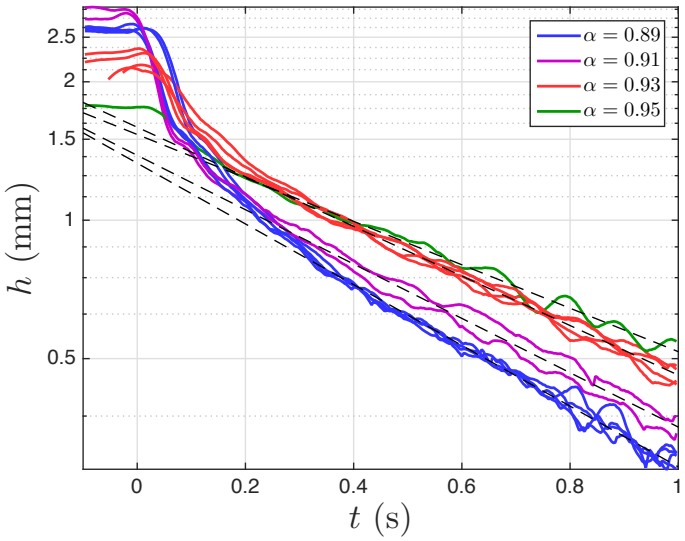

Figure 3.3: Maximum depth of depressions versus time for different towing speeds. The forcing is removed at $t = 0$. The dashed lines are exponential fits for $0.3 \leq t \leq 1$ s.

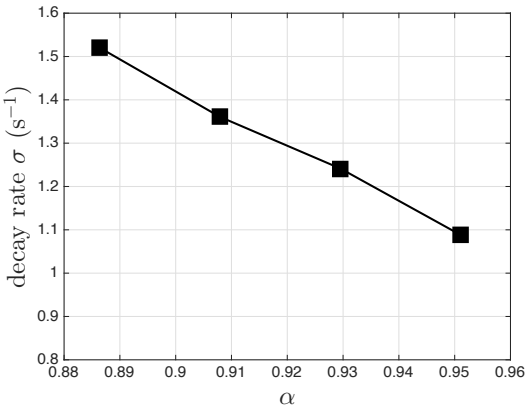

Figure 3.4: Exponential decay rate of the lumps versus towing speed parameter.

rate of decay is relatively high. For example for a lump with initial depth of about 2.5 mm, the decay rate is about $\sigma = 1.52$ s^{-1} which means that it loses about 63 percent of its initial depth in less than 0.66 seconds. The high decay rate of lumps indicates that observation of gravity-capillary lumps generated in normal conditions (for example in the ocean or a wind tank) might be difficult. For comparison, as reported in §2.5.2, the measured decay rate of unsteady lumps of state III is about $\sigma = 1.11$ s^{-1} which is close to the decay rate of the free lumps that are generated at $\alpha = 0.951$, which is almost at the boundary of states II and III for the forcing used (figure 2.14).

The LIF measurement only yields the streamwise profiles of the lumps along their centerplanes. The observation that the decay behavior of lumps are different even when they have the same stream-wise profiles, points to the importance of the cross-stream variations. Quantitative measurement of the three-dimensional surface shape upstream of the pressure source during the lump decay was carried out using

the refractive-based method explained in §2.3. Experiments were performed for towing speeds of $\alpha = 0.886$ and $\alpha = 0.930$. The measurement region is about 10 cm in the cross-stream direction and 6 cm in the stream-wise direction and it covers the region upstream of the air-jet tube. The tube is visible in the camera images and its position can be determined accurately. Images are taken at 600 frames per second. The spatial resolution of the measurement is about 0.6 mm in both directions. Due to the limitations of the method (mainly ray crossing at places with high surface curvature) only waves with amplitudes smaller than about 1 mm can be measured reliably. Comparison of the results of this method with the LIF technique shows an error of less than 5% for surface elevation.

Contours of the surface elevation for two runs are shown in figures 3.5 and 3.6. The air-jet tube center is located at the origin of the coordinate system. The carriage is moving in the positive x direction (from left to right) and the free surface is measured in a reference frame moving with the source. In these experiments the carriage continues its motion at the same speed before and after the air-jet is turned off. At $t = 0$, the forced lump is behind the tube and is not visible in the field of view of the measurement. After the forcing is removed, a ring wave pattern is generated with small amplitude short waves in the forefront. The main depression is too steep at this stage (it is also blocked by the tube) and the measurement method fails to capture it, but the smaller amplitude ring waves are observed upstream of the tube. As the main depression decays, it moves upstream of the tube and becomes visible in the field of view and is clearly seen in the snapshots after $t = 0.4$ s as a localized depression. By this time, the depression is much more extended in the

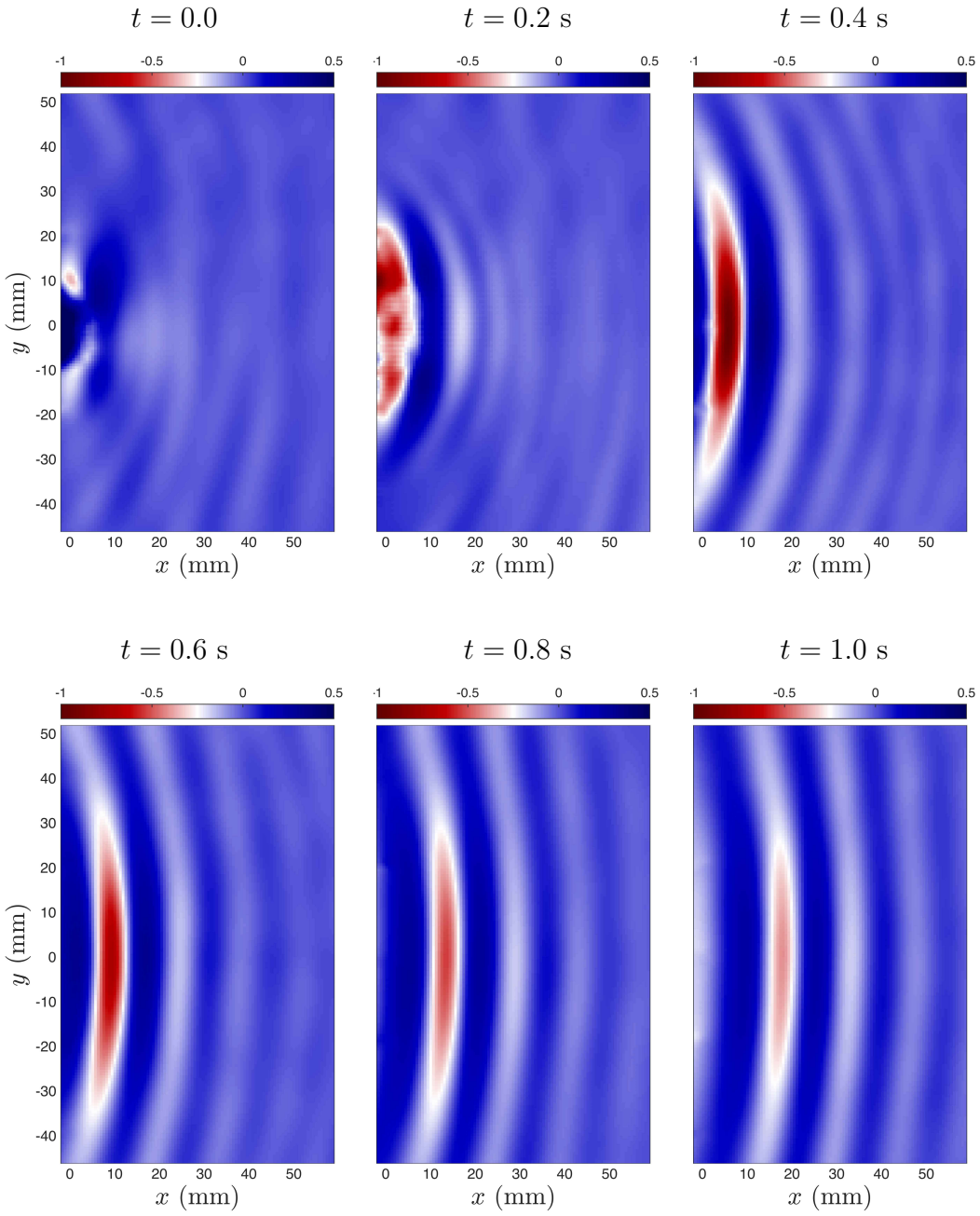

Figure 3.5: Snapshots of the surface elevation (in mm) for $\alpha = 0.886$ and $0.0 \leq t \leq 1.0$ s.

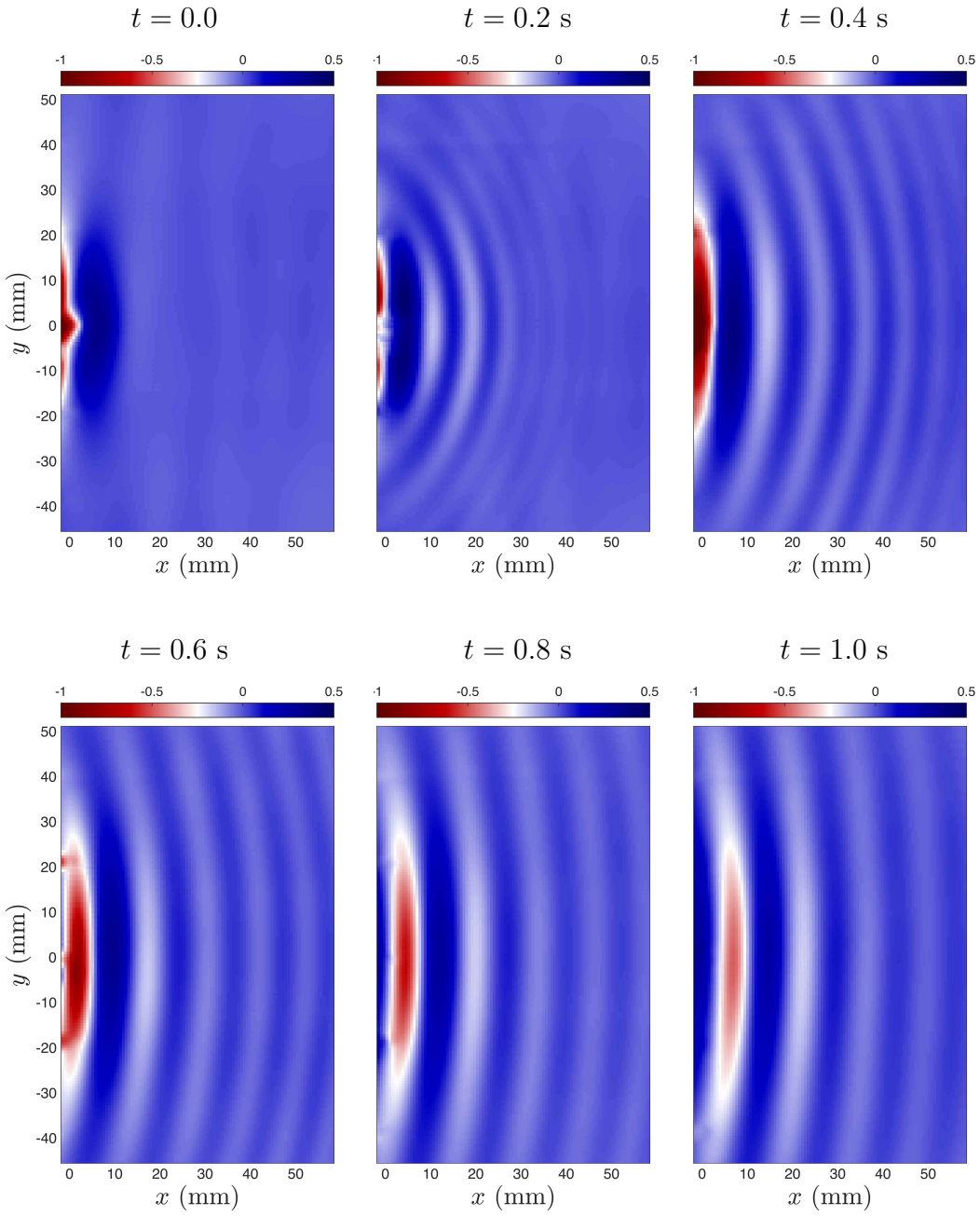

Figure 3.6: Snapshots of the surface elevation (in mm) for $\alpha = 0.930$ and $0.0 \leq t \leq 1.0$ s.

cross-stream direction than the forced gravity-capillary lumps in state II measured by Diorio *et al.* (2011).

At later times ($0.6 \leq t \leq 1.0$ s) the wave pattern is a combination of small amplitude ring waves and a decaying localized depression that keeps expanding in the cross-stream direction. Longuet-Higgins (1997) attributed the higher decay rate of 2-dimensional gravity capillary solitary waves compared to linear sinusoidal waves to the spreading of the wave envelope as the wave amplitude decreases. In the small amplitude limit, where the solitary waves are governed by the NLS equation (Akylas, 1993), the decay rate is twice the value for an infinite train of linear sinusoidal waves. Similarly, we can expect an even higher decay rate for three-dimensional lumps due to the spreading in both directions. Cho *et al.* (2011) used a value of $\tilde{\nu} = 2.4\tilde{\nu}_0$ for the viscous dissipation parameter in their model equation (see §2.4, equation 2.7) where $\tilde{\nu}_0$ is the theoretical value for linear waves.

Eventually as the amplitude becomes too small, the localized structure of the lump is disrupted and the wave pattern resembles two-dimensional sinusoidal waves with a wavelength of about 1.5 to 1.7 cm (the same order of magnitude as $\lambda_{\min}$). This can be seen in the wave pattern for $1.2 \leq t \leq 2.2$ seconds for two runs with $\alpha = 0.886$ and $\alpha = 0.930$ are shown in figures 3.7 and 3.8, respectively.

It was observed from the LIF results in the center-plane of the tube that depressions with similar amplitudes and profiles can have different decay properties. From the snapshots of the three-dimensional shape of the wave pattern, it seems that the lumps that were generated at a lower towing speed (higher initial amplitude) are more extended in the cross-stream direction. In order to obtain a better

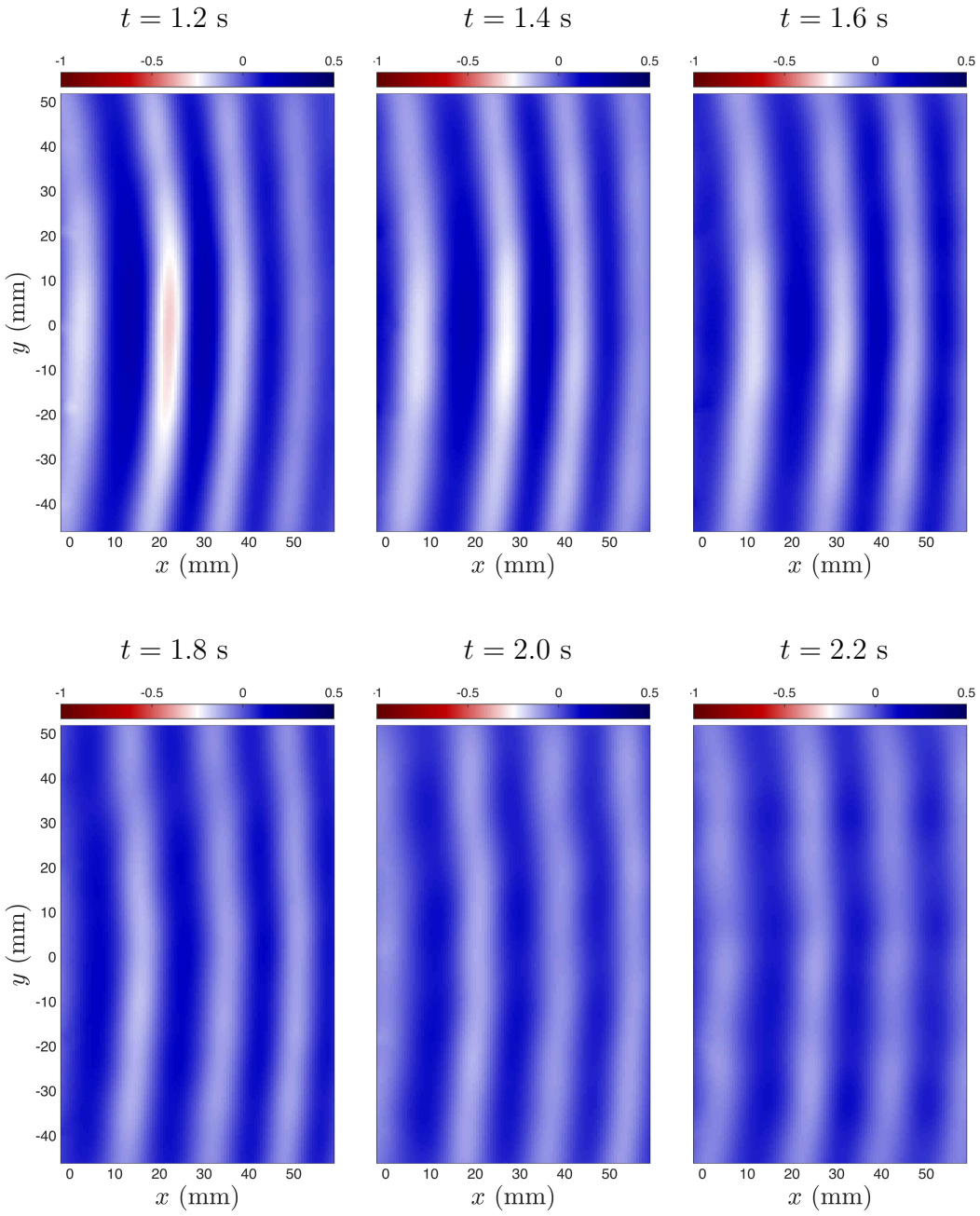

Figure 3.7: Snapshots of the surface elevation (in mm) for $\alpha = 0.886$ and $1.2 \leq t \leq 2.2$ s.

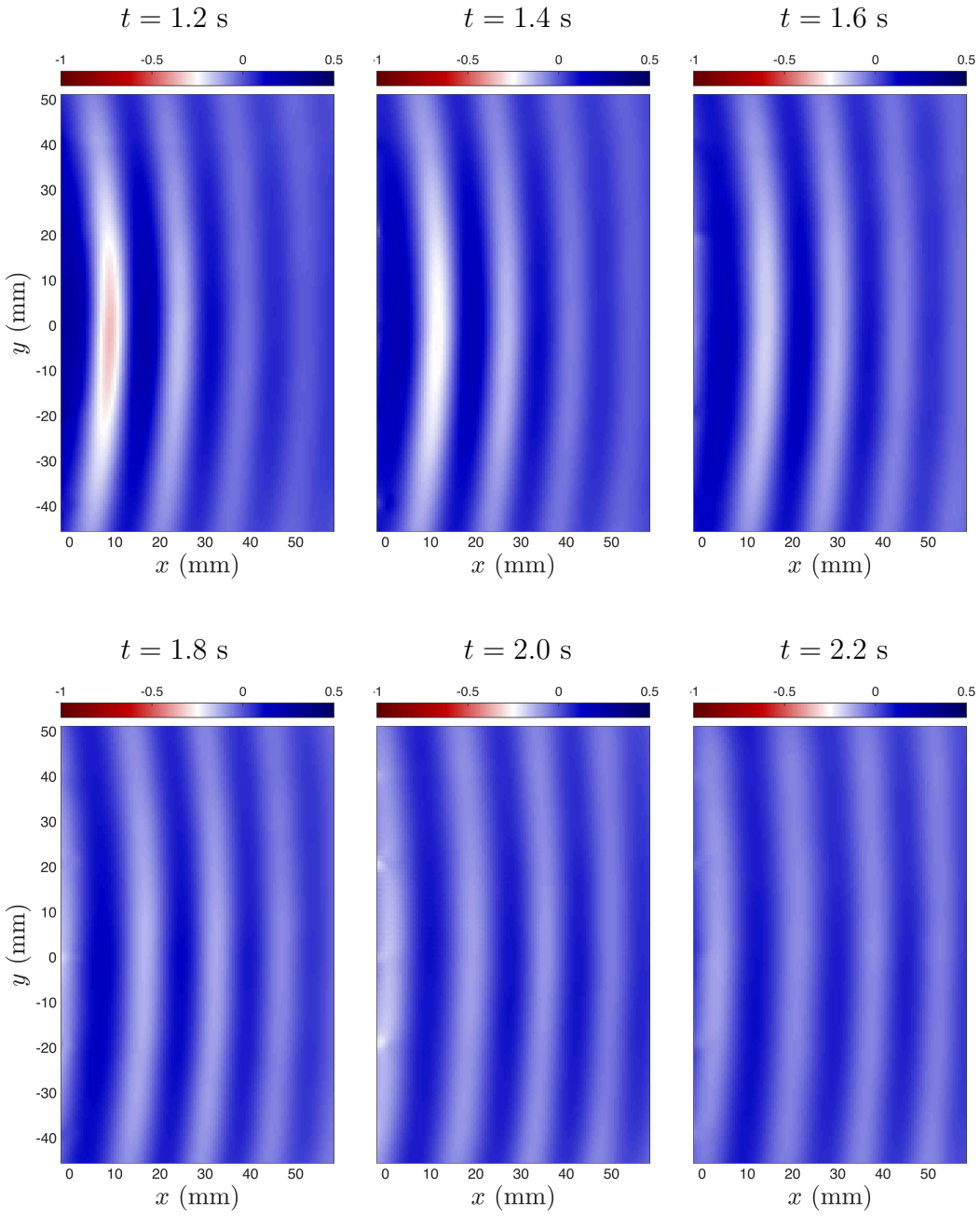

Figure 3.8: Snapshots of the surface elevation (in mm) for $\alpha = 0.930$ and $1.2 \leq t \leq 2.2$ s.

measurement of the shape of the main depression, the carriage program was changed and the carriage was set to decelerate to a lower steady speed right after the air-jet was shut off. After the air-jet is turned off the wave pattern is not affected by the motion of the carriage anymore and the lump is translated to the middle of the field of view of the camera.

Several runs with $\alpha = 0.886$ and $\alpha = 0.930$ were carried out with the modified carriage input. Results for two runs are shown in figures 3.9 and 3.10. This time, instead of plotting the surface elevation pattern at a certain instant after the shut-off, the snapshots of the wave shape are plotted when the depressions of a certain amplitude are observed. In these plots, the boundaries of each lump are also plotted as black lines. These boundaries define an enclosed region with an elevation of $z < -h/2$ where h is the maximum depth of the lump at that instant. From these plots, it is clear that the lumps that were generated at a slower towing speed are more extended (have a larger area) than the lumps of the same amplitude in the higher towing speed case.

The width of the free lumps can be measured at each amplitude using the boundaries defined at $z = -h/2$. For each towing speed parameter, four experimental runs are performed and the results are averaged for each amplitude. Figure 3.11 shows the variation of the width of the lumps versus their maximum deoth for two speed parameters.

One of the well-known features of solitary waves is the one-to-one relation between their speed and amplitude. Resonantly forced lumps of state II move at the same speed as the pressure forcing and a monotonically decreasing relation

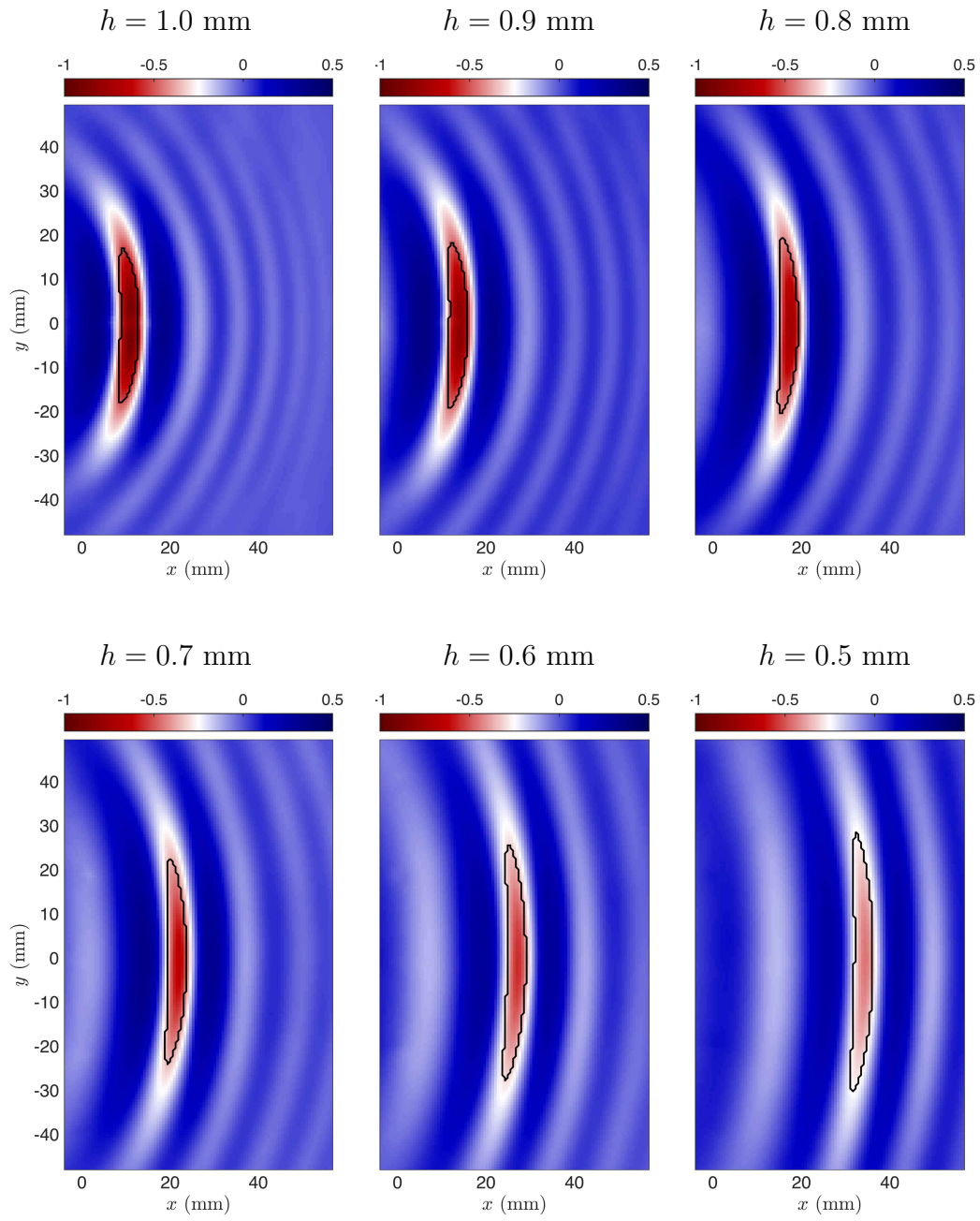

Figure 3.9: Snapshots of the surface elevation (in mm) for $\alpha = 0.886$ at different lump amplitudes, h. The black lines are the boundary of the region with $z < -h/2$.

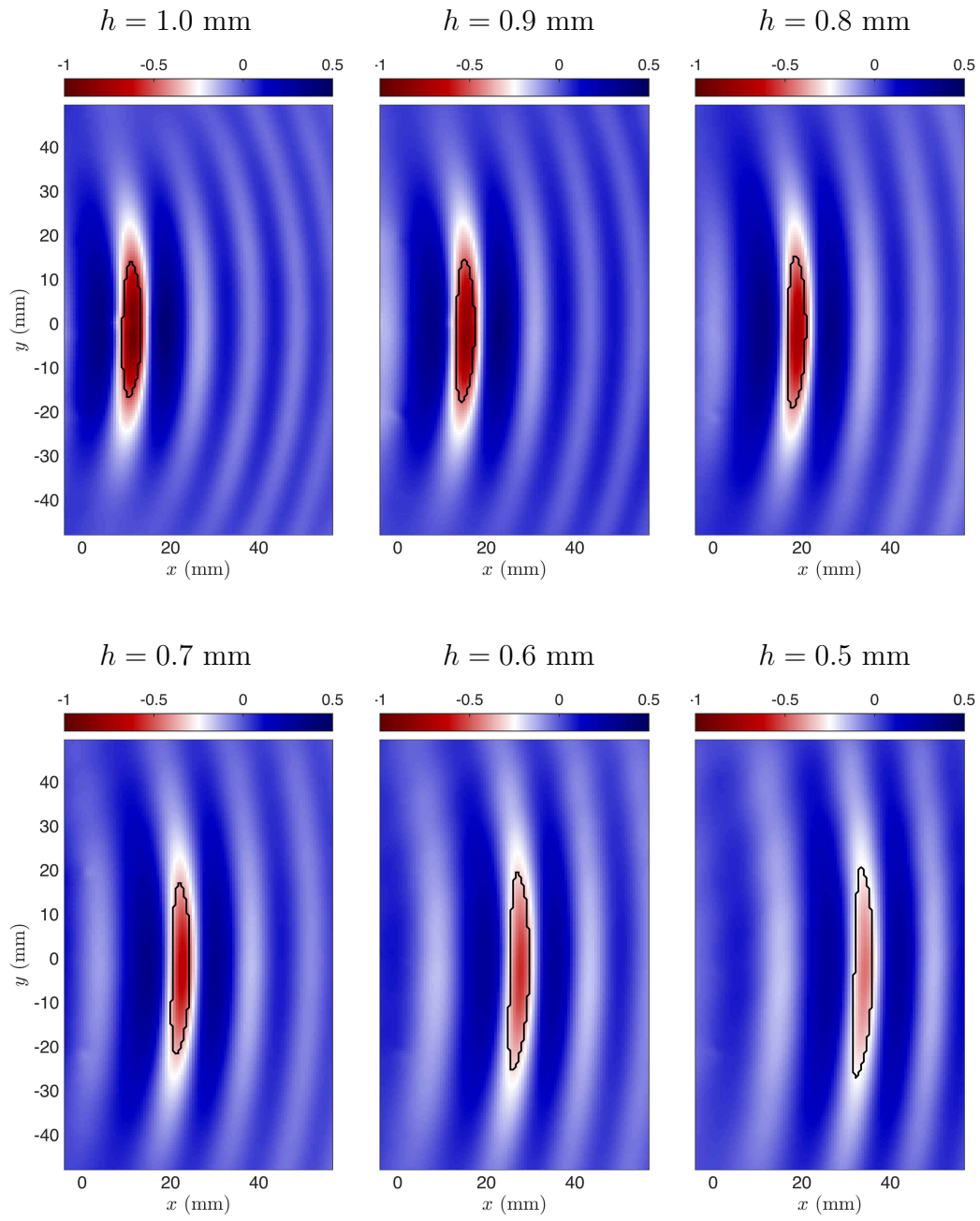

Figure 3.10: Snapshots of the surface elevation (in mm) for $\alpha = 0.930$ at different lump amplitudes, h. The black lines are the boundary of the region with $z < -h/2$.

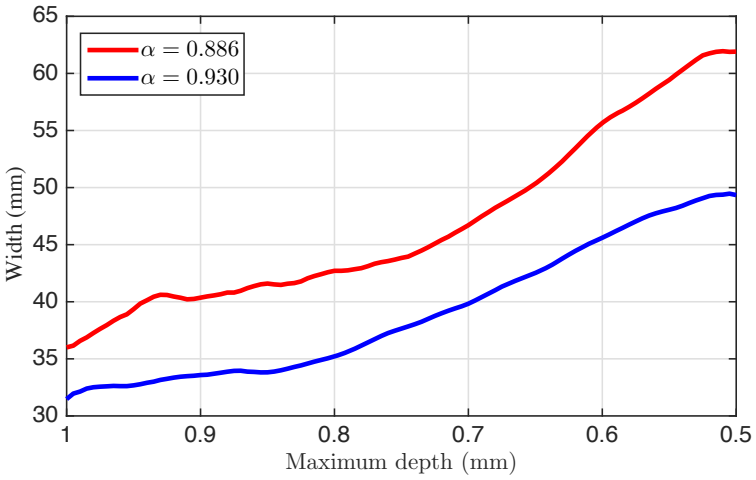

Figure 3.11: Width versus amplitude for lumps generated at speed parameters $\alpha = 0.886$ and $\alpha = 0.930$. Each curve is an average of four experimental runs. Note that the x-axis is decreasing.

between their maximum depth and the towing speed was found in the experiments of Diorio *et al.* (2011). A similar relation was found in the inviscid potential flow calculations of Părău *et al.* (2007) for freely propagating lumps.

The unforced free lumps decaying under the effects of viscosity are unsteady. It is clear from the experimental results presented in this chapter that these lumps move forward when the forcing is removed indicating that the speed of a free lump increases as the amplitude decreases. In order to measure the speed of these free lumps, the position of the maximum depth for a lump was tracked using the LIF measurements. Velocity results obtained from the position signal is in general noisy. Especially at higher towing speeds the difference between the final speed of a free lump and the carriage speed is small and the results from tracking the maximum

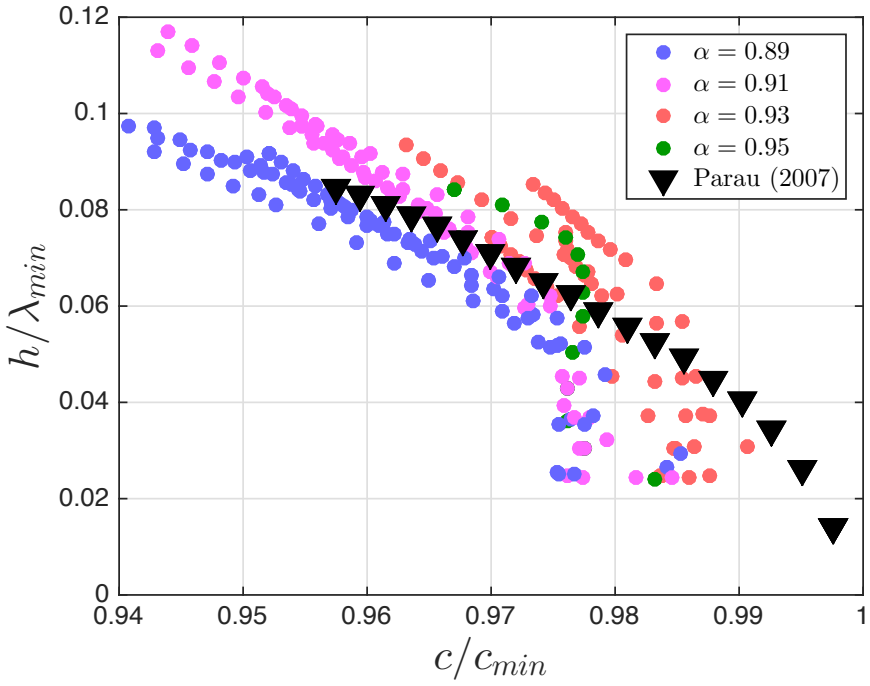

Figure 3.12: Maximum depth of free lumps versus their measured speed in the reference from of the lab. $\lambda_{\min}$ and $c_{\min}$ are used as length and velocity scales. Each dot represent the average speed of a lump during its decay over a small time interval.

depth are sensitive to the vibrations present in the system. Nonetheless, velocity measurement was performed on fourteen free lumps from separate runs with different generation towing speeds. The results are shown in figure 3.12. In this plot each dot is the average velocity of a lump over a time interval of 0.25 s versus its average maximum depth during the same time interval. The speed versus height relation for a steady free lump from inviscid potential flow calculations of Părău *et al.* (2007) is also plotted as downward triangles for comparison. It is observed that, although the free decaying lumps measured in the experiments are not steady, they follow the theoretical curve very closely. This is especially true for the lumps generated at lower towing speeds. The experimental results deviate from the theoretical curve when the lump amplitude becomes smaller than about 0.5 mm and the localized structure of the lump is destroyed.

The model equation described in §2.4 was used to test the validity of the viscous dissipation term in the equation and compare the decay properties with the experimental results. The computational domain was $-75.4 < \xi < 75.4$ and $-31.4 < y < 31.4$ with 1024 and 256 grid points in ξ and y directions, respectively. A forcing parameter of $A = 0.30$ and a viscous damping of $\tilde{\nu} = 2.4\tilde{\nu}_0$ were used to generate the state II response for $\alpha = 0.930$. The simulation was performed for $0 \leq t \leq 5$ s with this forcing and a steady state II response was obtained. The forcing term was then set to zero and the unsteady response was calculated for $5 < t < 10$ s. Contours of the free surface elevation after the forcing is removed are shown in figure 3.13. The model equation generally overpredicts the lump amplitude (see Cho *et al.*, 2011) but the surface response is qualitatively similar to the experimental results of

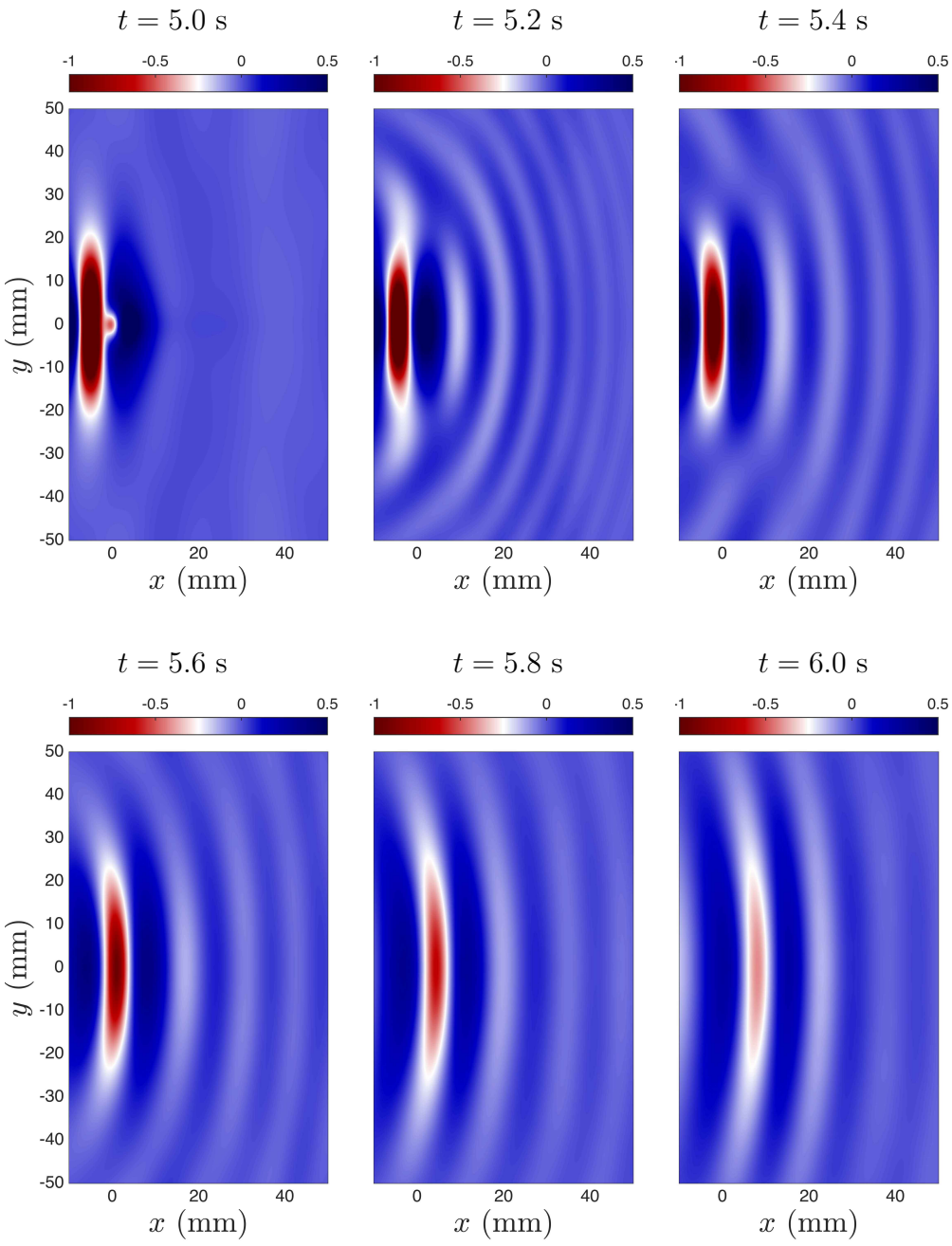

Figure 3.13: Simulation results of the model equation. Snapshots of the surface elevation (in mm) for $\alpha = 0.930$ and $5.0 \leq t \leq 6.0$ s. The forcing term is $A = 0.30$ for $t < 5.0$ s and is set to zero at $t = 5.0$ s.

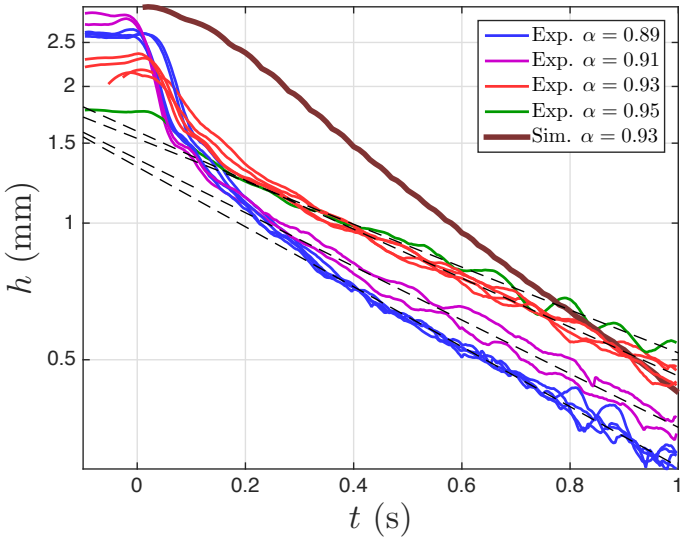

Figure 3.14: Maximum depth of depressions versus time for different towing speeds. The forcing is removed at $t = 0$. The dashed lines are exponential fits for $0.3 \leq t \leq 1$ s.

figure 3.6.

The decay rate of the lump shown in figure 3.13 is compared to the experimental LIF results in figure 3.14. It clearly shows the viscous damping in the model equation cannot capture the correct behavior especially at large steepness and a nonlinear model that depends on the wave steepness should be considered.

3.4 Summary and conclusions

In this chapter, the evolution of a free lump under the action of viscosity was explored experimentally. A forced lump in state II was first generated. The forcing was then removed suddenly and the lump then propagated freely. The change

in shape and speed of the free lump was measured using the LIF and refraction techniques. The decay rate of these free lumps was found to be relatively high and depend on the steepness just after the forcing was removed but a constant exponential decay rate was found about 0.3 second after the forcing was turned off. This constant decay rate was found to depend on the initial shape of the lump, i.e. the towing speed of the forcing. At low towing speeds (i.e. larger initial depth), the observed decay rate is larger. Full-field measurement of the free surface shape suggests that the spreading of the lump in cross-stream direction is responsible for the difference in decay rates. Measurement of the speed of the free lumps as they decay shows that they follow the speed-amplitude relation for freely propagating lumps of potential theory very closely until the amplitude becomes too small and the localized structure of the lump is lost. Comparison of the experimental results with the simulation results of the numerical model reveals that the linear viscous damping used in the model equation does not capture the correct behavior especially at large steepness and a nonlinear model is required.

Chapter 4: Oblique interaction of lumps generated by two pressure sources moving at trans-critical speeds

4.1 Introduction

As discussed in chapter 2, a surface pressure source moving at a speed close to $c_{\min}$ periodically generates gravity-capillary lumps (state III). These lumps are generated in pairs from the tips of a V-shaped wave pattern. In the reference frame of the laboratory, the trajectory path of a lump makes an angle of about 15 degrees with the direction of the source motion. Now, consider two pressure sources moving in parallel at a speed that produces a state III response for each tube. It is possible to generate nearly identical lumps from the two sources and have them collide in the middle of the sources. In this chapter, the dynamics of the wave pattern produced by two disturbances moving at speed close to $c_{\min}$ is investigated experimentally.

An interesting feature of KdV solitary waves is that they can interact with other solitary waves and remain unchanged after the interaction, except for a phase shift (Solitary waves that possess this characteristic are called solitons, see Scott, 2005). For theory and experimental measurements of collision of shallow water solitary waves see Craig *et al.* (2006) and Chen & Yeh (2014). The collision of

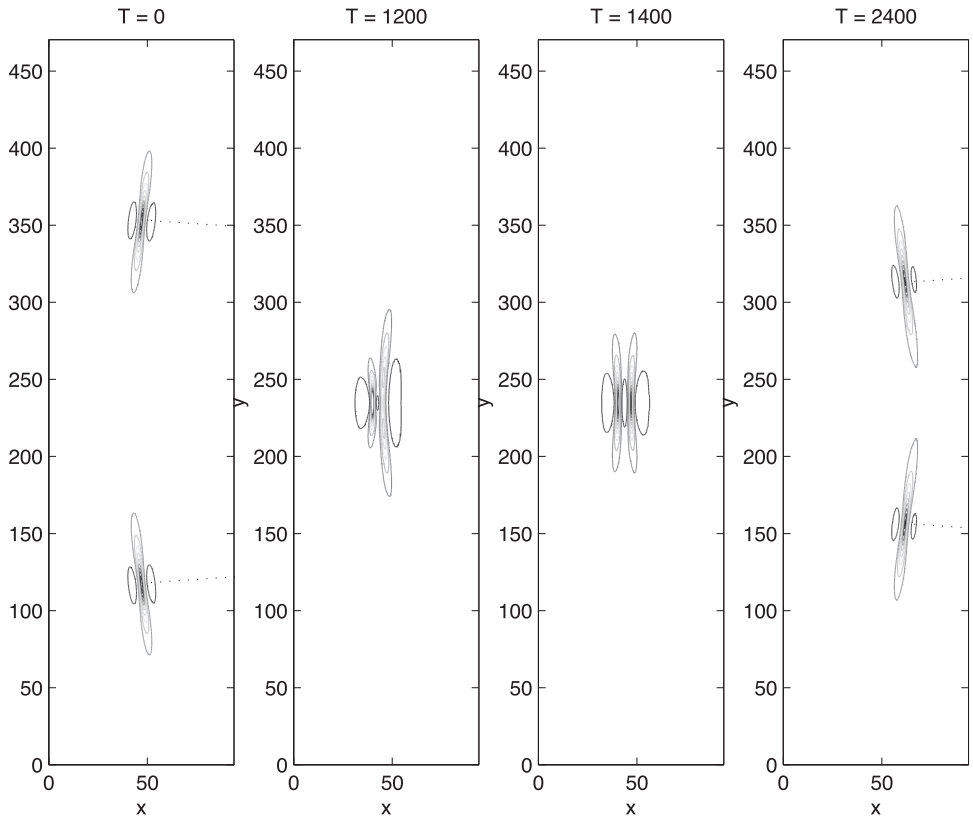

Figure 4.1: The collision of two lumps in the surface-tension-dominated regime based on the generalized Benny-Luke equation from Berger & Milewski (2000).

gravity-capillary solitary waves has been considered numerically by several authors. Milewski *et al.* (2010) performed simulations based on Euler equation for head-on collisions and overtaking collisions of two-dimensional solitary waves. They found that head-on collisions were almost elastic with little radiation but for overtaking collisions the smaller wave can break up and transfer some energy to the larger wave. The dynamics of three-dimensional lumps during collision was studied by Akers & Milewski (2010) and Wang & Milewski (2012) using model equations based on a truncation of the Euler equation. They reported similar results to the two-dimensional case mentioned above for head-on and overtaking collisions.

Perhaps the most relevant previous work on lump collisions to the experimental results of this chapter is the study by Berger & Milewski (2000). They reported "oblique" collision of two lump solutions of the generalized Benny-Luke equation for the strong-surface-tension regime ($Bo > 1/3$) and found a soliton like interaction between with the lumps appearing intact after the collision (see figure 4.1).

In this chapter, a brief overview of the experimental setup and measurement techniques is given first. This is followed by the experimental results and discussion of the measurements of the wave pattern generated by two pressure sources.

4.2 Experimental details

The experiments are done in the tank and carriage setup explained in §2.2. For the experiments presented in this chapter an additional air-jet tube is added to the setup.Two pressure disturbances are made on the water surface by blowing

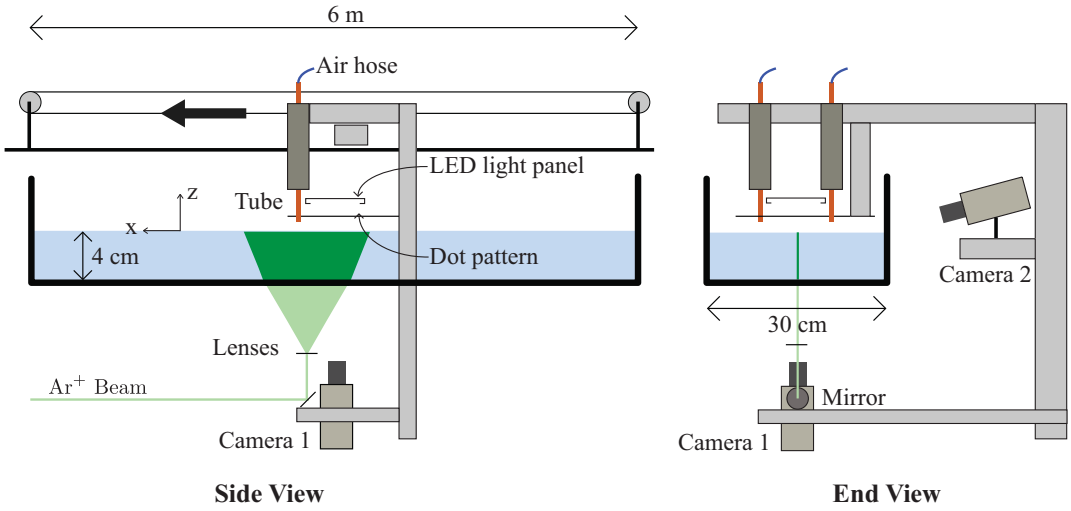

Figure 4.2: Schematic of the experimental set-up. Two air-jet tubes are mounted on the carriage and the distance between them is adjustable. Each tube has its own air tank and the airflow in the tubes can be adjusted independently. The laser light sheet is positioned in the middle of the tubes.

air through two 2.5-mm-ID tubes that are attached to the instrument carriage and held at the same vertical plane normal to the direction of the carriage motion. These tubes are oriented vertically with the bottom end of the tubes positioned at about 1 cm above the water surface. The horizontal distance between the tubes can be adjusted in a range from about 4 cm to 14 cm (see figure 4.2). Each tube is connected to a separate compressed air tank via a separate system consisting of a pressure regulator, a needle valve, a flow meter and flexible hoses. The airflow in each tube is controlled independently of the other tube.

Qualitative and quantitative measurements of the wave pattern downstream

of the two tubes is done using methods explained in detail in §2.3. Here, we provide a brief description of the methods. The main features of the surface response are visualized qualitatively using a refraction-based method. A pattern of randomly placed dots is printed on a translucent screen which is in turn attached to the carriage via a vertically oriented traverser and held parallel to the calm water surface. The distance between the dot pattern and the water surface can be adjusted using the traverser. A vertically oriented camera (camera 1 in figure 4.2) images the dot pattern through the bottom of the tank and the water free surface. Due to the refraction at the air-water interface the dot pattern images become distorted and it is possible to interpret the raw images to find the locations of surface depressions as follows. A lump-like depression is characterized by a profile with two low amplitude crests and a high amplitude trough between the two crests in the direction of propagation and a more elongated profile in the direction normal to the direction of propagation. The aspect ratio of this surface wave pattern is about 5. In the present measurements, the dot pattern is positioned far from the free surface and the dots appear as lines at places with high surface slope (e.g. between a crest and a trough) and the dot density increases at the trough of a lump. The lensing effect of the surface curvature also changes the light intensity in the images and helps with interpreting them. Along with these qualitative visualizations of the surface wave pattern, the cinematic Laser Induced Fluorescence (LIF) method was used to measure the wave height along the center line of the two tubes, see figure 4.2.

The level of the forcing is controlled by the airflow in the air-jet tubes and is denoted by the nondimensional parameter $\epsilon = h_0/d$ where h_0 is the depth of

the circular depression under the tube when the carriage is stationary and d is the internal diameter of the tube. In the experiments presented in this chapter, ϵ ranged from 0.30 to 0.40. The carriage speed is indicated by nondimensional parameter $\alpha = U/c_{\min}$ where U is the carriage speed. Three values of $\alpha = 0.986$, 0.994 and 1.003 were used in the experiments. When only one pressure source is active, these α values provide state III responses for the range of ϵ used. The distance between two tubes (D) was varied between 4 and 12 cm.

4.3 Results and discussion

In this section, the water surface deformation patterns produced by two air jets moving side by side at speeds near $c_{\min}$ are explored through the raw refraction images and the LIF surface shape measurements along the streamwise mid-line between the two air jets. The behavior of the two-jet surface pattern is better understood by first comparing it during its formation to the pattern development for a single air jet. To this end, two sequences of six refraction images at the condition $\epsilon = 0.30$ and $\alpha = 0.994$ are shown in figures 4.3 and 4.4. In figure 4.3, the surface deformation pattern is generated by a single air jet located near the upper left corner of each image, while in figure 4.4 there is an air jet in each corner, separated by 8 cm in the physical plane. The first images were obtained just after the air-jet tube reached constant speed and the images in each sequence are separated in time by 0.25 s. For the single air jet, the pattern develops as described qualitatively by Diorio *et al.* (2009) and measured in detail in §2.5.2. At this condition, a sequence

of pairs of lump-like depressions are generated periodically at the ends of a small V-shaped pattern and once formed, each lump propagates along an approximately straight line ray oriented at an angle of about 15 degrees to the direction normal to the carriage motion. In the images in figure 4.3 only the right side of the nearly symmetric pattern is shown. The long axis of the lump is nearly aligned with the rays, i.e., the propagation direction. The propagation speed of the lump along the ray is relatively slow in the images, but in the reference frame of the laboratory, the lump moves along the tank at a speed a little less than $c_{\min}$ with a small angle to the towing direction, i.e., in the direction perpendicular to the long axis of the lump. The shedding period of these pairs of lumps was shown in figure 2.24 and found to decrease with increasing towing speed, reaching around 1 s as the towing speed approaches $c_{\min}$. The timing of the shedding of the first lump is fairly repeatable from run to run.

When both air jets are turned on, the shedding of the first lumps from the two air jets is nearly synchronized, see the first two images in figure 4.4. In the third image, the left edge of the lump from the right air-jet tube and the right edge of the lump from the left air-jet tube meet in the center plane. As the lumps collide, a pattern of small-amplitude waves radiates radially away from the location of the collision; one of these radiated waves is barely visible in the top center of the fourth image. The radiated waves have small amplitude, but can be seen clearly in the movie image sequence. By the time of the fifth image, the radiation has stopped and a pattern of three rows of lumps has formed with the first row of two lumps directly behind the air jets, the second row of two lumps a little farther downstream

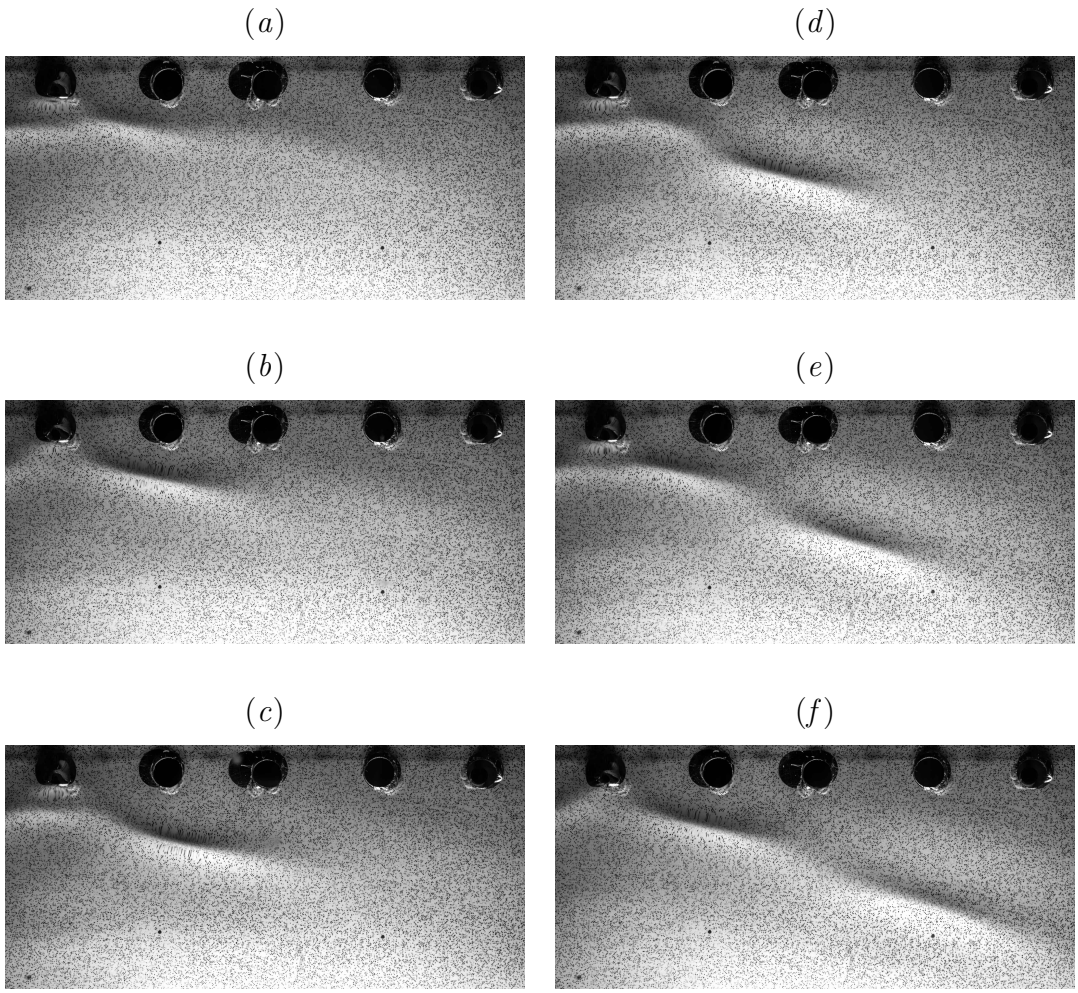

Figure 4.3: Sequence of dot pattern images with one air-jet for $\alpha = 0.994$ and $\epsilon = 0.30$. The time separation between images is 0.25 s.

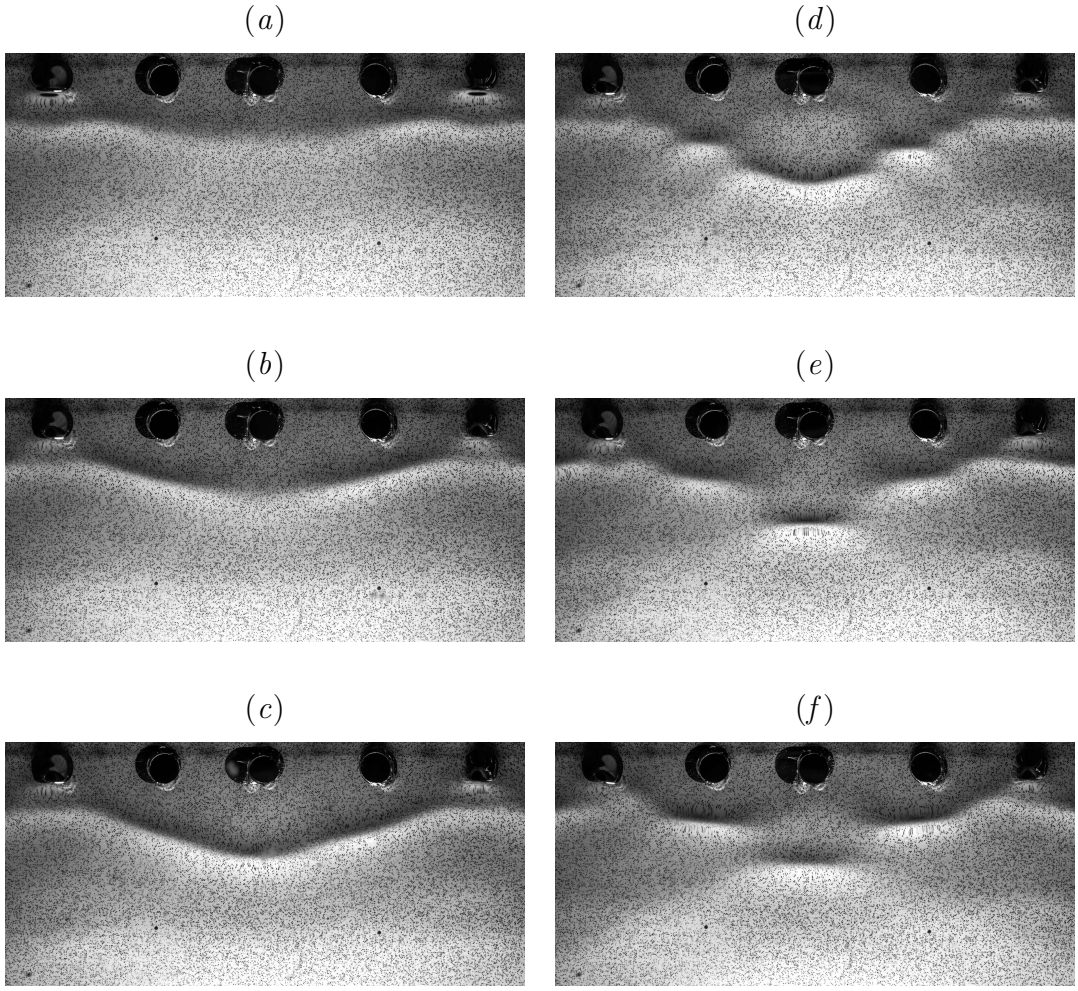

Figure 4.4: Sequence of dot pattern images with two air-jets for $\alpha = 0.994$, $\epsilon = 0.30$ and tube separation of $D = 8$ cm. The time separation between images is 0.25 s.

and the third row, consisting of a single lump centered on the midline between the two air jets. While this basic pattern is stable, the streamwise position of the lumps varies by a small amount in time and small-amplitude waves radiate from the downstream lump periodically. The lumps in the second and third rows have become oriented with the long axis nearly perpendicular to the flow direction. Radiation events at the center-plane lump occurs with a seemingly random periodicity.

The collision event and the radiation of small amplitude radial waves can be seen more clearly in figures 4.5 and 4.6 where the tube separation is fixed at $D = 12$ cm. In figures 4.5 *a*-*c*, two isolated lumps approach the center plane and collide in figure 4.5-*d* and form a pattern with several rows of localized depressions oriented normal to the carriage motion. This pattern is relatively stable with the depth of the middle depression oscillating in a manner similar to the breathers described in Wang & Milewski (2012). A breather is a time periodic localized structure, in this case a depression lump, with periodic amplitude modulations. A sequence of images just after the collision are shown in figure 4.6 with a time separation of 0.15 s between images. The propagation of a small-amplitude radial wave form the collision location is visible in these images (The wavefront is denoted by red arcs in the images in the right column of the figure). From these images, the propagation speed of the wavefront is measured to be approximately 27 cm/s in the reference frame of the lab.

The distance between the two air-jet tubes, D, has a strong influence on the surface deformation pattern. This pattern is shown in figure 4.7 for $D = 4$, 6, 8, 10 and 12 cm. The field of view is the same for all images and the active air jets for the $D = 10$ and 12 cm cases are outside the field of view. For each condition, the deformation pattern at the instant 0.2 s after the first collision is shown. If the disturbance under and just behind the air-jet tubes is called the first row, then there are two rows of lumps for the $D = 4$ cm case and four rows of lumps for the $D =$ 12 cm case.

The stable pattern with several rows of lumps looks similar to the steady

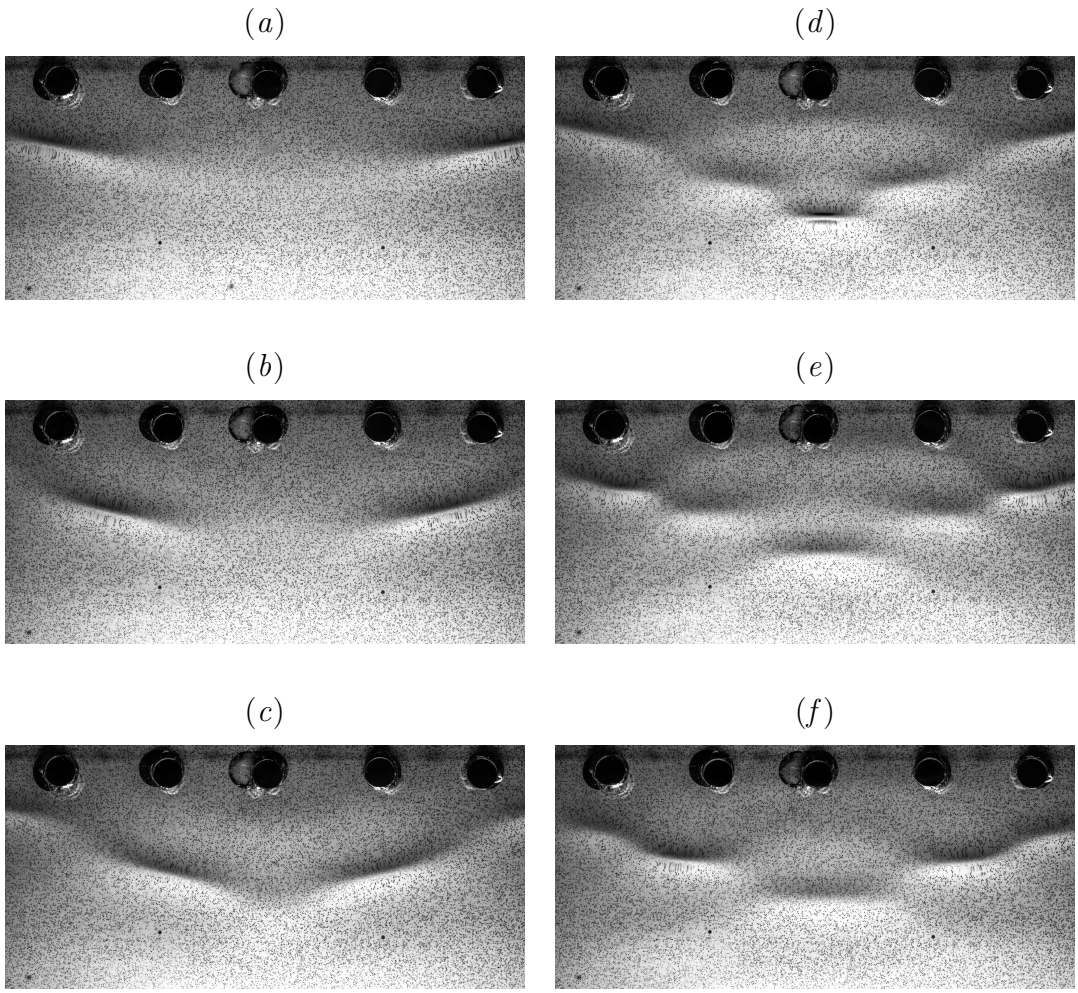

Figure 4.5: Sequence of dot pattern images with two air-jets for $\alpha = 0.994$, $\epsilon = 0.30$ and tube separation of $D = 12$ cm. The time separation between images is 0.25 s.

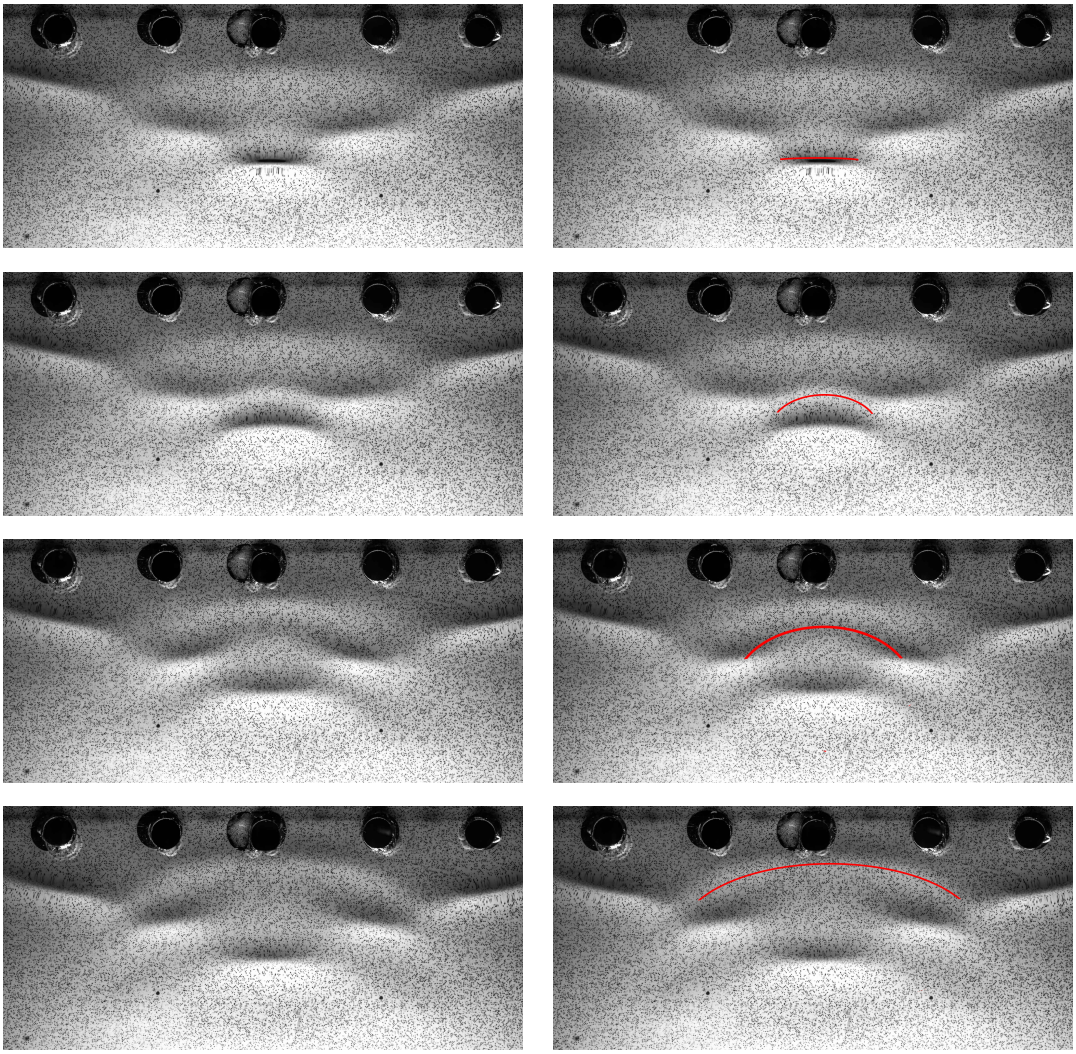

Figure 4.6: Snapshots for $\alpha = 0.994$ and $\epsilon = 0.30$ with time separation of 0.15 s and a tube separation of $D = 12$ cm. Propagation of a radial wave is visible in these images.

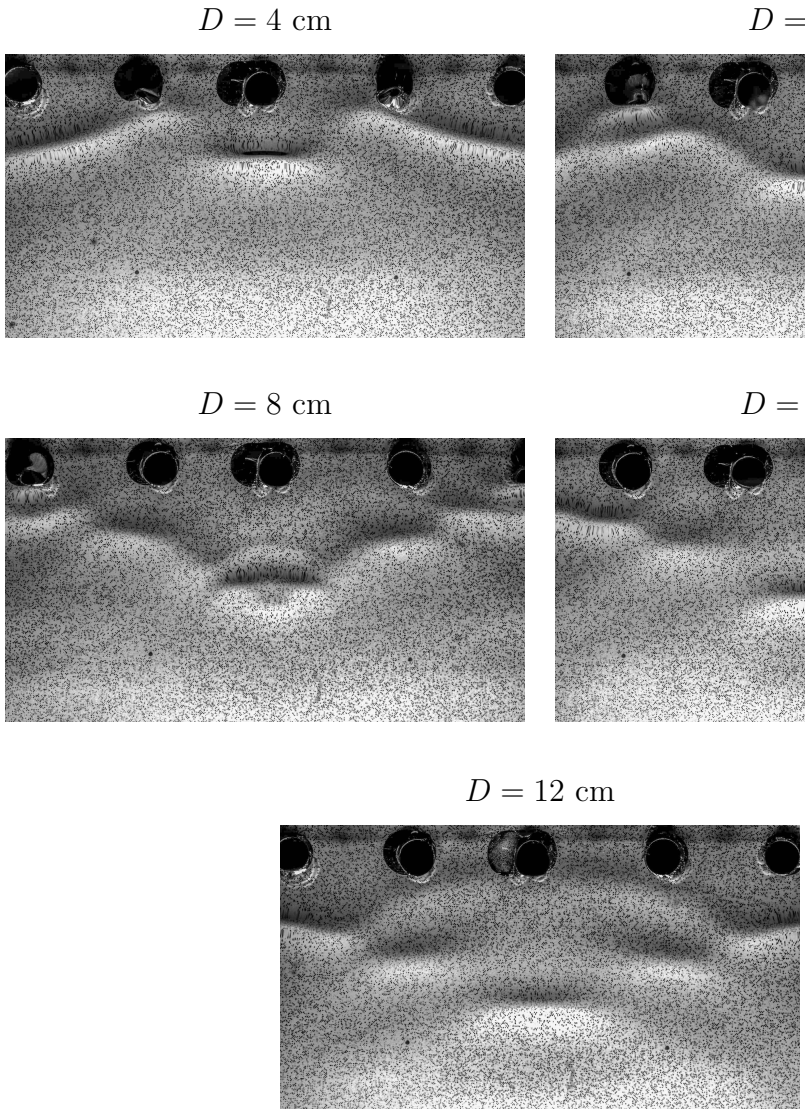

Figure 4.7: Free surface shape 0.2 s after the first burst for $\alpha = 0.994$ and $\epsilon = 0.30$ and tube separations of $D = 4$, 6, 8, 10 and 12 cm.

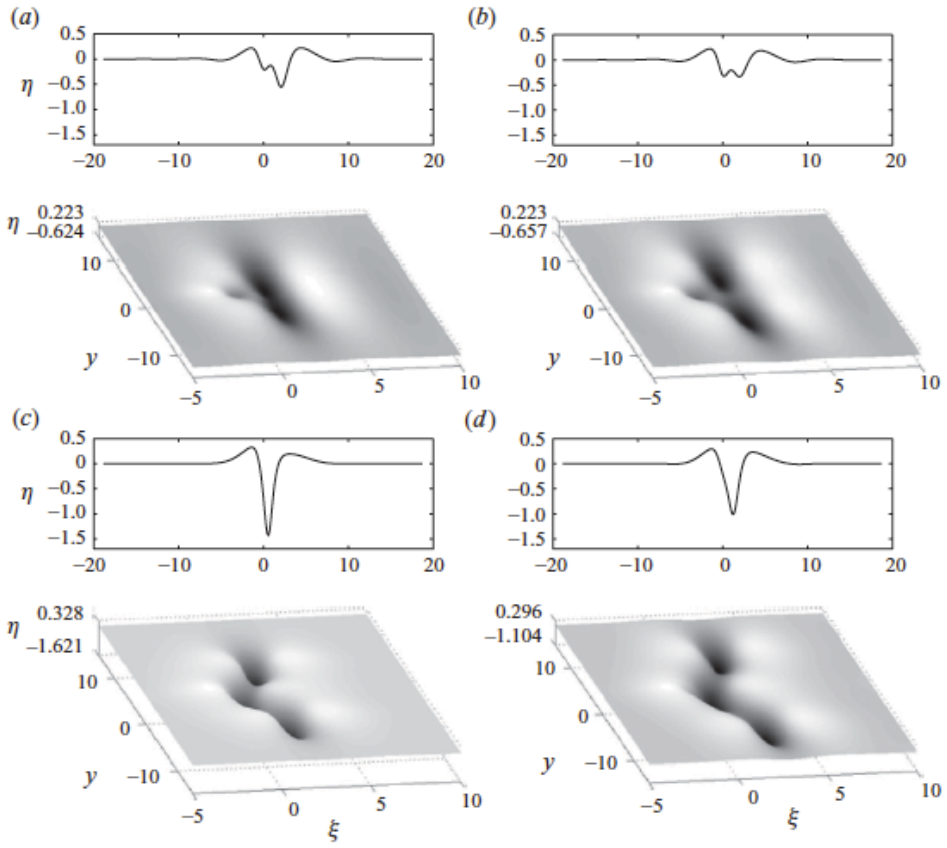

Figure 4.8: Steady patterns with multiple lumps from Cho *et al.* (2011).

patterns found by Cho *et al.* (2011) and shown in figure 4.8. They used an arclength continuation method (Cho, 2014) to find steady patterns beyond the third turn in the bifurcation curve. The first and second turns are associated with the formation of a steady lump in state II and the response is expected to be unsteady beyond the third turn. Nonetheless, by carrying on the continuation beyond the third turn, they found steady patterns with multiple lumps downstream of the source and suggested a new state can bifurcate with several rows of lumps, but did not pursue this possibility.

The LIF images are used to obtain quantitative measurements of the wave

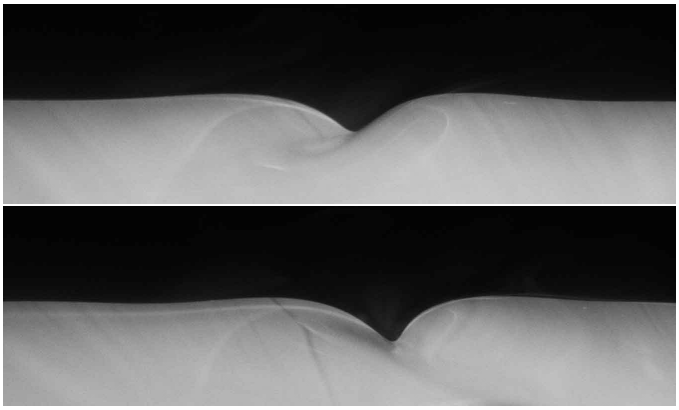

Figure 4.9: LIF image in the center plane of the tubes with $\alpha = 0.994$, $\epsilon = 0.30$ and $D = 8$ cm. Source moving from left to right. Left: 1 tube active. Right: both tubes active, just before the first burst.

height in the midline of the two tubes. Examples of raw LIF images are shown in figure 4.9. In these images the source is moving from left to right. The image on the left shows a state III lump (only one air jet is on) as it passes through the laser light sheet. The image on the right shows the surface shape when both air-jets are on and just before the first burst. Both images are taken at the same instant relative to the carriage motion start time. It is observed that in the case when both air-jets are on, the depression in the midline of the air-jet tubes becomes asymmetric and very steep (almost vertical at the front edge) just before the burst event.

In order to illustrate the evolution of the free surface, a sequence of profiles extracted from the LIF images are shown in figure 4.10. In this figure, the source is moving in the positive x-direction in the laboratory reference frame and is located at $x = 0$ in the moving reference frame of the plot. The horizontal and vertical axes

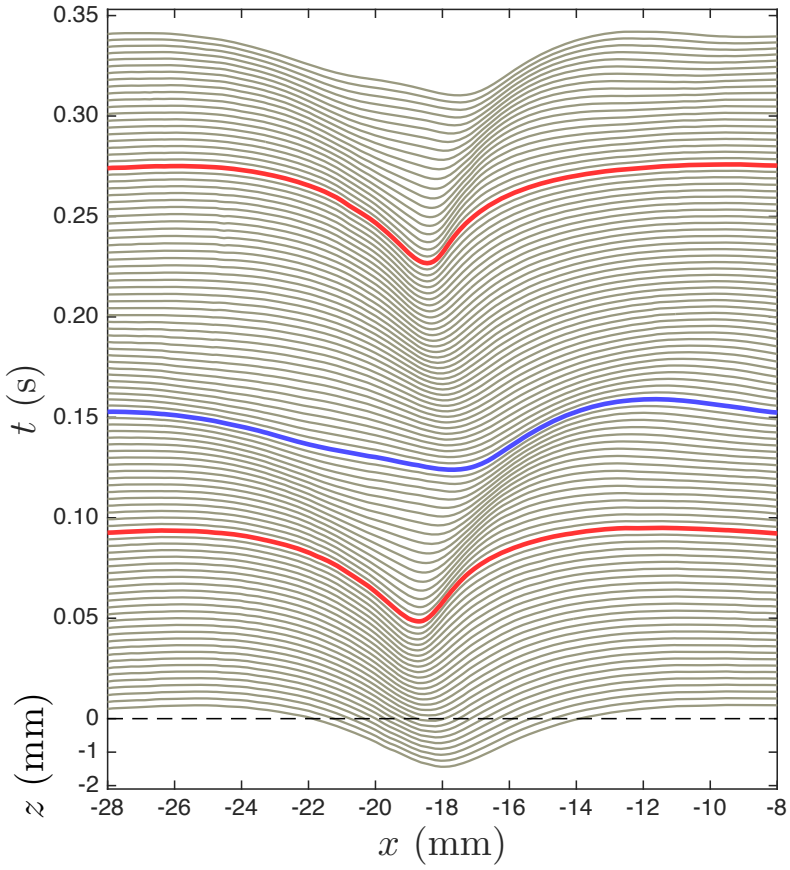

Figure 4.10: Free surface profiles in the center plane of the tubes for $\alpha = 0.994$, $\epsilon = 0.30$ and $D = 8$ cm. Each profile is shifted vertically by 0.2 mm from the previous profile and the time difference between consecutive profiles is 1/300 s.

have the same scale and each profile is shifted vertically from the previous profile to show the evolution in time. The red lines denote the profiles for which the maximum depth of the wave is a local maximum in time. The blue line shows a profile for which the maximum depth is a local minimum in time. This set of profiles show the first collision of the lumps and the subsequent radiation of small amplitude waves. As can be seen in the plot, the surface profile of the local depression resembles the stream-wise profile of a gravity-capillary lump but becomes asymmetric and very steep (especially the front edge) as the two lumps approach the mid-plane. As the energy from the sources accumulates and the depth of the depression increases, it moves downstream of the pressure sources, consistent with the fact that the speed of a gravity-capillary lump decreases with increasing depth. Eventually this depression loses form and radiates energy away in the form of small-amplitude radial waves (between the red and blue curves in the plot). Shortly after this "burst", the energy accumulates again and another burst happens. The time scale between this double burst is about 0.2 s and it happens for all tube separations during the first collision of lumps.

The LIF profiles can be used to study the unsteady behavior of the middle depression during the first collision and also after the quasi-steady pattern with several rows is formed. Figure 4.11 shows the time evolution of the LIF profiles for a case with one air-jet (column a) and two air-jets with a separation of $D = 12$ cm (column b). The bottom plots in the figure show the maximum depth of each LIF profile versus time. The period of oscillation for both cases is about 1 s indicating that when the distance between the sources is large enough for the state III lumps

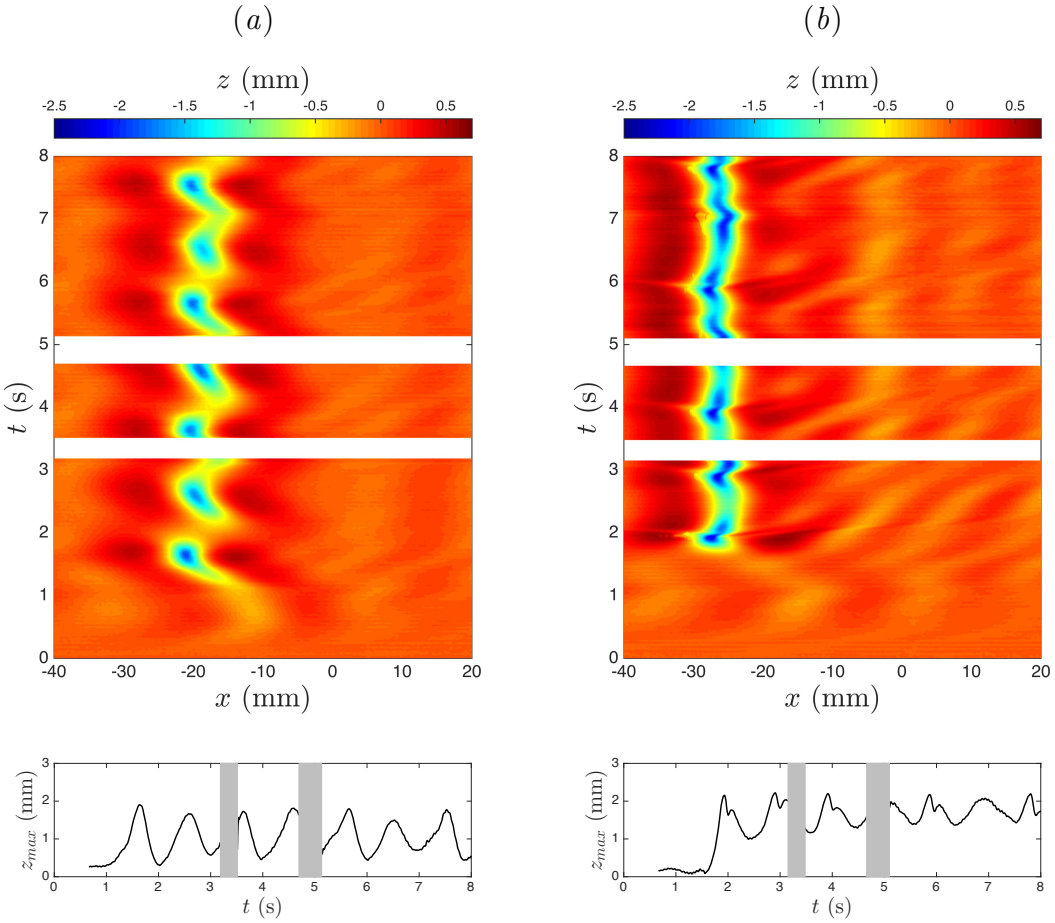

Figure 4.11: Surface height intensity maps (top) and maximum depth of LIF profiles versus time (bottom) for $\alpha = 0.994$ and $\epsilon = 0.30$. (a) One air jet. (b) Two air jets with $D = 12$ cm.

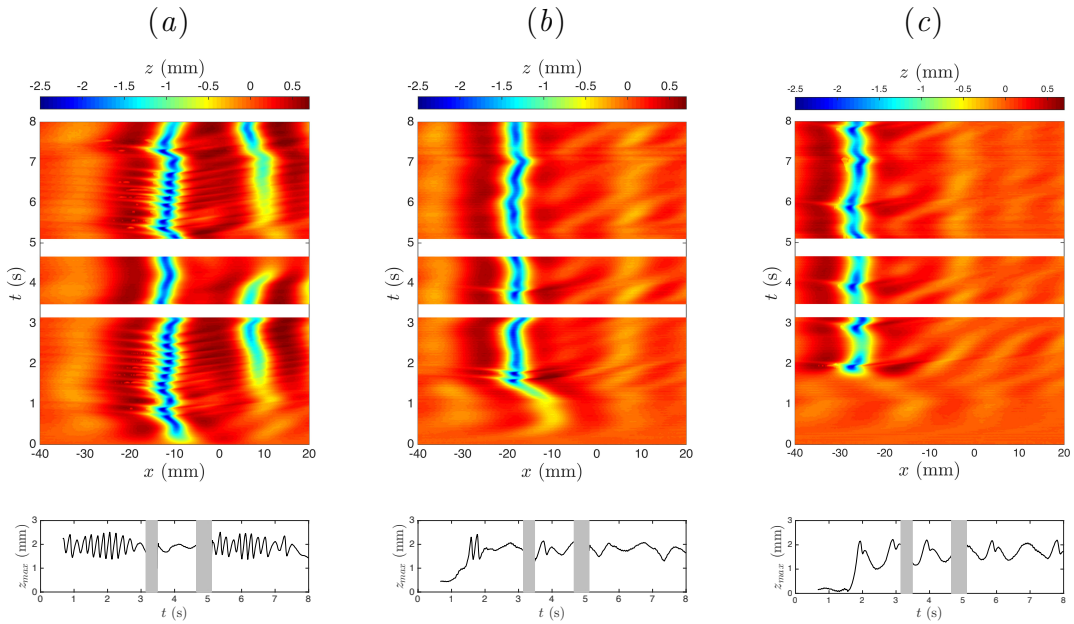

Figure 4.12: Surface height intensity maps for $\alpha = 0.994$, $\epsilon = 0.30$ and $D = 4$, 8 and 12 cm.

from two sources to form independently, the period of depth oscillations for the middle depression is probably the same as the period of generation of lumps from each source.

The effect of the tube separation (D), towing speed (α) and forcing (ϵ) on the oscillations of the middle depression are shown in figures 4.12, 4.13 and 4.14, respectively. In each case, one parameter is varied while the other two are kept constant. In general, when more energy is directed towards the middle depression (i.e. smaller tube separation, higher towing speed or higher forcing), the period of oscillation decreases. The oscillatory behavior seems to be quite complex and suggests the importance of high order nonlinear modes. While these results are promising, more thorough experiments and theoretical models are needed to provide

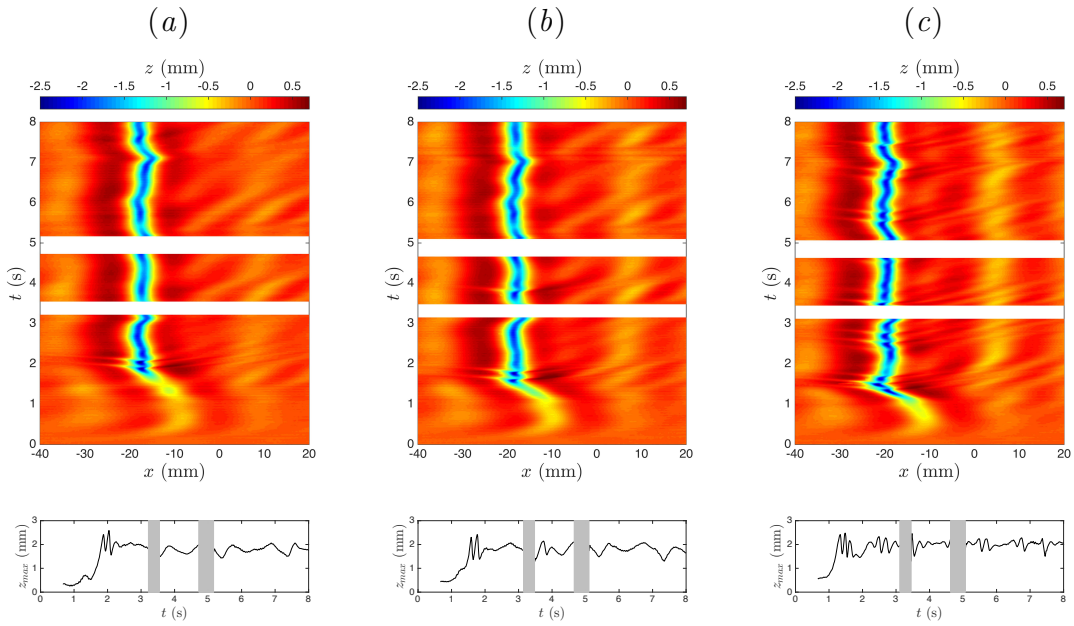

Figure 4.13: Surface height intensity maps for $\epsilon = 0.30$, $D = 8$ cm and speed parameters of $\alpha = 0.986$, 0.994 and 1.003.

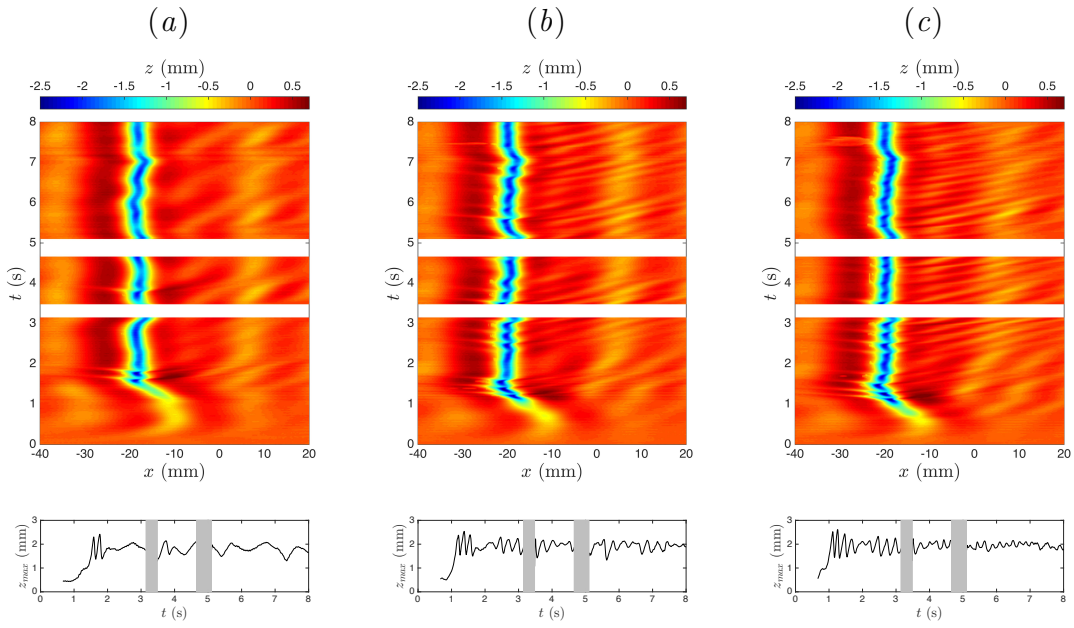

Figure 4.14: Surface height intensity maps for $D = 8$ cm, $\alpha = 0.994$ and forcing parameters of $\epsilon = 0.30$, 0.35 and 0.40.

an explanation for the observed phenomenon.

4.4 Summary and conclusions

In this chapter, the interaction of gravity-capillary lumps generated by two surface pressure sources moving in parallel straight lines was investigated experimentally. When the distance between the two sources is large enough, an isolated state III lump is generated from each source and moves away from the source. These two lumps then meet and interact at the center-plane of the two sources. It was observed that during the collision a steep depression is formed that is aligned normal to the direction of the source motion. In all experiments the steepness in the front edge of the depression increases as the energy from the two lumps is accumulated and eventually this isolated depression breaks and radiates energy away in the form of small-amplitude waves. After this "burst" event a quasi-steady pattern is formed with several rows of isolated depressions that are similar to steady lumps of state II but exhibit oscillations in time similar to a "breather". The number of rows and the frequency of oscillations depend strongly on the distance between the pressure sources.

Chapter 5: Concluding remarks

In this thesis we explored some aspects of the dynamics of nonlinear gravity-capillary waves that are generated by surface disturbances moving at speeds close to the minimum phase speed of linear water waves. Accurate measurements of the wave pattern produced by a source moving at such trans-critical speeds revealed that three-dimensional gravity-capillary solitary waves (or lumps) are generated periodically and have similar characteristics to free lumps of inviscid theory. The periodic behavior is found to be analogous to the periodic generation of two-dimensional solitary waves by a source moving at speeds close to the maximum speed of pure gravity waves. The unsteady gravity-capillary lumps decay under the action of viscosity as they move away from the forcing and their decay rate was measured for the first time.

The effects of viscous dissipation on freely propagating lumps was investigated in a separate set of experiments. A steady lump was first generated by applying appropriate surface pressure and towing speed. The forcing was then removed and the evolution of the shape and speed of the free lump was measured. The decay rate of these free lumps was found to be relatively high and depend on the steepness just after the forcing was removed but a constant exponential decay rate was found at

later times. This constant decay rate was found to depend on the initial shape of the lump, i.e. the towing speed of the forcing.

Lastly, the surface wave pattern generated by two sources moving in parallel straight lines and at a trans-critical speed was examined. It was observed that the two lumps generated by the sources interact in the middle and form a steep depression that quickly breaks up and radiates energy away in the from of small-amplitude radial waves. A quasi-steady pattern is then formed with several rows of lump-like depressions.

Bibliography

Adrian, R. & Westerweel, J. 2010 *Particle Image Velocimetry*, 1st edn. Cambridge University Press.

Akers, B & Milewski, P. A. 2009 A model equation for wavepacket solitary waves arising from capillary-gravity flows. *Studies in Applied Mathematics* **122** (3), 249–274.

Akers, B. & Milewski, P. A. 2010 Dynamics of three-dimensional gravity-capillary solitary waves in deep water. *SIAM Journal on Applied Mathematics* **70** (7), 2390–2408.

Akylas, T. R. 1984 On the excitation of long nonlinear water waves by a moving pressure distribution. *Journal of Fluid Mechanics* **141**, 455–466.

Akylas, T. R. 1993 Envelope solitons with stationary crests. *Physics of Fluids A: Fluid Dynamics (1989-1993)* **5** (4), 789–791.

Akylas, T. R. & Cho, Y. 2008 On the stability of lumps and wave collapse in water waves. *Philosophical Transactions of the Royal Society of London A: Mathematical, Physical and Engineering Sciences* **366** (1876), 2761–2774.

Amini, A.A., Weymouth, T.E. & Jain, R.C. 1990 Using dynamic programming for solving variational problems in vision. *Pattern Analysis and Machine Intelligence, IEEE Transactions on* **12** (9), 855–867.

Benney, D. J. & Luke, J. C. 1964 On the interactions of permanent waves of finite amplitude. *Journal of Mathematics and Physics* **43** (1-4), 309–313.

Berger, K. M. & Milewski, P. A. 2000 The generation and evolution of lump solitary waves in surface-tension-dominated flows. *SIAM Journal on Applied Mathematics* **61** (3), 731–750.

Calvo, D. C. & Akylas, T. R. 2002 Stability of steep gravity-capillary solitary waves in deep water. *Journal of Fluid Mechanics* **452**, 123–143.

Chen, Y. & Yeh, H. 2014 Laboratory experiments on counter-propagating collisions of solitary waves. part 1. wave interactions. *Journal of Fluid Mechanics* **749**, 577–596.

Cho, Y. 2010 Nonlinear dynamics of three-dimensional solitary waves. PhD thesis, Massachusetts Institute of Technology.

Cho, Y. 2014 Computation of steady gravity-capillary waves on deep water based on the pseudo-arclength continuation method. *Computers and Fluids* **96**, 253 – 263.

Cho, Y., Diorio, J. D., Akylas, T. R. & Duncan, J. H. 2011 Resonantly forced gravity-capillary lumps on deep water. part 2. theoretical model. *Journal of Fluid Mechanics* **672**, 288–306.

Craig, W. 2002 Non–existence of solitary water waves in three dimensions. *Philosophical Transactions of the Royal Society of London A: Mathematical, Physical and Engineering Sciences* **360** (1799), 2127–2135.

Craig, W., Guyenne, P., Hammack, J., Henderson, D. & Sulem, C. 2006 Solitary water wave interactions. *Physics of Fluids* **18** (5).

Crapper, G. D. 1957 An exact solution for progressive capillary waves of arbitrary amplitude. *Journal of Fluid Mechanics* **2**, 532–540.

Davey, A. & Stewartson, K. 1974 On three-dimensional packets of surface waves. *Proceedings of the Royal Society of London A: Mathematical, Physical and Engineering Sciences* **338** (1613), 101–110.

Dias, F. & Kharif, C. 1999 Nonlinear gravity and capillary-gravity waves. *Annual Review of Fluid Mechanics* **31** (1), 301–346.

Diorio, J., Cho, Y., Duncan, J. H. & Akylas, T. R. 2009 Gravity-capillary lumps generated by a moving pressure source. *Phys. Rev. Lett.* **103**, 214502.

Diorio, J. D., Cho, Y., Duncan, J. H. & Akylas, T. R. 2011 Resonantly forced gravity-capillary lumps on deep water. part 1. experiments. *Journal of Fluid Mechanics* **672**, 268–287.

Duncan, J. H., Qiao, H., Philomin, V. & Wenz, A. 1999 Gentle spilling breakers: crest profile evolution. *Journal of Fluid Mechanics* **379**, 191–222.

Falcon, É., Laroche, C. & Fauve, S. 2002 Observation of depression solitary surface waves on a thin fluid layer. *Phys. Rev. Lett.* **89**, 204501.

Forbes, L. K. 1989 An algorithm for 3-dimensional free-surface problems in hydrodynamics. *Journal of Computational Physics* **82** (2), 330 – 347.

Fouras, A., Hourigan, K., Kawahashi, M. & Hirahara, H. 2006 An improved, free surface, topographic technique. *Journal of Visualization* **9** (1), 49–56.

Fouras, A., Jacono, D. Lo, Sheard, G.J. & Hourigan, K. 2008 Measurement of instantaneous velocity and surface topography in the wake of a cylinder at low reynolds number. *Journal of Fluids and Structures* **24** (8), 1271 – 1277, unsteady Separated Flows and their Control.

Hammack, J. L. & Segur, H. 1974 The korteweg-de vries equation and water waves. part 2. comparison with experiments. *Journal of Fluid Mechanics* **65**, 289–314.

Kadomtsev, B. B. & Petviashvili, V. I. 1970 On the stability of solitary waves in weakly dispersing media. *Soviet Physics Doklady* **15**, 539.

Kass, M., Witkin, A. & Terzopoulos, D. 1988 Snakes: Active contour models. *International Journal of Computer Vision* **1** (4), 321–331.

Kim, B. & Akylas, T. R. 2005 On gravity-capillary lumps. *Journal of Fluid Mechanics* **540**, 337–351.

Korteweg, D. J. & de Vries, G. 1895 On the change of form of long waves advancing in a rectangular canal, and on a new type of long stationary waves. *Philosophical Magazine* **39** (240), 422–443.

Lee, S-J., Yates, G. T. & Wu, T. Y. 1989 Experiments and analyses of upstream-advancing solitary waves generated by moving disturbances. *Journal of Fluid Mechanics* **199**, 569–593.

Longuet-Higgins, M. S. 1988 Limiting forms for capillary-gravity waves. *Journal of Fluid Mechanics* **194**, 351–375.

Longuet-Higgins, M. S. 1989 Capillary-gravity waves of solitary type on deep water. *Journal of Fluid Mechanics* **200**, 451–470.

Longuet-Higgins, M. S. 1993 Capillary-gravity waves of solitary type and envelope solitons on deep water. *Journal of Fluid Mechanics* **252**, 703–711.

Longuet-Higgins, M. S. 1997 Viscous dissipation in steep capillary-gravity waves. *Journal of Fluid Mechanics* **344**, 271–289.

Longuet-Higgins, M. S. & Zhang, X. 1997 Experiments on capillary-gravity waves of solitary type on deep water. *Physics of Fluids (1994-present)* **9** (7), 1963–1968.

Masnadi, N. & Duncan, J. H. 2016 The generation of gravity-capillary solitary waves by a pressure source moving at a trans-critical speed. *arXiv preprint arXiv:1606.00457* .

Miles, J. W. 1980 Solitary waves. *Annual Review of Fluid Mechanics* **12** (1), 11–43.

Milewski, P. A. 1998 A formulation for water waves over topography. *Studies in Applied Mathematics* **100** (1), 95–106.

Milewski, P. A. 2005 Three-dimensional localized solitary gravity-capillary waves. *Commun. Math. Sci.* **3** (1), 89–99.

Milewski, P. A., Vanden-Broeck, J-M & Wang, Z. 2010 Dynamics of steep two-dimensional gravity–capillary solitary waves. *Journal of Fluid Mechanics* **664**, 466–477.

Moisy, F., Rabaud, M. & Salsac, K. 2009 A synthetic schlieren method for the measurement of the topography of a liquid interface. *Experiments in Fluids* **46** (6), 1021–1036.

Părău, E. I., Vanden-Broeck, J.-M. & Cooker, M. J. 2005 Nonlinear three-dimensional gravity-capillary solitary waves. *Journal of Fluid Mechanics* **536**, 99–105.

Părău, E. I., Vanden-Broeck, J.-M. & Cooker, M. J. 2007 Three-dimensional capillary-gravity waves generated by a moving disturbance. *Physics of Fluids (1994-present)* **19** (8).

Russell, J. S. 1844 Reports on waves. *Report of the fourteenth meeting of the British Association for the Advancement of Science* pp. 311–390.

Scott, A. 2005 *Encyclopedia of Nonlinear Science*. Routledge.

Vanden-Broeck, J-M. & Dias, F. 1992 Gravity-capillary solitary waves in water of infinite depth and related free-surface flows. *Journal of Fluid Mechanics* **240**, 549–557.

Wang, Z. & Milewski, P. A. 2012 Dynamics of gravity-capillary solitary waves in deep water. *Journal of Fluid Mechanics* **708**, 480–501.

Whitham, G.B. 2011 *Linear and Nonlinear Waves*. Wiley.

Wu, T. Y. 1987 Generation of upstream advancing solitons by moving disturbances. *Journal of Fluid Mechanics* **184**, 75–99.

Zhang, X. 1995 Capillary-gravity and capillary waves generated in a wind wave tank: observations and theories. *Journal of Fluid Mechanics* **289**, 51–82.